Investigating Graphene-based Devices towards Sensing Applications

Submitted by

Sneha Eashwer Singhraj

to the University of Exeter

as a thesis for the degree of Doctor of Philosophy in Physics

February 5th, 2018.

This thesis is available for Library use on the understanding that it is copyright material and that no quotation from the thesis may be published without proper acknowledgement.

I certify that all material in this thesis which is not my own work has been identified and that no material has previously been submitted and approved for the award of a degree by this or any other University.

Signed: **Sneha Eashwer Singhraj, 5th February 2018**

For my parents,
Francis Xavier and Lalita Eashwer,
who have taught me by example what it means to persevere against the odds.

Abstract

Graphene is a novel material that has exceptional electrical properties. In this work the graphene-based devices were developed towards three applications. Graphene-glass electrodes were fabricated and characterised towards understanding the electrochemical nature of graphene. It was shown that graphene could serve as an electrochemical electrode towards use as a sensing platform due to its fast electron transfer characteristics and thus exhibited potential as a platform for electrochemical sensing of electroactive species. Further, the Graphene-on-Glass electrodes were shown to be used as a working electrode to create a reversible electrochromic device where the optical transparency of the Graphene was modulated, and the electrochemical characteristics of the Graphene device were examined.

A proof-of-concept detection for the presence of a biomarker for Sepsis was developed. Large-area, functionalised graphene was shown to able to electronically sense the presence of the binding events of the Anti-PCT antibody, PCT molecule and differentiate from their bulk solution. The device was able to detect the presence of PCT over the whole medically relevant range (50 ng/L – 1000 ng/L). This sensor combines the exceptional electrical properties of graphene leading to high sensitivity, which when functionalized also yields high specificity as a sensor platform and offers a new route for diagnosis of Sepsis electronically in real time measurements.

Lastly, a hybrid graphene FET array that is embedded under microfluidic channels was developed. The effect of water on the device was measured and the utility of such devices towards sensing in aqueous media is discussed. Further, it is shown that the microfluidic channels of varying widths are able to transport water along the graphene FET array, such that individual graphene strips can sense them. This scheme is extremely useful and can be adapted to a host of other sensing applications which would benefit from dynamic and precise control on the detection of the analyte.

Table of Contents

Acknowledgements

This work would not have been possible if not for the contributions and support of several people.

First, I would like to express my deepest gratitude to my supervisor Dr. David W. Horsell. I am grateful to him firstly, for giving for giving me the opportunity to learn and work at the QSN group, and for teaching me a lot about experimental techniques. His guidance and input throughout all the stages of this work, from designing the experiments, right up to writing up this thesis has been invaluable. He was always generous with his time in discussions and willing to lend his experience and expertise to troubleshoot experiments. I cannot thank him enough for his patience, understanding and support throughout, and especially at certain pivotal moments on this journey.

Next, I would like to thank some wonderful colleagues and friends that I had the pleasure of working with and learning from. I am very grateful to Dr. Laureline Mahe, for all her help and for being so generous with her time and knowledge as I navigated the worlds of electrochemistry and biophysics. I am also grateful to my fellow occupants of G-28: Dr. Adam Price, Dr. Ivan Khrapach, Dr. Tim Khodkov, Dr. Fred Withers, Dr. Sam Hornett, Dr. Arseny Alexeev, Dr. Eugene Alexeev, Dr. Chris Downs, Dr. Dave Hudson, Dr. Tom Bointon – who made me feel welcome when I first joined Exeter University and shared their experience and knowledge with me along the way. Fabrication, lab and experiments without their advice, co-operation and cheery banter would have been considerably harder and significantly duller.

My sincere thanks also to Mr. Mark Heath who always lent a helping hand in the cleanroom and taught me how to use a lot of the equipment and to Mr. Paul Wilkins and the Physics workshop team who contributed their significant technical expertise towards helping me with designing, building and executing

my measurement set-up. I would also like to acknowledge and thank several academic members of staff at Exeter Physics for discussions, guidance and support: Dr. Stephen Green, Dr. Feodor Ogrin, Prof. Alastair Hibbins, Prof. Saverio Russo, Prof. Monica Craciun. And a big thanks to the PG admin staff at CEMPS for their support and of course to the University of Exeter for enabling me to do this research and providing me with financial support during my PhD.

Outside of work and study, several people played an instrumental part during my time at Exeter. I am truly grateful to have found and made a wonderful set of friends while in Exeter, all of whom made my time there truly memorable. First, I must express my sincerest thanks to Jill Christie, Chris and Steve Gordon for their kindness, friendship and for giving me a roof over my head when I needed it. I would also like to thank Varun Kothamachu, Lucky Bandhu, Laura Colombo, Caterina Balistreri and Selina Nath – for all the wonderful shared times, great conversation and fun we had together, my time in Exeter would not have held as much meaning without your friendship.

Lastly, I must thank a set of people that, although were not with me in Exeter, are a constant in the mosaic of my life - my friends who are spread out around the globe, and my large and loving family, that are always in my heart. Their love, encouragement, support and friendship colour my life in amazing ways and have always helped me weather every storm. I would particularly like to thank: Aarti Raghuraman for her unwavering support. And finally, I am eternally grateful to: My grandmother, Meena Eashwer and my parents, Lalita Eashwer and Francis Xavier without whose unconditional love, encouragement, support, prayers and blessings I would not be here today; and lastly, my husband, Ashwin Raghu – no words can fully express how grateful I am to him for the countless ways he supported me and for sticking with me through it all on this journey.

List of Figures

Figure 3.12: A schematic diagram showing the various steps involved in fabricating the graphene strips.

Figure 3.13: Optical microscopy images showing the graphene strips during processing, a) and c) are taken immediately after exposure to the EBL at 5x and 50x magnification respectively and b) and d) are images taken after RIE once the PMMA layer is removed at 5x and 50x magnification respectively.

Figure 3.14: Optical images at 5x magnification of two arrays of graphene ribbons after being contacted. The scale bar in both images indicates 100µm.

Figure 3.15 shows a schematic of typical device once it is full fabricated. The Blue strips represent the graphene ribbons. The yellow represents the metallised contacts. And the red represents the fluidic channels and trenches.

Figure 3.16: An optical image taken at 50x magnification of a test channel that is 5µm wide.

Figure 3.17: An SEM image taken at 5000x magnification of a test channel showing the profile of the resist that is 10µm wide and 2µm deep.

Figure 3.18: Optical images at 5x magnification showing flow channels of 3 different widths. Top left - 5µm, Top right- 20µm and Bottom left - 50µm. For all three images, the scale bar indicates 100µm

Table 3.1: List of all the devices fabricated for use in experiments along with their purpose of use, yield, graphene source and device type.

Figure 4.1: A schematic diagram showing the three-electrode electrochemical cell.

Figure 4.2: Total current as a function of applied potential at the electrode-electrolyte interface, as the sum of cathodic and anodic partial currents. The total current is represented as a solid line and the partial currents as dashed lines for a value of $\boldsymbol{\alpha = 0.5}$ Adapted from [6]

Figure 4.3: Graphs showing (a) Time-dependent concentration profiles of the oxidized species for a redox couple. The numbers 1 to 6 correspond to increasing time and so increasingly negative values of E (b) Current-potential profile of a redox couple when the potential at the working electrode is varied linearly from E_1 to E_2 as a function of time. Adapted from [5][6]

Figure 4.4: Graphs showing (a) Influence of the scan rate v ($V\ s^{-1}$) of the potential applied at the working electrode on the concentration profile at the working electrode. The numbers 1, 2 and 3 correspond to increasing scan rates. Right: Influence of scan rate on the reduction current peak height. Adapted from [5][6]

Figure 4.5: A typical Cyclic Voltammetry Potential Waveform

Figure 5.3: A schematic of the hall bar arrangement of contacts on a large area graphene Sheet

Figure 5.4: Substrate holder for the chip package Left: Side view showing wired connections to a port that is interfaced with a dipstick for low temperature measurements. Right : Top view showing the device architecture

Figure 5.5: A schematic diagram of the circuit used to measure the I-V_g Characteristics of the device.

Figure 5.6: A photograph taken 1 minute after HRP-PBASE functionalized graphene is immersed in an OPD solution with Phosphate citrate buffer. The colourless solution turned yellow.

Figure 5.7: R-V_g curves for the 4 samples S1-S4, (R is measured as kΩ and V_g in volts) taken at T=4.2K and V_{SD} = 1V **a)** For S1, V_D = 137.59 V **b)** For s2, V_D = 137.783 V **c)** For s3, V_D =138.12 V and **d)** For S4, V_D = 180.12 V

Figure 5.8: R-T response (measured as kΩ and seconds resp.) to addition and removal of a drop of water on the FET channel. Applied V_g = 20V. Blue arrows indicate addition of a droplet of water onto the channel. The yellow and green arrows indicate gradual drying and drying with N_2 gun respectively.

Figure 5.9: R-T response (measured as kΩ and seconds resp.) for (a) The addition of AB between L3 and L4 – ΔR = 8.4 % (b) The addition of CBB solution to R3 and R4 of the sample test sample TS1. ΔR = 4.2 % (c) and (d) correspond to the reverse process where CBB was added to L3 and L4 (ΔR = 6.4 %) and AB was then added to R3 and R4 (ΔR = 12.1 %).

Figure 5.10: R-T response (measured as kΩ and seconds resp.) for the addition of 2μL drop of 0.01M PBS solution between L3 and L4 of test sample TS3. ΔR = 6.8 %

Figure 5.11: R-T response (measured as kΩ and seconds) for the addition of (1) CBB Solution (ΔR = 3.91 %) followed by (2) addition of PCT solution between L2 and L3 of test sample TS2 (ΔR < 1 %)

Figure 5.12: R-T response (measured as kΩ and seconds resp.) for the addition of (1) AB solution (ΔR = 16.6 %) followed by (2) the successive addition and removal of DI 3 Water drops (ΔR = 8.1%) and (3) addition of PBS solution between L1 and L2 of test sample TS1 (ΔR = 4.91 %)

Figure 5.13: R-T response (measured as kΩ and seconds resp.) for the addition of (1) AB Solution (ΔR = 4.56 %) followed by (2) removal of excess liquid (3) addition of DI Water drop and (4) addition of PCT 1 solution (ΔR = 5.9 %) between L1 and L2 of sample S1

Figure 5.14: R-T response (measured as kΩ and seconds resp.) for the (1) addition of CBB solution (ΔR = 8.1 %) followed by (2) addition of AB solution (ΔR = 10.9 %) (3) removal of excess liquid and refreshing the surface with DI Water and (4) addition of PCT 2 solution (ΔR = 8.4%) between R3 and R4 of sample 2.

Figure 5.15: R-T response (measured as kΩ and secs resp.) for (1) addition of AB Solution (ΔR = 12.9 %) followed by (2) addition of PCT 1 soln (ΔR = 7.9 %) (3) addition of AB soln. and refreshing surface (4) addition of PCT 3 (ΔR = 13.9 %) solution between L3 and L4 of sample 3

Figure 5.16: R-T response (measured as kΩ and seconds resp.) for the (1) addition of AB Solution (ΔR = 9.1%) followed by (2) removal of excess liquid (3) refreshing the surface with DI Water and (4) addition of PCT 4 solution (ΔR = 15.9 %) between R1 and R2 of sample S4

Figure 5.17: A bar graph correlating the percentage ΔR shift from R-T measurements for four samples S1-S4 using 4 different concentrations of PCT 1-4.

Figure 6.1: *Left:* A CAD schematic of the device layout. *Right:* A photo showing a fully fabricated and contacted device.

Figure 6.2: A Schematic Diagram of the circuit used to measure the Resistance as a function of time for 3 graphene strips simultaneously in the device.

Figure 6.3: A Schematic Diagram of the circuit used to measure the R-T and R-V_{dc} for 2 graphene strips simultaneously in the device

Figure 6.4: *Left:* Graph showing drop in resistance as a result of the a droplet of water being placed on the graphene strip. *Right:* A photograph taken of the sample after the drop was placed.

Figure 6.5: *Left:* Graph showing resistance changes as a result of the addition and removal of water twice, being placed in the proximity of the graphene strip. *Right:* A photograph taken of the sample after the drop was placed.

Figure 6.6: A Graph showing the R-T characteristics of two graphene strips TL1 (ΔR = 0.69%)and TL2 (ΔR = 0.71%) in sample S1, for the 5μm channel upon the placement of a drop in the top reservoir.

Figure 6.7: A Graph showing the R-T characteristics of three graphene strips BR1 and BR2 and BR3, for the 50μm channel in sample S1, upon the placement of a drop in the bottom reservoir.

Figure 6.8: A graph showing the hysteretic response of the resistances for BL1 and BL2 on the application of Vdc on BL4.

Figure 6.9: Resistance modulation on the addition of 1 drop of DI water at V_{dc}=0V as a result of V_{dc} being swept between -10V and +10V. Here R1 refers to BL2 an R2 refers to BL1.

Figure 6.10: Resistance modulation on the addition of 1 drop of DI water at V_{dc}= 20V, as a result of V_{dc} being swept between -20V and +20V. Here R1 refers to BL2 an R2 refers to BL1.

Figure 6.11: Resistance Vs. Time graph showing the addition of 1 drop of DI water at V_{dc}= 20V, for the top left array of the sample S2. Here R1 refers to BL2 an R2 refers to BL1.

Figure 6.12: Photos showing the retreating meniscus of the water droplet away from the applied DC potential corresponding to the measurement in Figure 6.11

Figure 6.13: Resistance Vs. Time graph showing the addition of 1 drop of DI water and its removal by evaporation at 1) V_{dc}= 0V, 2) V_{dc}= 1V 3) V_{dc}= 5V 4) V_{dc}= 10V 5) V_{dc}= 20V for the top right of sample S2.

Chapter 1

Introduction

1.1 Motivation

Sensors are ubiquitous in modern daily life. Their use and the range of their applications is ever expanding. They are embedded in human skin, they are in our cars, cell phones, radios, watches, fitness gear, cooking equipment, and with the rise in automation, they are central to most industrial processes. In short, sensors are required to monitor things as simple as the temperature in our homes, to things as vital as sugar levels in our blood. [1-3]

In the last twenty years, with the rapid progress in the field of nanotechnology as well as an increased understanding of the physico-chemical properties of nanomaterials, there is great interest in exploring sensor architectures that are based on nanomaterials and nanostructures. The growing demand for sensor devices have necessitated the development of sensors that can deliver high performance while being low cost and operating on low power, so as to be able to sustain portable or remote applications. [2,3] Consequently, the performance and reliability of sensing devices depends critically on usage of suitable materials and appropriate device design. The miniaturization of sensors in particular, allows for lower power consumption and better integration into lab-on-chip applications. Equally, the vast array of techniques that have been discovered to

engineer nanomaterials and nanostructures can be harnessed towards fabricating extremely sensitive devices that are also extremely specific [3].

Carbon nanostructures including Carbon Nanotubes and graphene are a sub-class of nanomaterials which have generated interest in the field of sensors. [6] This is because they are composed almost entirely of surface atoms and have been shown to have exceptional electrical, physical and optical properties. They have been shown to have extremely good modulation of their electrical properties upon exposure to chemically and biologically interesting species. [2] Additionally, their structural characteristics and electrical properties enable them to be easily utilised in field-effect transistors (FETs). This is extremely advantageous as it indicates potential towards becoming integrated into more complex microelectronic systems. Lastly, carbon nanomaterials have unique electrical, physical, mechanical and chemical properties, that are widely and extensively studied, and this makes them attractive as a sensing material [3].

Single-walled carbon nanotubes were first investigated towards developing novel biosensors due to their excellent electrical properties. [3,6] Over many years of study, it emerged that there were several key problems with these devices. Firstly, it was often difficult to separate semiconducting CNTs from metallic CNTs. Secondly, they were found to be unsuitable to sense large biological species because the surface area of the CNTs were insufficient to allow proper interfacing with the analyte owing to its large, complex molecular structure. Other issues associated with CNTs included difficulty in bio-functionalisation and issues with bio-compatibility and toxicity which made it unfeasible for bio-medical applications. [2,7]. Thus, graphene with its unique structural and electrical properties first began to be studied as an improved alternative to CNTs in sensing applications.

As of date, graphene is being investigated exhaustively for its potential as a sensing element in a whole array of different sensors. It is believed to be highly promising for the development of new types of chemical/biological sensors with ultrahigh sensitivity because it is a two-dimensional material and thus every atom can be exposed to the surface adsorbates, which maximizes the signal.

The primary advantages it possessed over CNTs was that it was easier to functionalise, and it could be developed towards very large area sensing using CVD grown graphene. A large surface area would mean enhanced interaction of the surface and the analyte. [8]

Graphene's exceptional conductive properties along with a zero band gap are also extremely beneficial for conducting electrons across the biomolecule-graphene interface.[7] Moreover, properties of graphene such as large domain size (that ensure a low level of excess (1/f) noise caused by thermal fluctuations [8]),high signal to noise ratio, high mechanical strength, high thermal conductivity [10], high carrier mobility and carrier density, along with the fact that graphene is sensitive to both electron-donor and acceptor molecules, makes graphene-based devices an ideal candidate for sensing applications [7-10].

Graphene has already been shown to have massive potential as a suitable sensing material for applications such as lab-on-chip, point-of-care devices, and environmental and industrial sensors [4,11]. In fact, many have argued that utilization of graphene could lead to the production a new generation of cheap and compact sensors with unprecedented performance and quality.

In developing sensors, important sensor characteristics that must be carefully considered and optimised include the following: high sensitivity, high specificity and large range. [11] And over the last few years considerable progress has been made in developing several schemes that utilise graphene to sense a whole host of biological species including DNA, Glucose, Haemoglobin, Cholesterol and so on. [11] These schemes use exfoliated graphene, RGO, CVD graphene as well as graphene flakes in solution as the sensor material. There is also great variety in the kind of devices that are made and what role graphene plays in these devices. These broadly fall into two categories – those that employ graphene FETs and other nano-electronic structures to electronically sense the analyte through changes in the current of the device and those that use graphene as an electrode material as part of an electrochemical cell to sense an analyte by studying redox reactions at the surface of the graphene [11].

This forms the basis of the research work reported in this thesis. Two kinds of graphene devices were fabricated for use towards practical applications: graphene devices for use in an electrochemical cell were developed and studied and graphene devices for use in electronic sensing were developed and applied to detect the presence of different molecules.

1.2 Thesis Overview

This thesis discusses the development and potential of graphene-based electrochemical devices and FET devices for their use in electrochromic and sensing applications.

Chapter 2 introduces graphene as a nanomaterial with unique properties. The crystallographic and band structure of graphene is described. This forms the basis for understanding its exceptional properties: electrical, optical and mechanical. Further, the chapter discusses the two most common methods of synthesizing graphene, namely by mechanical exfoliation and chemical vapour deposition (CVD). The chapter is concluded with a description of the characterisation methods such as Optical microscopy and Raman spectroscopy that are used to evaluate the thickness and quality of graphene samples

Chapter 3 gives a detailed description of the fabrication processes and methods that were used to develop devices used in this work. First, the fabrication of graphene–on–glass electrode devices is described. These devices are used in the electrochemical characterization of graphene, as well as in the development of a graphene-based electrochromic device as described in Chapter 4. This is followed a discussion of the fabrication process employed in the development of large-area graphene sheets for electronic sensing of biomolecules. These devices are used for proof–of–concept sensing of PCT as described in chapter 5. Finally, the chapter is concluded with a detailed description of the processes involved in developing a microfluidic channel embedded onto a graphene FET-array device.

Chapter 4 begins by introducing certain key electrochemical concepts from a theoretical perspective. This is followed by a description of the two

electrochemical measurement techniques, namely Cyclic Voltammetry and Chrono-Amperometry. And finally, a detailed description of the electrochemical characterisation experiments performed with graphene–on–glass devices is detailed, followed by a discussion of the results obtained in the development of a reversible electrochromic graphene-based device.

Chapter 5 describes the development of a novel proof-of-concept electronic detection mechanism for Procalcitonin (PCT), a biomarker that presents in human blood and indicates the onset and progression of the disease Sepsis. The chapter details the background for the experiments, followed by the experimental set-up and a discussion of the results that were acquired from experiments, indicating that PCT can be detected for the desired concentration range and the sensor that was developed is able to differentiate PCT from other background analytes.

Chapter 6 investigates an alternate device architecture, where microfluidic channels are embedded onto an array of graphene FETs. This device was developed towards realising flow-sensing of analytes, as well as towards the study of the effect of water on the FET channels. This is essential if graphene is to be used as a sensing element in an integrated device.

Finally, this thesis is concluded with a summary of the results obtained in the experiments along with suggestions for the direction of future work.

1.3 Bibliography

1. Kolmakov, A., Moskovits M., Annu. Rev. Mater. Res. 2004, 34, 151–180.
2. Biosensors – A practical approach. Jon Cooper and Tony Cass. Oxford University Press 2004.
3. Ping An Hu, Jia Zhang, Le Li , Zhenlong Wang , William O'Neill, Pedro Estrela, Sensors 2010, 10, 5133-5159
4. Subbiah Alwarappan, Chang Liu, Ashok Kumar, and Chen-Zhong Li, J. Phys. Chem. C 2010, 114, 12920–12924
5. Richard L. McCreery Chem. Rev. 2008, 108, 2646–2687
6. Yuyan Shao, Jun Wang, Hong Wu, Jun Liu, Ilhan A. Aksay, Yuehe Lina Electroanalysis 2010, 22, No. 10, 1027 – 1036
7. Reina, A., Jia, X., Ho, J., Nezich, D., Son, H., Bulovic, V., Dresselhaus, M. S., Kong, J. Nano Lett. 2008, 9, 30-35
8. Dragoman, M. Dragoman, D.,Prog. Quantum. Electron. 2009, 33, 165–214.
9. Novoselov, K.S., Jiang, D.,Schedin, F., Booth, T.J., Khotkevich, V.V.,Morozov, S.V.,Geim, A.K.. PNAS 2005, 102, 10451–10453.
10. Li, X.Cai, W., An, J., Kim, S., Nah, J., Yang, D., Piner, R., Velamakanni, A., Jung, I., Tutuc, E., Banerjee, S. K., Colombo, L., Ruoff, R. S. Science 2009, 324, 1312-1314
11. Tapas Kuila, Saswata Bose, Partha Khanra, Ananta Kumar Mishra, Nam Hoon Kim, Joong Hee Lee Biosensors and Bioelectronics 26 (2011) 4637–4648

Chapter 2

Graphene

2.1 Introduction

Graphene is a novel material that consists of carbon atoms which are arranged in a tightly packed, two-dimensional hexagonal lattice. Its unique physical, mechanical and electronic properties are a function of its crystal and band structure, the study of which has led to a whole new chapter in low-dimensional condensed matter physics. Although graphene was experimentally discovered only in 2004 [1], it was first studied theoretically over 70 years ago by P.R Wallace, in his investigations on the band structure of Graphite [2].

Interestingly, the experimental discovery in 2004 contradicted a long and widely held theory, first postulated in the late 1930s by Landau and Peierls [3,4], that strictly 2-Dimensional crystals could not be thermodynamically stable and therefore could not exist. They argued that it was impossible to achieve long range order over such crystals because of the fact that that at finite temperatures, short-range thermal fluctuations in the crystals would lead to a spatial distortion in the distribution of the atoms in the crystal to such an extent as to be of the order of the inter-atomic distance. These arguments were further supported by the work of Mermin in the late 1960s [5], His work demonstrated the impossibility of long range positional order in two dimensions. This has been supported by several experimental observations, including the work of Venables

et al, studying the nucleation and growth of thin films, who observed the melting temperature rapidly decreasing with decreasing thickness, thus pushing the film to become unstable and to break up into islands when the thickness approaches about 10 atomic layers [6].

Thus, while there were experiments able to achieve low dimensional crystals [7], it was widely thought impossible for a 2-Dimensional crystal to exist independent of a 3-Dimensional bulk material or base crystal until 2004 when Geim and Novoselov successfully exfoliated graphene monolayers for the first time. Since then, many other 2- Dimensional crystal lattices have been found to exist independently and be thermodynamically stable such as boron nitride etc, thus opening up the world of physics further not just to possibilities of graphene but also to a whole class of new, interesting 2-Dimensional crystals as well as an array of hybrid materials that can be derived from them. [8]

The excitement surrounding graphene began early on, as it revealed itself to be a window into exploring many concepts in fundamental physics, including relativistic quantum phenomena. Simultaneously, an interest in its physical and chemical properties towards an array of applications began to attract attention as well. This has been aided by the fact that graphene can be produced in a wide-range of techniques allowing it to remain a relatively low-cost material to work with. Additionally, it's physical properties including its ultra-high strength and its transparency have attracted interest towards NEMs and opto-electronics applications respectively. graphene has also drawn immense interest for its potential use towards sensing applications.

In this chapter, graphene as a material is introduced. After a brief overview and history of the research on graphene, the crystallographic and band structure of graphene is described. This section is followed by a description of the main electronic properties of graphene as well as its physical properties. Subsequently, the main methods of synthesis of graphene are discussed. And finally, the chapter is concluded by describing the characterisation techniques such as optical microscopy and Raman spectroscopy which are used to characterise the graphene.

2.2 Crystallographic and Band Structure of Graphene

Graphene is a 2-dimensional arrangement of carbon atoms in a hexagonal lattice structure. This monolayer structure forms the most basic building block for all graphitic materials. Figure 2.1 schematically depicts how fullerenes, carbon nanotubes and graphite can be derived from the structure of graphene. Fullerenes which are a spherical arrangement of carbon atoms, can be thought of as essentially a graphene sheet which has been wrapped up into a ball, yielding a 0-dimensional allotrope of carbon. Similarly, carbon nanotubes can be thought of as a rolled sheet of graphene, yielding a 1-dimensional allotrope of carbon and finally, the repeated stacking of graphene sheets, yields graphite – a 3D or bulk allotrope of carbon.

In graphene, the atoms are arranged in a hexagonal planar structure. The carbon atoms have an electronic configuration of $\mathbf{1s^2\ 2s^2\ 2p_x^1\ \ 2p_y^1\ 2p_z^0}$ giving them four valence electrons. Of these, the $\mathbf{2s}$, $\mathbf{2p_x}$ and $\mathbf{2p_y}$ orbitals hybridize (sp^2 hybridization) to form 3 strong covalent or σ bonds with the nearest neighbouring carbon atoms resulting in a trigonal planar structure. These bonds do not contribute to the conduction but rather, are responsible for the robustness and strength of graphene.

The $2p_z$ orbitals of neighbouring carbon atoms that lie perpendicular to the plane, overlap to form a delocalized band of π (valence) and π^*(conduction) electrons. It is these bands that are responsible for the unique electronic properties of graphene.

The band structure of graphene can be understood by studying the relationship of energy and momentum of the electrons within the material. This can be done using the tight binding approximation, which allows us to calculate the wave function of the system as the linear combination of atomic orbitals of the block wave functions which correspond to the two unit-cell atoms A and B, as depicted in Fig 2.2. This method was first used by Wallace to calculate the band structure of single-layer graphite in 1947 [2].

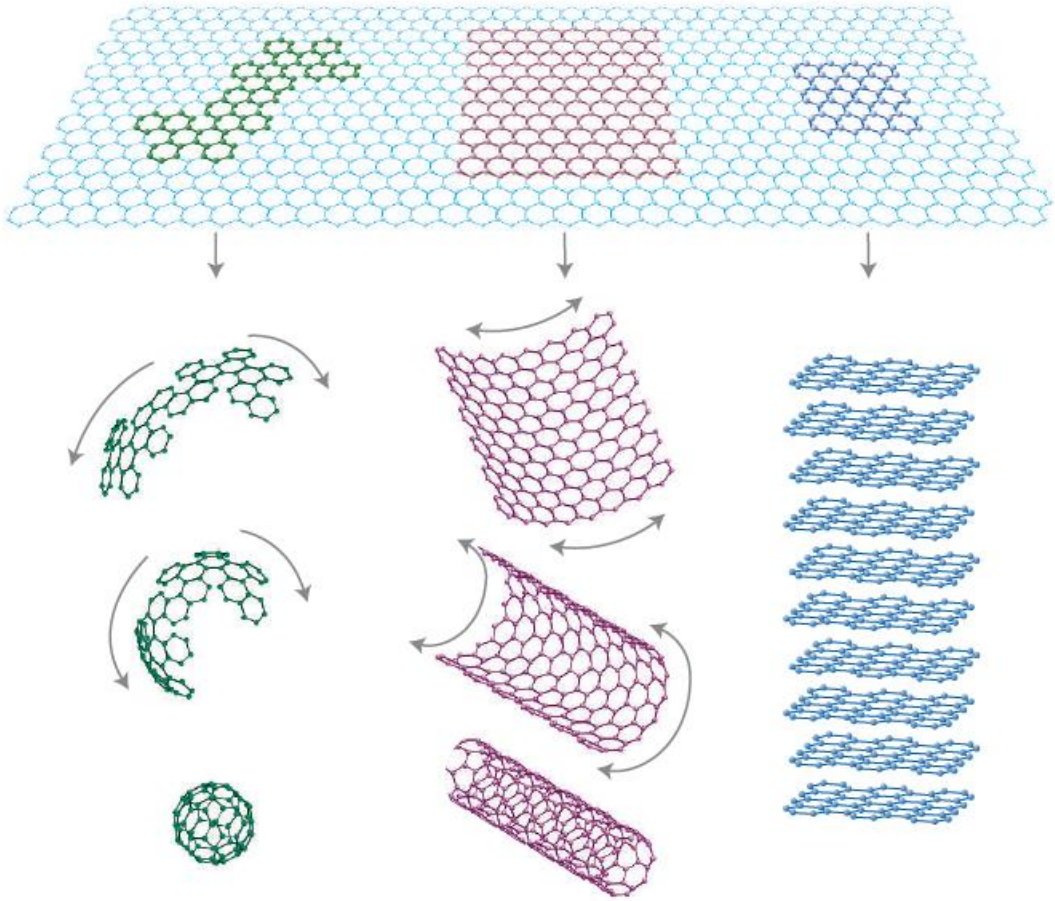

Figure 2.1: Schematic diagram showing the allotropes of Carbon: 0-D Fullerenes, 1-D Nanotubes, 2-D graphene and 3-D graphite [10]

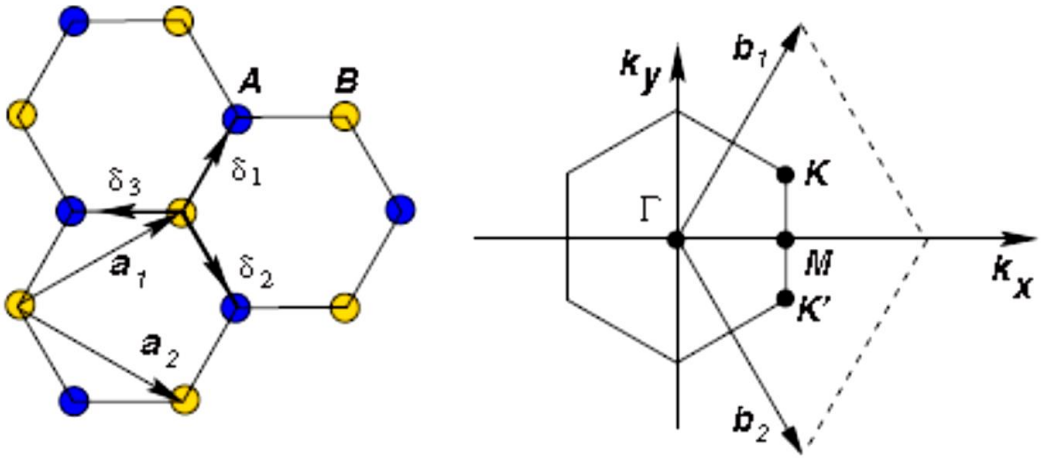

Figure 2.2: *Left*: The lattice structure of graphene in real space with Lattice vectors (a_1 and a_2) and nearest-neighbour vectors δ_1 δ_2 and δ_3. *Right*: Corresponding first Brillouin Zone in reciprocal space with the dirac points **K** and **K'** (adapted from [9])

As depicted in Figure 2.2, The structure of graphene can be visualised as two interleaving triangular lattices with a basis of 2 atoms per unit cell. These two triangular lattices are referred to as sublattices A and B respectively, such that each atom from sublattice A is surrounded by three atoms from sublattice B and vice versa.

The lattice vectors can be written as

$$a_1 = \frac{a}{2}(3, \sqrt{3}) \quad \text{and} \quad a_2 = \frac{a}{2}(3, -\sqrt{3}) \qquad [2.1]$$

where a = 1.42 Å is the interatomic spacing between two carbon atoms. The reciprocal vectors are correspondingly given by

$$b_1 = \frac{2\pi}{3a}(1, \sqrt{3}) \quad \text{and} \quad b_2 = \frac{2\pi}{3a}(1, -\sqrt{3}) \qquad [2.2]$$

In the reciprocal space, the first Brillouin Zone is defined by the boundary of the planes that bisect the vectors to the nearest reciprocal lattice points. This gives us the form of the original hexagon but rotated by π. Notably, of the six points at the corners of the first Brillouin zone, two groups of three are equivalent. So, we can consider just two of them. These corners correspond to important high symmetry points, **K** and **K'**, known as the Dirac points. And their position in momentum space is given by

$$K = \frac{2\pi}{3a}(1, \frac{1}{\sqrt{3}}) \quad \text{and} \quad K' = \frac{2\pi}{3a}(1, -\frac{1}{\sqrt{3}}) \qquad [2.3]$$

If we begin by considering that the electrons in graphene can only hop to the nearest neighbours, then the tight binding approximation yields the Bloch Hamiltonian

$$\hat{\mathrm{H}}(\vec{k}) = \begin{pmatrix} o & tS(\vec{k}) \\ tS^*(\vec{k}) & 0 \end{pmatrix} \qquad [2.4]$$

where $\vec{k}$ is the wave vector and t (~2.8 eV) is the nearest neighbour hopping energy and $S(\vec{k})$ is the overlap integral given by:

$$S(\vec{k}) = \sum_{\vec{\delta}} e^{i\vec{k}\vec{\delta}} = 2\,exp\left(\frac{ik_x a}{2}\right)\cos\left(\frac{k_y a\sqrt{3}}{2}\right) + \exp(-ik_x a) \qquad [2.5]$$

The relation for the energy is therefore given by,

$$E(\vec{k}) = \pm t\left|S(\vec{k})\right| = \pm t\sqrt{3 + f(\vec{k})} \qquad [2.6]$$

where,

$$f(k) = 2\cos\left(\sqrt{3}\,k_y a\right) + 4\cos\left(\frac{\sqrt{3}}{2}\,k_y a\right)\cos\left(\frac{3}{2}\,k_x a\right) \qquad [2.7]$$

At the band crossing points, K and K', $S(\vec{k}) = S(\vec{k}') = 0$,

The Hamiltonian near these points is given by

$$\hat{\mathrm{H}}_{K'}(\vec{q}) \approx \frac{3at}{2}\begin{pmatrix} 0 & \alpha(q_x + iq_y) \\ \alpha^*(q_x - iq_y) & 0 \end{pmatrix} \qquad [2.8]$$

and

$$\hat{\mathrm{H}}_{K}(\vec{q}) \approx \frac{3at}{2}\begin{pmatrix} 0 & \alpha^*(q_x + iq_y) \\ \alpha(q_x - iq_y) & 0 \end{pmatrix} \qquad [2.9]$$

where $\alpha = e^{\frac{5i\pi}{6}}$, $\alpha^* = e^{\frac{-5i\pi}{6}}$ and $\vec{q} = \vec{k} - \vec{K}$ and $\vec{k} - \vec{K'}$ at points K and K' respectively.

This allows us to represent the effective Hamiltonian near these points as

$$\hat{\mathrm{H}}_{K,K'}(\vec{q}) = \hbar\nu\begin{pmatrix} 0 & \alpha(q_x \mp iq_y) \\ (q_x \pm iq_y) & 0 \end{pmatrix} \qquad [2.10]$$

where $\nu = \frac{3a|t|}{2}$ is the electron velocity at these points.

If we take into account, both the nearest neighbour hopping as well as the second nearest neighbour hopping, then the relations for the energy bands are given by:

$$E_{\pm}(k) = \pm t\sqrt{3 + f(\mathbf{k})} - t'f(\mathbf{k}) \qquad [2.11]$$

where, t and t' refer to the first and second nearest neighbour hopping energies respectively and the '+' sign applies to π* band and the '-' sign applies to the π band.

The energy dispersion spectrum of graphene as calculated for a finite value of t and t' is shown in Figure 2.3. From eqn. 2.6, it is evident that if t'=0, then the spectrum will be symmetric at zero energy. For finite values of t' however, the symmetry gets broken and the π and π* bands will be asymmetric in nature.

In Figure 2.3, a zoomed-in view of the energy dispersion spectrum close to the so called 'Dirac points' is also shown, which reveals a conical structure. The dispersion at these points can be described by looking at eqn. [2.4], for the region around the two points K and K'. In this case, we can substitute k with $\mathbf{k} = \mathbf{K} + \mathbf{q}$ for all $|\mathbf{q}| \ll |\boldsymbol{K}|$ such that, the eqn. [2.4] becomes

$$E(q) \approx \pm v_f |\mathbf{q}| + O\left[(\frac{q}{K})^2\right] \qquad [2.12]$$

where $v_f = 3t\frac{a}{2}$ is the Fermi velocity and $\mathbf{q}$ is the momentum measured relative to the Dirac points, K and K'. This effectively means that for undoped, pristine graphene, the Fermi energy level cuts across these points in such a way that the there is no band gap between the valence and the conduction bands.

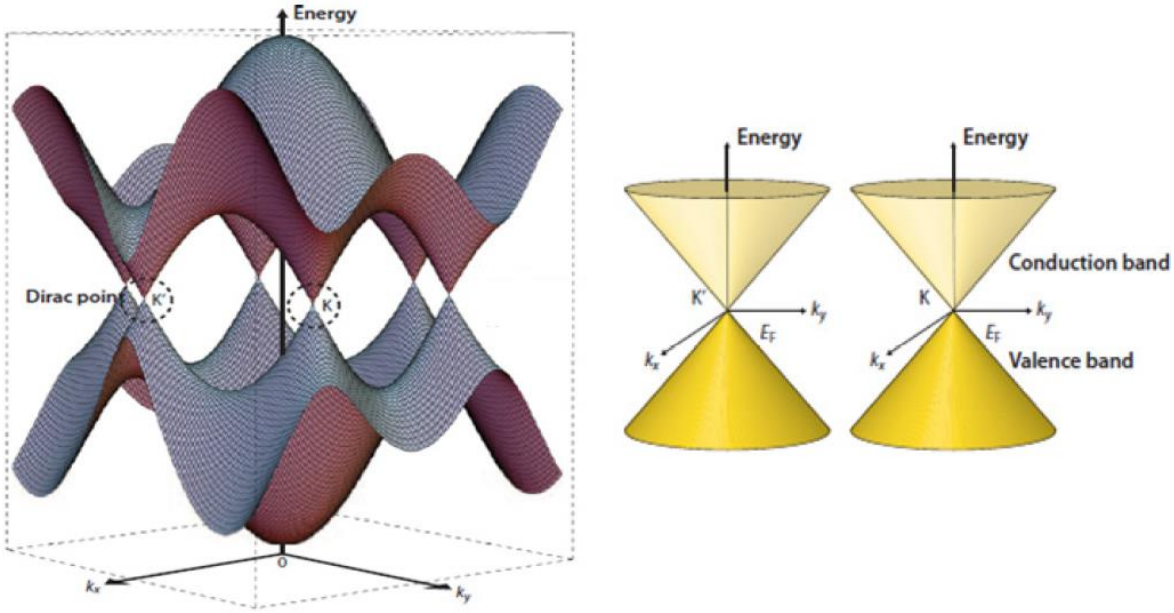

Figure 2.3: The energy band spectrum near the Fermi level in graphene. Inset: The conduction bands touch at K and K' *Right:* The conical energy bands in the vicinity of K and K' [52]

2.3 Electrical Properties of Graphene

In pristine graphene, the fermi energy coincides exactly with the energy level at the Dirac points, such that there is no band gap between the valence and conduction bands. This characteristic, along with the fact that graphene has a high degree of electron-hole symmetry, virtually ballistic transport over large mean free paths and ultra-high mobility makes it stand out as a material of great interest by virtue of its electrical properties alone. [1,9,10,37]

This section gives a brief overview of some of the most important aspects of graphene's electrical properties

2.3.1 Density of States

The density of states (DOS) of graphene per unit cell is the no. of states per unit energy. It is given by the equation

$$\rho(E) = \frac{dn}{dE} = g_v \frac{2\pi k}{N} \frac{dk}{dE} \qquad [2.13]$$

where g_v denotes the degeneracy of the states, N represents the total number of states, and the factor (2πk dk) is the additional area of the Fermi surface for an infinitesimal increase dk .

For mono-layer graphene, close to the dirac points, the energy dispersion relation can be simplified to $E = \hbar v_f k$. Taking the differential, we get $dE/dk = \hbar v_f$ and substituting in equation 2.7we find that

$$\rho(E) = g_v \frac{E}{(\hbar v_f)^2} \qquad [2.14]$$

This is noticeably different from conventional 2 DEG systems, as depicted in Fig. 2.4, which have a parabolic energy dispersion relation and consequently, a constant DOS.

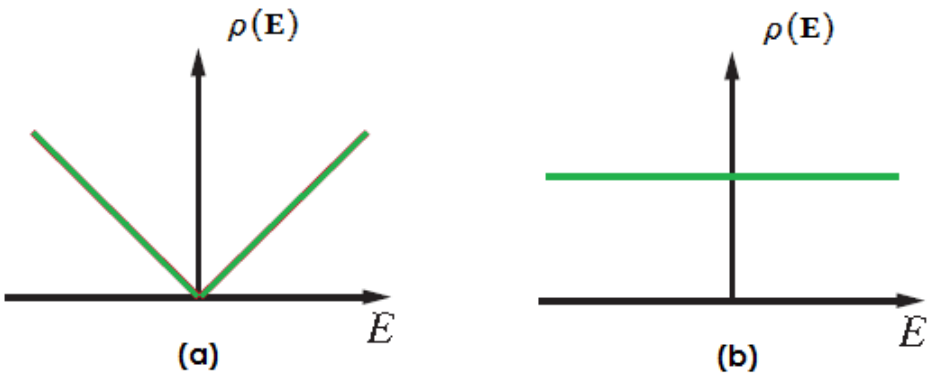

Figure 2.4: A schematic representation of the density of states for (a) Monolayer graphene and (b) a conventional 2DEG.

2.3.2 Massless Dirac Fermions

As described in section 2.2, near the Dirac points K and K', the energy dispersion relation of graphene is linear in nature.

The dispersion relation near the K points can be expressed as

$$E_{\pm}(K) = \pm \hbar v_f \mid k - K \mid \qquad [2.15]$$

And the corresponding Hamiltonian for these points is given by

$$\hat{H}_k = \hbar v_f \begin{pmatrix} 0 & k_x - ik_y \\ k_x + ik_y & 0 \end{pmatrix} = \hbar v_f \, \vec{\sigma}. \, \vec{k} \qquad [2.16]$$

$$\hat{H}_{k'} = \hbar v_f \, \vec{\sigma^*}. \, \vec{k} \qquad [2.17]$$

where $\vec{\sigma} = (\sigma_x, \sigma_y)$ is the 2D vector for the pauli matrices, $\vec{k}$ is the wave-vector and v_f refers to the Fermi velocity, which is $\approx 10^6 \, m/s$.

This linear dispersion is analogous to the dispersion relation for that of photons $E_k = \hbar ck$ except that in the case of graphene, the speed of light c is replaced by the fermi v_f velocity . This means, that in this region, the charge carriers in graphene have an effective mass that is undefined, and the charge carries behave like relativistic particles with an effective speed given by the Fermi velocity. These electrons in graphene interact with the periodic potential of the graphene lattice yielding new quasi particles. These quasi-particles can be accurately described by (2+1) dimensional Dirac equation and are therefore referred to as massless Dirac fermions [10].

This property of the charge carriers in graphene gives rise to many interesting and unusual transport behaviour such as anomalous quantum hall effect and half-integer quantization.

2.3.3 Electric Field Effect and Mobility

In order to study the effects of electric field on graphene, a typical device with 'Hall bar' geometry is employed. graphene is deposited on a Si/SiO_2 substrate and electrical contacts, typically gold, are defined on top of it using electron beam lithography. These electrodes are patterned in a specific geometry known as the hall bar geometry. This consists of source and drain contacts as well as four voltage probes. The Si acts as the back gate with the layer of SiO_2 acting as an insulating layer.

As depicted in Fig. 2.5, a source current is applied between the source and drain contacts. And the voltage drop across the length of the channel can be measured by measuring the potential drop between the two voltage probes. This device geometry allows us to change and tune the charge carrier concentration of electrons and holes in graphene by applying a gate voltage V_g between the doped Si substrate (back gate) and the graphene channel across the dielectric layer. In the above set-up, a positive voltage induces electrons in the graphene channel, while a negative voltage induces holes.

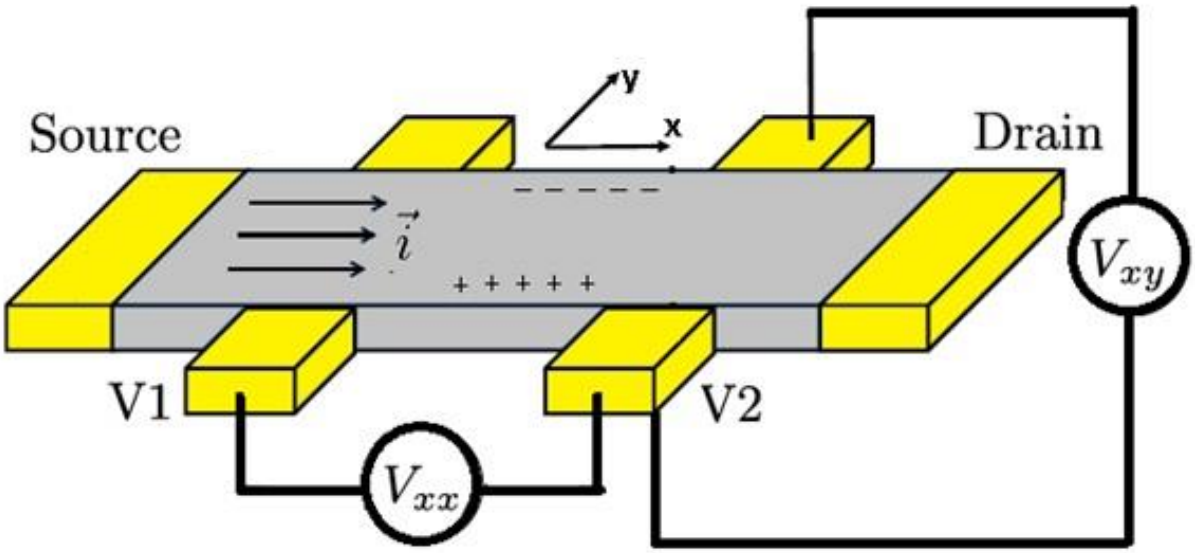

Figure 2.5 : Schematic diagram of a graphene FET device geometry to measure field effect and mobility.

When a positive voltage is applied, a negative charge accumulates on the graphene channel and shifts the fermi level into the conduction band. Thus, as we increase the gate voltage, the density of states occupied in the conduction band increases and more electrons can participate in the conduction. Analogously, when a negative voltage is applied, the Fermi level is lowered into the valence band and conduction can take place with the charge carriers being holes. In both directions however, as the voltage increases, the resistance drop starts to saturate and this attributed to the presence of short range scatterers in the graphene crystal [37]. If a magnetic field is turned on, perpendicular to the

plane of the graphene channel, another potential V_{xy} develops in the transverse direction, across the width of the channel. In real-life experiments, however, the Dirac point does not coincide with $V_g = 0$ V because there are a variety of defects and impurities that affect the position of the Fermi level [36].

The Hall coefficient, which can be extracted from the hall voltage, is given by $R_H = 1/ne$. When R_H is measured as a function of the gate voltage V_g , the linear relation between n and V_g can be experimentally observed. In figure 2.7, the dependence of sheet resistivity as a function of gate voltage is illustrated. The sheet resistivity of the graphene channel shows a rapid increase as the charge carriers are depleted and displays a sharp peak known as the 'Dirac peak'. Knowing the device geometry and dimensions, Resistance of the graphene sample versus the Gate voltage can be translated to estimate both the carrier concentration and the mobility of the device.

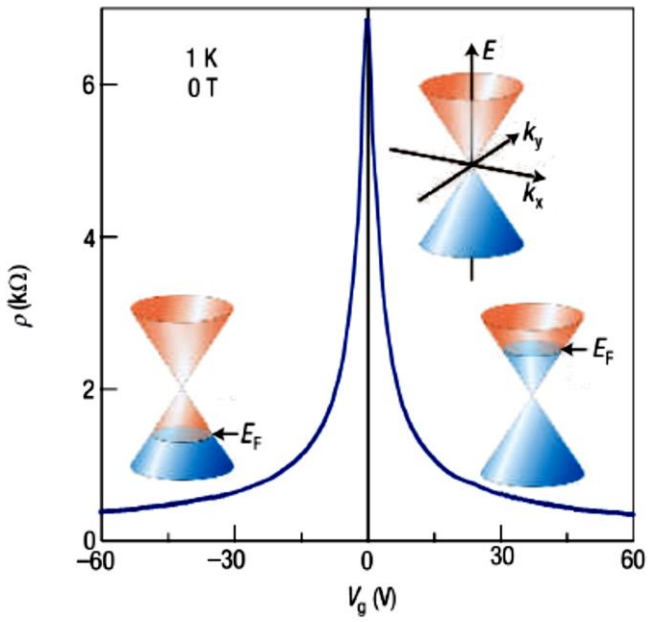

Figure 2.6: Ambipolar electric field effect in single-layer graphene. The insets show its conical low-energy spectrum $E(k)$, indicating changes in the position of the Fermi energy E_F with changing gate voltage V_g. Positive (negative) V_g induce electrons (holes). The apid decrease in resistivity ρ on adding charge carriers indicates their high mobility (Illustration taken from [10])

In a typical graphene device geometry such as figure 2.6, the mobility can be calculated using the direct transconductance method

$$\mu = g_m \frac{L}{WCV_{DS}}$$

where L is the length of the sample between the two voltage probes, W is the width, R is the resistance and C is the capacitance per unit area given by $C = \epsilon_0 \epsilon \frac{A}{t}$ where A is the area L*W and the transconductance $g_m = \frac{\partial I_{DS}}{\partial V_g}$ and I_{DS} is the source-drain current and V_g is the gate voltage.

Even at room temperature, where many scattering phenomena and thermal fluctuations limit the transport of charge carriers, Graphene devices that have been fabricated on top of mechanically exfoliated graphene have been shown to consistently achieve mobilities 10,000 $cm^2 V^{-1} Sec^{-1}$. [1][39] At low temperatures mobilities of upto 25000 $cm^2 V^{-1} sec^{-1}$ have been reported. [40] [41] This means that graphene devices can achieve ballistic transport over several 100s of nanometres. [39][41]

Scattering phenomena that limits graphene mobility has been well reported including intrinsic scatterers such as surface phonons and extrinsic scatterers such as microscopic ripples and charged impurities. Efforts to reduce the extrinsic scattering caused due to surface interactions have been reported by changing the substrate from Si/SiO_2 and substitute it with hexagonal boron nitride [43] which yielded mobilities of over 100,000 $cm^2 V^{-1} sec^{-1}$. Another technique used to achieve ultra-high mobilities of over 200,000 $cm^2 V^{-1} sec^{-1}$ is by suspending graphene over trenches in the substrate. The only drawback with such devices are that they are inherently fragile and are affected by slight changes in ambient temperature and atmosphere. [39] [44]

In contrast to mechanically exfoliated graphene, CVD grown graphene sheets exhibit markedly lower values of mobility. The growth process of the graphene has a significant effect on the density of defects in the form of tears, wrinkles, grain boundaries. Additionally, the morphology and the grain boundaries of the

metal on which graphene is grown influence the grain size of the graphene and consequently on the mobility of the graphene grown on them. This is ascribed to the fact that the grain boundaries introduce line defects in the path of the charge carriers thus acting as scattering points. [46][47][48]

Secondary impurities also arise because CVD graphene has to be transferred from the metal on which it is grown, to a suitable substrate. This process further introduces impurities in the form of residues that are trapped between the graphene sheet and the surface of the substrate such as etchant solution and resist residues.

While many methods have been developed to circumvent the extrinsic causes of impurities and reduce them, the mobility of CVD graphene remains far below what has been demonstrated for exfoliated graphene, from anywhere between 500 to 50,000 $cm^2 V^{-1} sec^{-1}$ [45][46]

2.4 Physical and Optical Properties of Graphene

As described in the previous section, graphene's electrical properties are unique, for its intrinsic value to explore the fundamental physics, but also in terms of applications, for its unsurpassed conduction properties. Another aspect of graphene, is its massive inherent strength. Experiments by C.Lee et al, probing the mechanical properties of graphene by nano-indentation of free-standing graphene membranes using AFM tips have given a measurement of tensile strength on the order of 100 GPa , which is about three orders of magnitude more than that of steel and the highest known strength measured for any material. [49] This finding along with a measurement of a young's modulus 0.5 TPa on suspended few-layer graphene membranes by Frank et al, reveal graphene's exceptional potential in the field of Nanoelectromechanical (NEMS) devices in applications for ultra-sensitive detection of pressure, charge and mass. [49][50]

In addition to its excellent mechanical properties, graphene's optical properties contribute significantly to make it an attractive material for use in the field of opto-electronic applications. graphene has a very high transparency to visible light. The transmittance of a single layer of graphene is given by

$$T = (1 + 0.5\pi\alpha)^{-2} \approx 1 - \pi\alpha \approx 97.7\ \%$$

where $\alpha = \frac{e^2}{4\pi\epsilon_o\hbar c}$ is the fine structure constant and $\alpha \approx 1/137$.

This means that each layer of graphene contributes to an absorbance of 1-T = $\pi\alpha$ which works out as about 2.3%. The optical absorbance of stacked layers of graphene sheets is proportional to the no. of layers and the reflectance of graphene sheets is very low at about 0.1% per layer of graphene. Combined with its excellent electrical transport properties, the optical properties of graphene have attracted a lot of interest as a replacement to ITO, which is the current standard for transparent electrode materials. This is especially so because ITO is extremely expensive due to increasing short supply of Indium. Additionally, much interest in graphene's optical properties is motivated towards realising its potential in applications such as large-area display electronics and touch screens, as well as smart windows, photo detectors and solar cells. [51]

2.5 Graphene Synthesis

Ever since 2004, when Novoselov et al. discovered that graphene sheets could be isolated from bulk graphite through a process of mechanical exfoliation, the synthesis of graphene has attracted great interest from within the scientific community. Since then many other methods have been developed to produce graphene through various physical and chemical means. One of the main reasons behind efforts in this direction has been driven by the desire of achieving higher quality, low-defect or no-defect samples. However, despite the development of many methods, including the reduction of graphene oxide sheets, liquid-phase exfoliation [32] and more exotic methods such as unzipping carbon nanotubes

[30], using molecular beam deposition [31], to date no other method has been shown to produce higher quality than the mechanical exfoliation from bulk graphite.

Another driver in this area of research has been the quest for large-scale production of graphene for device applications especially in the field of display electronics. A method that has been shown to produce reliably high-quality as well as large-area graphene is via the epitaxial growth of graphene on SiC. [28][29] This involves the thermal decomposition of SiC by heating SiC crystals in ultra-high vacuum to temperatures upto1500˚C, causing the Si from the surface to sublimate and leave behind graphene layers that are epitaxial grown on the surface.[28] The main drawback however, is the difficulty in isolating the graphene sheets from the SiC substrate and transferring it without damage to other substrates.[22]

In this section we describe in some detail the two most widely employed methods of synthesis, mechanical exfoliation and the synthesis of graphene on Cu by Chemical vapour deposition technique.

2.5.1 Mechanical Exfoliation

The exfoliation of graphene typically begins with the use of highly oriented pyrolitic graphite (HOPG) as the precursor material. This is essentially the bulk source from which individual layers of graphene are cleaved. The surface of HOPG is initially cleaned using an O_2 plasma, which removes any contaminated top layers revealing a clean surface.

This surface is then placed onto a pre-cut strip of sticky tape and pressure is applied manually by pressing down on the HOPG into the tape. The tape is then cleaved off the surface of the HOPG carefully, revealing several 100s of layers of graphene stuck to it. The section of the tape with the graphite layers is brought into contact with another untouched section of tape, and pressure is applied such that when the two sections of the tape are pulled apart, some of the layers of the

graphite have been transferred to the new section. This is repeated several times. The tape is then examined under a low-magnification microscope to identify locations with higher density of few-layer flakes. That section of the tape is then pressed carefully on to a thoroughly cleaned substrate of Si/SiO_2. If the substrate is not cleaned thoroughly, there is a risk that there will not be good enough adhesion between the substrate and flakes for a good transfer. Following the transfer, careful examination of the Si/SiO_2 substrate is needed under an optical microscope to identify the mono and few layer flakes of the desired size.

Figure 2.7: The figures show the different steps in the exfoliation and deposition of graphene from HOPG onto Si/SiO_2 (a) The exfoliation from bulk HOPG onto tape (b) The transfer on to the Si/SiO_2 substrate (c) the resultant graphene flakes [18]

The main advantage of the mechanical exfoliation method is that the highest quality, virtually defect free flakes can be obtained. More recently, larger size of flakes has been shown to be reliably achieved (300 μm^2 -1mm^2) by introducing modifications such as heat treatment and plasma cleaning of the bulk graphite source [18][19]. The disadvantages of graphene synthesis through mechanical exfoliation, despite yielding the highest quality, are nevertheless significant. They include a lack of control on the size, shape, positioning and the no. of flakes of particular layer thickness that can be achieved, as well as the time-consuming and laborious nature of searching and identifying flakes under a microscope.

2.5.2 Chemical Vapour Deposition

As described in the previous section, the mechanical exfoliation of graphene, while yielding very high-quality, does not lend itself to scaling up. This is a

limiting factor for certain device applications as well as industrial applications. Other methods capable of synthesizing larger-area graphene including the desorption of Si from SiC, leaving few layer graphene on SiC and the reduction of graphene oxide to graphene have certain limitations as well, which lack control over the number of layers and the large defect density respectively.

Chemically vapour deposited (CVD) graphene has been demonstrated to grow on several transition metals such as Nickel, Copper, Platinum and Palladium [20-24]. This method of graphene synthesis can be described as a bottom up approach wherein the graphene layers are grown layer by layer rather than broken down into individual layers from a bulk source.

Typically, a hydrocarbon source is introduced to the surface of a transition metal at very high temperatures (around 1000˚C). This causes the hydrocarbon to decompose or 'crack' at the surface of the metal, releasing carbon atoms. The carbon atoms find it energetically favourable to adsorb/aggregate on the metal surface, thus forming the graphene sheets [24][25].

The specific growth mechanism however varies from one metal to another and consequently, also the controllability on defect density and layer thickness also varies from one metal to another. For instance, on Nickel, Carbon atoms are adsorbed not just on the surface of the metal but also have a degree of solubility into the metal. Therefore, because of the high solubility of Carbon in nickel, the graphene growth occurs as it precipitates out of the bulk on to the nickel surface during the cooling phase. This mechanism, couple with the fact of Ni having smaller grain sizes, indicates the higher probability of few-layer graphene growth and less control on the defect density [20-22].

Ruoff et. al. published a method of synthesizing graphene by Chemically Vapour Depositing graphene on Cu substrates using methane. The graphene produced by this method has the advantage of large size as well as being predominantly monolayer. This is attributed to the very low solubility of C in Cu. As a result,

following a surface-catalyzed mechanism, the graphene growth using this method yields > 95% monolayer graphene [22]. At the time of publishing this method, Ruoff et al. were able to synthesize continuous films of graphene on the order of 1 cm^2. Since then the process has evolved and roll production of large-area graphene films on flexible substrates has been achieved [27]. This controllability of size has great advantages in potential applications of graphene, for ex. as transparent electrodes in Solar cells, in sensor applications as well as a nano-electronic component in the quest for flexible electronics.

In this work, CVD graphene grown on Cu has been exclusively used to fabricated devices. Therefore, the experimental methods used to achieve this growth is enumerated below.

Firstly, polished and cleaned Cu foils of around 25-50 µm thickness are introduced into the fused silica tube of the CVD Furnace as shown in Fig. 2.8 This forms the chamber of the furnace, which is first evacuated and then flushed with H_2 at a pressure of about 40 mTorr and flow rate of 2sccm. The temperature is then gradually increased from room temperature to reach 1000˚C. The ramp rate of the temperature is important because it anneals the Cu foil and increases the size of the domain on the Cu surface. This affects the domain size of the graphene flakes that form on the surface and increases the distance between domain boundaries, thus reducing defects in the graphene. [22][23] Once this temperature is reached, the hydrocarbon source in the form of methane (CH_4) gas is introduced at flow rate of about 35 sccm increasing the pressure to about 500 mTorr and kept as such for about 15 mins. This time is needed to allow for the cracking process and the nucleation and growth of continuous sheets of graphene on Cu. Fig. 2.9 graphically represents the experimental parameters such as the flow of gases, pressure etc. as a function of time.

Fig. 2.10 shows the dependence of the size of the graphene flakes on the amount of time the Cu is exposed to the high temperature and CH_4 gas flow. After the required time of exposure to CH_4, the furnace is cooled down to room temperature.

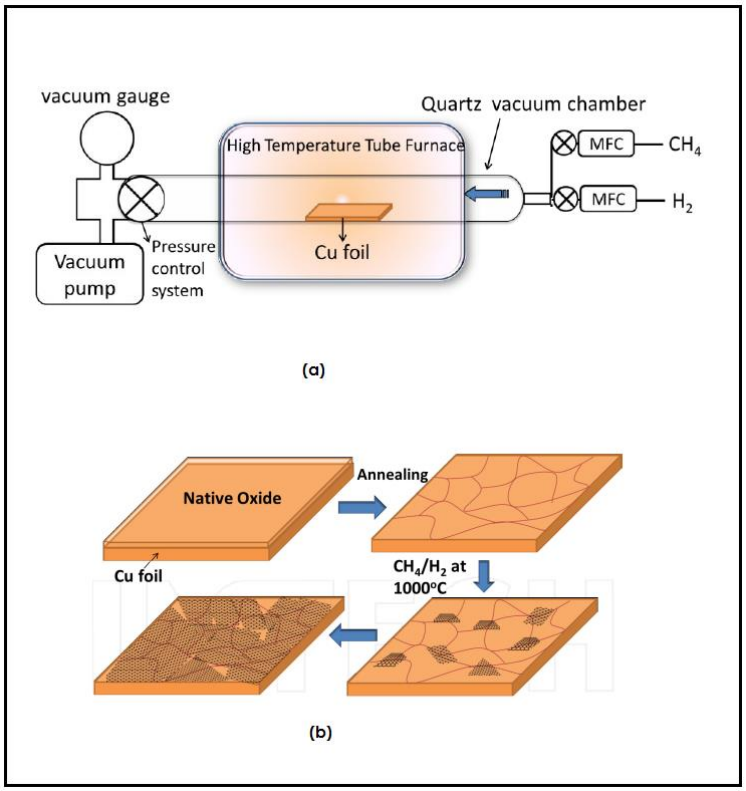

Figure 2.8: Schematic diagram showing (a) the setup for CVD growth of graphene on Cu (b) the step-by-step process that occurs on the Cu Foil during the CVD process [26]

Graphene films that are grown by CVD method on Cu need to be transferred onto other substrates to make devices. While there are many nuances that affect the ultimate quality of transferred graphene, typically, a polymer support is spun on the graphene and the metal is etched away. The graphene is transferred onto the desired substrated where a device is made using standard lithography techniques. This will be enumerated in detail in the fabrication techniques of Chapter 3

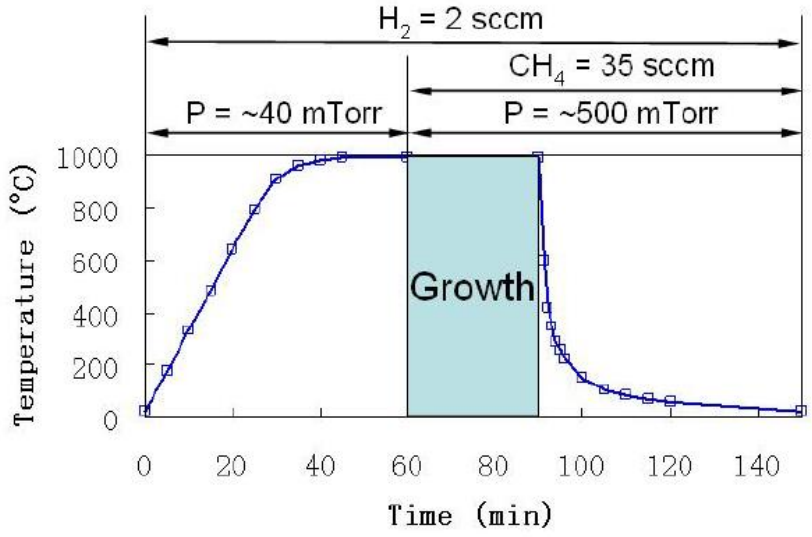

Figure 2.9: A Graph depicting experimental parameters of Temperature, Pressure and Flow as a function of time in the CVD growth of graphene on Cu [22]

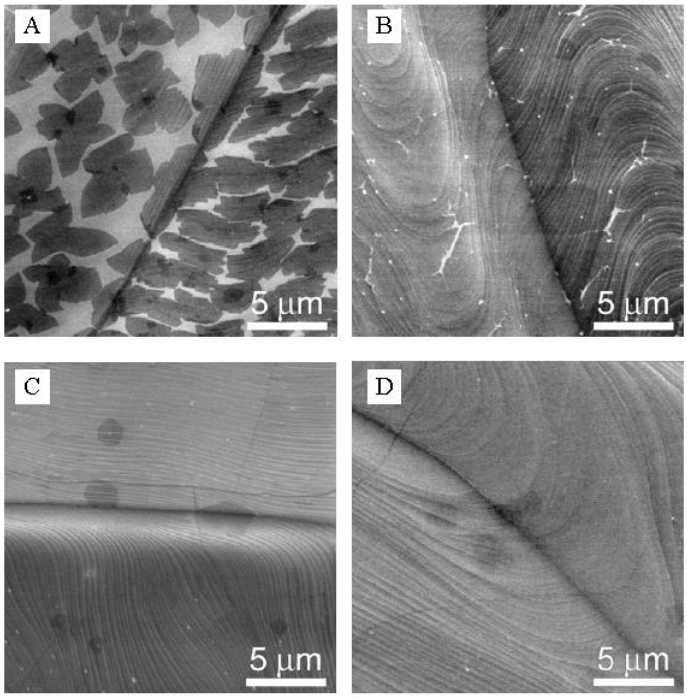

Figure 2.10 : SEM images of graphene grown on Cu taken at (a) 1 min (b) 2.5 mins (c) 10 mins (d) 60 mins[45]

2.6 Graphene Characterisation

Several imaging methods such as AFM, STM, TEM and SEM have been shown to be able image the surface of graphene, as well as determine the thickness and quality of graphene that is synthesized. While some techniques such as AFM, STM, TEM have proven useful in studying the structural quality of graphene, and others like SEM, TEM and AFM have been employed to gain an understanding of the thickness of graphene flakes [1][8][13][14], for day to day working with graphene flakes many of these techniques are either far too time consuming , have low throughput, need special sample preparation or are not as reliable in determination of thickness. For ease of use as well as reliability, two techniques stand out. To enable a quick and preliminary identification of layer thickness, it is optical microscopy that is often relied upon. For a more in depth understanding and examination of the quality and thickness of graphene samples, Raman spectroscopy is used as the preferred characterisation technique. Below we give a brief description of the two techniques.

2.6.1 Optical Microscopy

Even though graphene is atomically thin, single layer graphene that is deposited on SiO_2 is visible using an optical microscope. This is because monolayer graphene that is laid on SiO_2 creates a small cavity that adds an optical length to the light that reflects off the surface of the substrate. This adds a small contrast to the image, thus allowing us to discern its presence. Interestingly, the contrast observed corresponds strongly to the thickness of the SiO_2 layer, the wavelength of light used to illuminate the sample as well as the angle of illumination. [11][12]. Importantly, the contrast between single, bi and tri layer graphene flakes are also have noticeably different contrasts under an optical microscope.

This fact is especially useful for the identification of the yield of flakes during the mechanical exfoliation of graphene from bulk graphite. Under white light the contrast between each layer of graphene is about 5%, which can be improved to about 8-10% by using passing it through a wide band green filter. [11]

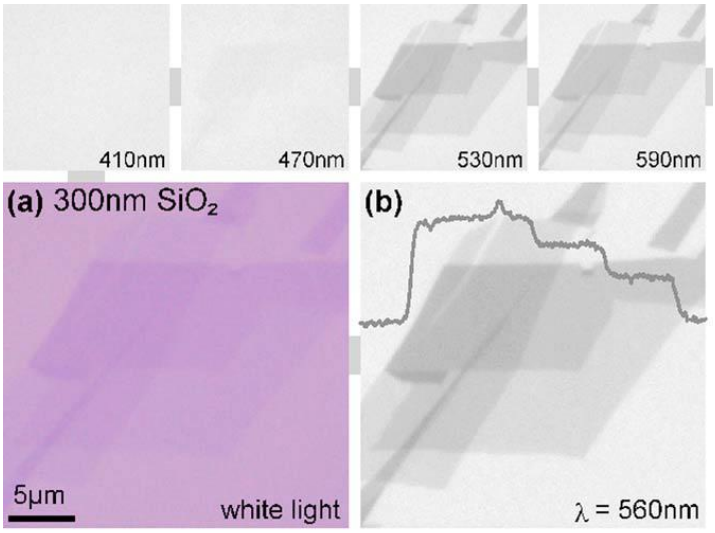

Figure 2.11 : Graphene crystallites on (a) 300 nm SiO2 imaged with white light (b) the same 300nm SiO_2 imaged with green light. Top panels show the same flake as in (a) and (b) but illuminated with light of various wavelengths. The trace in (b) shows step-like changes in the contrast for 1, 2, and 3 layers. [11]

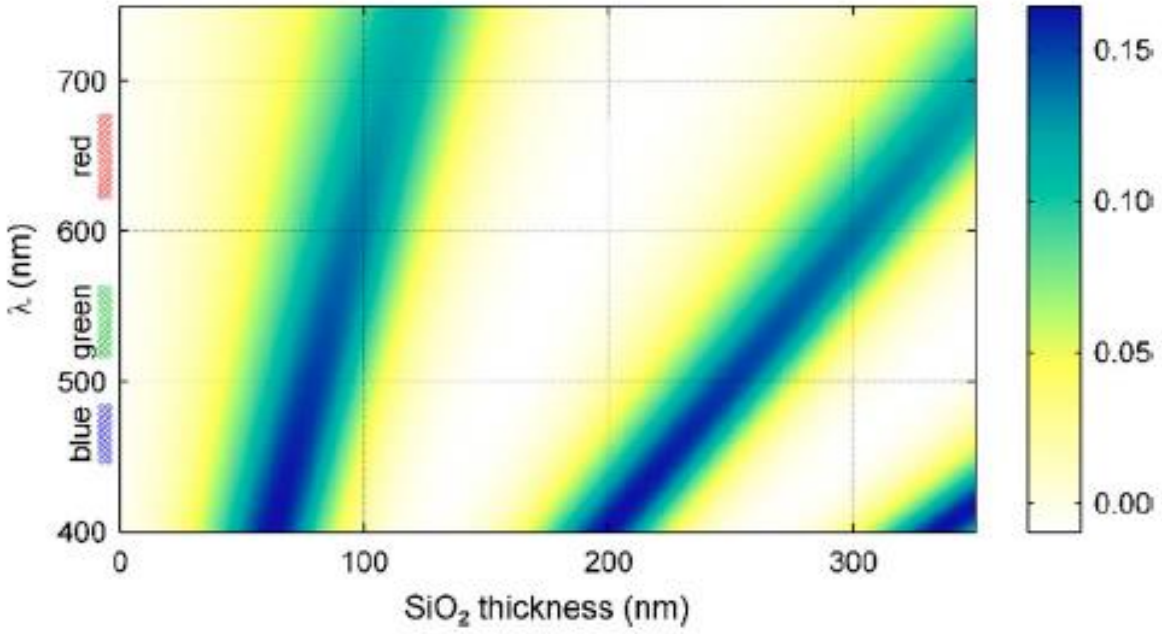

Figure 2.12: Colour plot of contrast of graphene on SiO_2 as a function of wavelength and SiO_2 thickness. [11]

2.6.2 Raman Spectroscopy

Raman spectroscopy is one of the most reliable techniques used to characterize graphene. It is based on the Raman Effect, discovered in 1928, which involves the inelastic scattering of photons in the near-infrared, visible and near UV regions. When photons impinge upon a sample, they are absorbed, and excite the molecules in the material to a higher energy state. When the molecules relax, they re-emit photons and these photons can either be of the same frequency as the incident photon or can be shifted. The emission of photons that correspond to the same frequency of the incident light is due an elastic scattering process that is known as Rayleigh Scattering. The photons with a shifted frequency are caused by an inelastic scattering effect know as Raman Scattering. This occurs when molecules relax to a different energy state but not back to the ground state. While most photons undergo Rayleigh Scattering, a small proportion of photons emitted are shifted to higher (anti-Stokes scattering) and lower (Stokes scattering) frequencies.

This shift in observed frequency of emitted light is called the Raman shift and gives us information about the different vibrational and rotational states of the material. The Raman shift is typically denoted by Δw, has a unit of cm^{-1} and is given by the equation,

$$\Delta w = \frac{1}{\lambda_0} - \frac{1}{\lambda_1} \qquad [2.10]$$

Where λ_0 and λ_1 correspond to the wavelengths of the incident photon and the emitted photon respectively.

In a Raman spectrometer, the sample is illuminated with light from a carefully calibrated laser source to one particular frequency. The light that is reflected back from the sample is then collected by a detector which measures the intensity of reflected light for certain specific shifts in frequency. This is depicted in the data as intensity peaks corresponding to a particular shift, which is the Raman shift(cm^{-1}) .

Raman spectroscopy allows us to probe the chemical composition and structure of materials as well as gain information about its phonon spectra. It is particularly versatile because it can be used for samples in solid, liquid and gaseous state. For graphene, it is the preferred method of characterisation because of that fact that is quick and non-destructive of the samples, and acts as a powerful tool to determine (a) the no. of layers in a graphene flake (b) the amount of doping as well as the density of defects and impurities in the sample and (c) amount of strain induced in the sample. [14,15,16]

The Raman spectrum of graphene is marked by the presence of three prominent intensity peaks. The G peak appears at about ~1580 cm^{-1}, the 2D peak at ~2690 cm^{-1} and the D peak at 1350 cm^{-1}. In graphene, when light impinges upon the sample, electrons are photo excited by an incident photon, and subsequently relax back to their original state through Rayleigh scattering. Alternately, they may also relax and lose energy by scattering on a phonon – this is referred to as resonant Raman Stokes scattering. The G peak in graphene spectra occurs as a result of the in-plane vibration of sp^2 hybridised carbon atoms in graphene. It is a first order intra-valley scattering process and is the most prominent feature of graphitic materials. When an electron in the valence band is excited into the conduction band by a photon, it scatters a low momentum phonon at the Γ point. It then recombines with the hole to emit a lower energy photon. It can alternatively be thought of as relaxing to a lower energy virtual state before finally recombining with a hole.

The 2D peak in graphene, unlike for the G-peak, arises as a result of a double resonance process that involves the inter-valley scattering of high energy phonons near the K point and is very prominent in single and few layer graphene. In this case an electron from one valley scatters to another adjacent Dirac cone, via an optical phonon and subsequently scatters again via another optical phonon before it relaxes back to its original state. The shape and intensity of the 2D peak are also used to understand how many layers are present in the graphene sample being measured. As shown in Fig. 2.13 , Mono-layer graphene has a distinctive and sharp 2D peak, which is nearly twice the

intensity of the G peak. Furthermore, there is an evolution of the 2D peak with the number of layers and this allows us to identify and characterize the thickness of the sample based on its Raman Spectra.

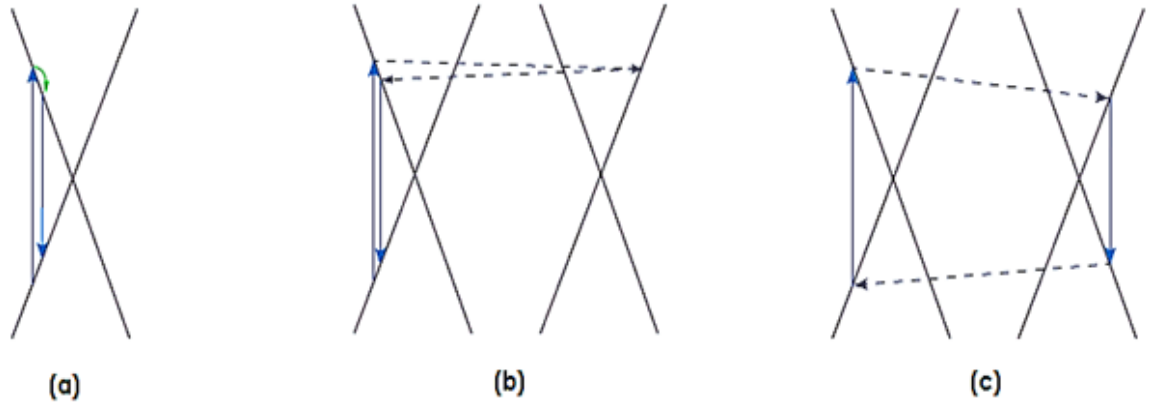

Figure 2.13 : A schematic showing the different electronic excitation and transition processes for monolayer graphene in (a) G peak (b) D peak (c) 2D peak.

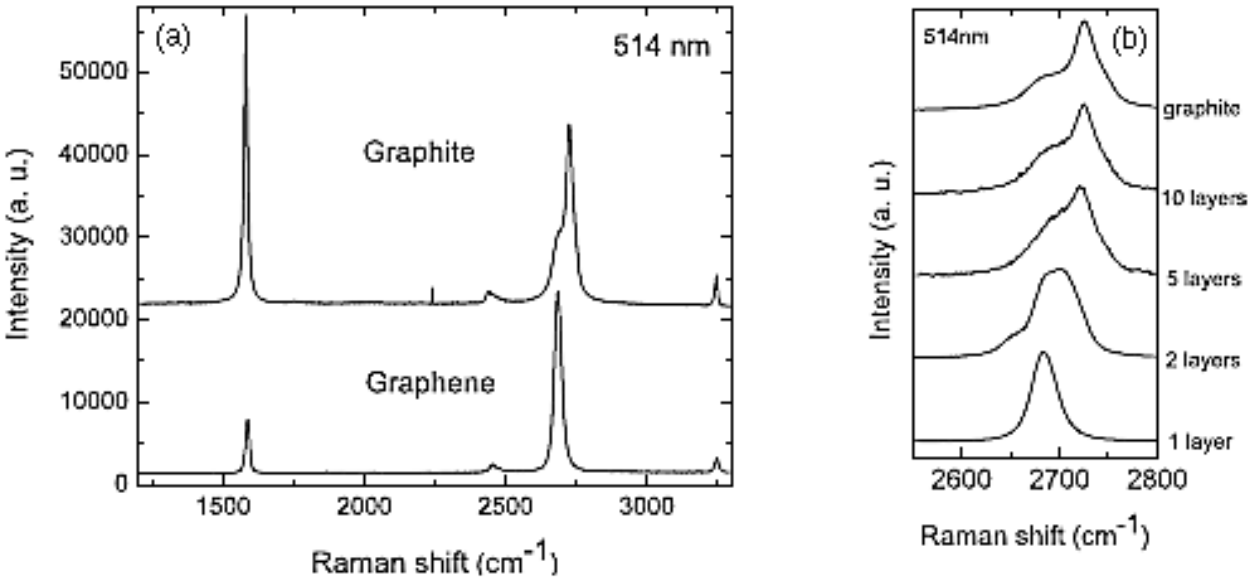

Figure 2.15: (a) Raman spectra for graphene and bulk graphite (b) The evolution of the 2D peak with increasing layers of graphene [14]

In pristine graphene, the D peak of the spectra is absent. This implies that the D peak is induced by defects and imperfections in the graphene lattice. Like the 2D peak, the D peak is also a result of a double resonant scattering mechanism. When an electron is excited, it is scattered into another valley. It returns to its original valley by scattering off short-range scatterers such as impurities and defects. This shifts its momentum considerably and it returns to its original valley to then relax and recombine to a hole, thus emitting a photon. In pristine graphene, the zone-boundary phonons that participate in this process do not satisfy the Raman fundamental selection rule and therefore the D peak cannot be seen. Furthermore, by analysing the ratio of the intensity of the D peak to intensity of the G peak, we can gain an quantitative understanding of the density of defects in a given sample of graphene [17].

In conclusion, we can see that Raman spectroscopy is a powerful and non-destructive tool with high throughput for the characterization of graphene samples. It can give us an accurate indication of the thickness/no. of layers of the sample, as well as tell us about the quality of the sample in terms of defects and impurities in the system.

2.7 Bibliography

1. Novoselov, K. S., Geim, A. K., Morozov, S. V., Jiang, D, Zhang, Y., Dubonos, S. V.; Grigorieva, I. V., Firsov, A. A. Science 306 (5696): 666–669
2. P. R. Wallace. The band theory of graphite. Physical Review, 71(9):622, 1947
3. L. D. Landau. Zur theorie der phasenumwandlungen ii. Physikalische Zeitschrift der Sowjetunion, 11:26, 1937.
4. R. E. Peierls. Quelques proprietes typiques des corpses solides. Annales de l'Institut Henri Poincare, 5:177, 1935.
5. N. D. Mermin. Crystalline order in two dimensions. Physical Review, 176(1):250, 1968.
6. Venables, J. A., Spiller, G. D. T. & Hanbucken, M. Rep. Prog. Phys. 47, 399–459 (1984)
7. M. S. Dresselhaus and G. Dresselhaus. Advances in Physics, 51(1):1, 2002
8. Novoselov, K. S. et al. Proc. Natl Acad. Sci. USA 102, 10451–10453 (2005)
9. A. H. Castro Neto, F. Guinea, N. M. R. Peres, K. S. Novoselov, and A. K. Geim Rev. Mod. Phys. 81, 109
10. A. K. Geim & K. S. Novoselov Nature Materials 6, 183 - 191 (2007)
11. P. Blake, E. W. Hill, A. H. Castro Neto, K. S. Novoselov, D. Jiang,R. Yang, T. J. Booth and A. K. Geim APL 91, 063124 2007
12. V. Yu and M. Hilke Appl. Phys. Lett. 95, 151904 (2009)
13. Vidya Kochat, Atindra Nath Pal, E. S. Sneha, Arjun Sampathkumar, Anshita Gairola, S. A. Shivashankar, Srinivasan Raghavan and Arindam Ghosh J. Appl. Phys. 110, 014315 (2011)

14. A. C. Ferrari, J. C. Meyer, V. Scardaci, C. Casiraghi, M. Lazzeri, F. Mauri, S. Piscanec, D. Jiang, K. S. Novoselov, S. Roth, and A. K. Geim Phys. Rev. Lett. 97, 187401

15. A. Das, S. Pisana, B. Chakraborty, S. Piscanec, S. K. Saha, U. V. Waghmare, K. S. Novoselov, H. R. Krishnamurthy, A. K. Geim, A. C. Ferrari & A. K. Sood Nature Nanotechnology 3, 210 - 215 (2008)

16. Jakob Zabel, Rahul R. Nair, Anna Ott, Thanasis Georgiou, Andre K. Geim, Kostya S. Novoselov, and Cinzia Casiraghi Nano Lett., 2012, 12 (2), pp 617–621

17. L. G. Cançado, A. Jorio, E. H. Martins Ferreira, F. Stavale, C. A. Achete, R. B. Capaz, M. V. O. Moutinho,A. Lombardo, T. S. Kulmala, and A. C. Ferrari Nano Lett., 2011, 11 (8), pp 3190–3196

18. Yuan Huang, Eli Sutter,Norman N. Shi, Jiabao Zheng, Tianzhong Yang, Dirk Englund, Hong-Jun Gao, and Peter Sutter ACS Nano, 2015, 9 (11), pp 10612–10620

19. A.K Geim Science 19 Jun 2009: Vol. 324, Issue 5934, pp. 1530-1534

20. Alfonso Reina, Xiaoting Jia, John Ho, Daniel Nezich, Hyungbin Son, Vladimir Bulovic, Mildred S. Dresselhaus and Jing Kong Nano Lett., 2009, 9 (1), pp 30–35

21. Keun Soo Kim , Yue Zhao, Houk Jang, Sang Yoon Lee, Jong Min Kim, Kwang S. Kim, Jong-Hyun Ahn , Philip Kim , Jae-Young Choi & Byung Hee Hong Nature 457, 706-710

22. Xuesong Li, Weiwei Cai, Jinho An,Seyoung Kim, Junghyo Nah,Dongxing Yang,Richard Piner, Aruna Velamakanni,Inhwa Jung, Emanuel Tutuc,Sanjay K. Banerjee,Luigi Colombo, Rodney S. Ruoff Science, 324(5932):1312, 2009.

23. Xiaohong An, Fangze Liu, Yung Joon Jung, and Swastik Kar J. Phys. Chem. C, 2012, 116 (31), pp 16412–16420

24. Gregory W. Cushing, Viktor Johánek, Jason K. Navin, and Ian Harrison J. Phys. Chem. C, 2015, 119 (9), pp 4759–4768

25. Phaedon Avouris and Christos Dimitrakopoulos Materials Today Volume 15, Issue 3, Page 86–97

26. Ajay Kumar and Chee Huei Lee Synthesis and Biomedical applications of http://dx.doi.org/10.5772/55728

27. Bae S, Kim H, Lee Y, Xu X, Park JS, Zheng Y, Balakrishnan J, Lei T, Kim HR, Song YI, et al. Nat. Nanotechnol. 2010 Aug, 5(8):574-8

28. Claire Berger , Zhimin Song , Tianbo Li , Xuebin Li , Asmerom Y. Ogbazghi , Rui Feng , Zhenting Dai , Alexei N. Marchenkov , Edward H. Conrad , Phillip N. First , and Walt A. de Heer J. Phys. Chem. B, 2004, 108 (52), pp 19912–19916

29. C. Berger, Z. M. Song, X. B. Li, X. S. Wu, N. Brown, C. Naud, D. Mayo, T. B. Li, J. Hass, A. N. Marchenkov, E. H. Conrad, P.N. First, and W. A. de Heer, Science 312 (2006) 1191-1196

30. Dmitry V. Kosynkin, Amanda L. Higginbotham, Alexander Sinitskii, Jay R. Lomeda, Ayrat Dimiev, B. Katherine Price & James M. Tour Nature 458, 872-876 (16 April 2009)

31. N. Zhan, M. Olmedo, G. Wang, and J. Liu, Carbon, vol.49, no. 6, pp. 2046–2052, 2011

32. H.He, J. Klinowski,M. Forster, andA. Lerf, Chemical Physics Letters, vol. 287, no. 1-2, pp. 53–56, 1998.

33. M. J. McAllister, J. L. Li, D. H. Adamson et al Chemistry of Materials, vol. 19, no. 18, pp. 4396–4404, 2007.

34. D. Sheng, L. Sheng, and Z. Weng. Physical Review B, 73(23):233406, 2006

35. N. Peres, F. Guinea, and A. H. C. Neto. Physical Review B, 73(12):125411, 2006.

36. J. H. Chen, C. Jang, S. Adam, M. S. Fuhrer, E. D. Williams, and M. Ishigami. Charged-impurity scattering in graphene. Nature Physics, 4(5):377, 2008.

37. Mikhail I Katsnelson , Graphene – Carbon in Two Dimensions Cambridge University press 2012

38. J. W. K los, I. V. Zozoulenko, *Phys. Rev. B* 82, 081414 (2010).

39. S. V. Morozov, K. S. Novoselov, M. I. Katsnelson, F. Schedin, D. C. Elias, J. A. Jaszczak, and A. K. Geim. Physical Review Letters, 100(1):016602, 2008.

40. K. S. Novoselov et al., Nature 438, 197 (2005)

41. Y. W. Tan et al., Phys. Rev. Lett. 99, 246803

42. E. H. Hwang, S. Adam, and S. Das Sarma, Phys. Rev. Lett. 98, 186806 (2007).

43. M. I. Katsnelson and A. K. Geim, Phil. Trans. R. Soc. A 366, 195 (2008)

44. K.I. Bolotin , K.J. Sikesb , Z. Jianga,d , M. Klimac , G. Fudenberga , J. Honec P. Kima , H.L. Stormera,b,e Solid State Communications 146 (2008) 351–355

45. A. Reina, X. Jia, J. Ho, D. Nezich, H. Son, V. Bulovic, M. S. Dresselhaus, and J. Kong 2009. Nano Letters, 9(1):30, 2009.

46. X. Li, W. Cai, J. An, S. Kim, J. Nah, D. Yang, R. Piner, A. Velamakanni, I. Jung, E. Tutuc, S. K. Banerjee, L. Colombo, and R. S. Ruoff Science, 324(5932):1312, 2009.

47. N. Petrone, C. R. Dean, I. Meric, A. M. van der Zande, P. Y Huang, L. Wang, D. Muller, K. L. Shepard, and J. Hone. Nano Letters, 12(6):2751, 2012.

48. Y. Ogawa, K. Komatsu, K. Kawahara, M. Tsuji, K. Tsukagoshi, and H. Ago. Nanoscale, 6(13):7288, 2014.

49. C. Lee, X. Wei, J. W. Kysar, and J. Hone. Science, 321(5887):385, 2008.

50. I. W. Frank, D. M. Tanenbaum, A. M. van der Zande and P. L. McEuen J. Vac. Sci. Technol. B 25, 2558 (2007)

51. F. Bonaccorso, Z. Sun, T. Hasan and A. C. Ferrari Graphene photonics and optoelectronics Nature Photonics Vol4 Sept. 2010

52. Rajni Garg, Naba K Dutta, Namita Roy Choudhury Nanomaterials 2014, 4, 267-300

53. S. Das Sarma, Shaffique Adam, E.H. Hwang, Enrico Rossi Rev. Mod. Physics, VOL 83, Apr–Jun 2011

Chapter 3

Device Fabrication and Methods

3.1 Introduction

In Chapter 2, the different physical and electrical properties of graphene were discussed, as well as the ways that graphene can be synthesized, and its quality characterized. In order to perform experiments that explore the sensing applications of graphene, strong emphasis is placed on the provenance of the graphene sample, the quality of graphene sheet, the method of synthesis utilised, and the fabrication of the device itself. This chapter enumerates all the above-mentioned aspects in order to obtain a device ready for experiments and describes in detail the three different graphene-based devices that were developed for experiments as described in Chapters 4 -6.

The fabrication process to develop a graphene-based device begins with the question of how to harvest graphene. The most commonly used method of obtaining high-quality graphene devices is by micro-mechanical exfoliation of graphene from bulk graphite. The high quality and exceptional electrical conductivity that is characteristic of this type of graphene makes it the first choice for many applications. [1] However, while the technique yields high quality at a low-cost and is extremely simple, there are a few drawbacks with this method that make it less suitable for some applications.

Firstly, the yield of monolayer graphene is low. The transfer of flakes usually results in only a small percentage of mono-layer graphene flakes, while most of the substrate is typically covered with multi-layer flakes and much thicker flakes of graphite. Secondly, the process of identification of these flakes is also quite time-intensive and difficult, and the difficulties are compounded when depositing the flakes on to transparent substrates such as glass or quartz. Thirdly, the flake size produced by exfoliation is variable and cannot be precisely controlled and is typically on the order of 10-100 μm. [2][3][4]

This becomes an impediment for certain device applications that require large area flakes. And while there has been research to show that flakes of up to 100s of microns in length can be produced by using special techniques for cleaning and treating the substrate as well as the bulk HOPG, the yield of these flakes are still quite low and are limited to a few large flakes per substrate [5]. Finally, the positioning of the flakes is also a chance occurrence which has an impact on the device geometry, especially for applications which require large-surface area.

Chemically vapour-deposited graphene offers a good alternative for applications which require large-area graphene, offering uniformly large-area (in the order of 100s of cm^2) ,scalable size, roll-to-roll production, good quality (mobilities upto 50,000 $cm^2 V^{-1} sec^{-1)}$, controllable layer thickness as well as choice of substrate.[2][3][4] While there are drawbacks, including high cost of production, and much higher defect densities than mechanically exfoliated graphene, overall, the benefits of CVD grown graphene are significant. [3][4]

In this chapter, all three graphene-based devices that were developed necessitated large-Area graphene flakes and therefore, CVD graphene was used in the fabrication of all the devices. Section 3.2 describes the use of large area graphene flakes and the fabrication and characterization of graphene on glass electrodes for the electrochemical sensing applications that are detailed in chapter 4. Section 3.3 details the fabrication and characterization of the large area graphene surfaces used for the electrical sensing of biomolecules described in chapter 5. And finally, section 3.4 describes the development, fabrication and

characterization of graphene transistor arrays that are embedded with a microfluidic channel as used in experiments in Chapter 6.

3.2 Fabrication of Graphene Electrodes

This section describes the device fabrication and the development of a graphene-on-Glass, transparent, conducting electrode for the purpose of performing electrochemical experiments (as detailed in chapter 4). As these devices were intended to be used in an electrochemical cell, it was important that the graphene sheet was transferred onto an electrically and chemically inert substrate that wouldn't interact with any of the chemical species in the cell in any way. Moreover, for the development of an electrochromic device, to observe changes in the transparency of the graphene substrate it was necessary that the substrate was optically transparent. With these two requirements in mind, the sections below describe the transfer of CVD grown graphene on Cu to a glass substrate, contact deposition and the characterization of the graphene sample.

3.2.1 Graphene Transfer

The transfer of graphene from the transition metal it is grown on to a suitable substrate is an integral part of the fabrication of graphene devices from CVD grown graphene because the graphene on metal has very limited usage while still attached to its metal support. [3][6] The 'PMMA technique' of transfer from Cu was first reported by Ruoff et al. [3], who showed that a polymer support could be used to adhere to the graphene film and would enable etching away of the metal support substrate, followed by the transfer of the graphene film onto the desired substrate. Since then several groups have reported improvements and modifications to this technique aimed at reducing the introduction of impurities and defects during the transfer process that affect the quality of the graphene devices that can be obtained. [4][6] Below we describe the various steps involved in the transfer in detail.

Initial attempts at growing CVD graphene on Cu in the lab yielded discontinuous films with small grain sizes and numerous multilayer grains. Therefore, for the device fabrication of graphene on glass electrodes, CVD grown graphene as purchased from Graphene Supermarket (single layer CVD grown graphene on Cu 2"x2" foil). The graphene foil was characterized using optical microscopy and Raman spectroscopy (see section 3.2.3) to verify the quality of the film. The foil was then carefully cut into the appropriate sizes depending on the final desired size of the graphene electrode.

3.2.1.1 Spin-Coating PMMA

In order to transfer graphene on to an alternate substrate, a polymer resist known as Polymethyl methacrylate (PMMA) is used. It is a versatile, transparent thermoplastic and is commonly used as a positive resist for electron-beam lithographic purpose. PMMA is acquired dissolved in solution (typically in anisole or chlorobenzene) and can be used to form a thin film over a given substrate using a spin-coater. The thickness of the film that is formed depends on the molecular weight of the polymer that is used in solution (Typically either 495,000 (495K) or 950,000 (950K)), the concentration of the polymer in solution as well as the speed at which the spinner rotates and the duration of spin time.

A 2" x 2" square of 20 µm Cu foil with monolayer graphene grown on it was acquired from Graphene Supermarket. From this larger foil, 10mm x 10mm pieces of Gr/Cu are carefully cut out to give foils of 1cm^2 area. The foil is placed on a 15 cm^2 cut out piece of mild-adhesive Nitto blue tape such that underside of the foil is covered by the tape. In the case of some devices where a larger area of graphene was required, the size of the Nitto tape is adjusted accordingly. This has two purposes – it peels away graphene grown on the underside when removed (refer to sec. 3.2.1.2) and it acts as a support for the Gr/Cu foil to be placed on the spinner and prevents the foil from crumpling due to the pressure of the vacuum.

PMMA 950K A4 (4% in anisole) solution is dropped on the top side of the foil and the spinner is run to 4000rpm for 1 min (10 sec to ramp up, 5 secs to ramp down

and 45 sec of constant speed) to form a resist layer of about 200nm thickness. The Gr/Cu are then separated from the support tape and placed on to a hot plate. This is known as 'baking' and has the effect that the polymer layer melts, recrystallizes and re-arranges itself to take on the topography of the underlying Gr/Cu foil. Although different groups have reported better transfer results for different baking temperatures, some even suggesting omitting the baking step [7], no significant difference in tear density was observed for baking temperatures from 160 to 180 ˚C and room temperature curing.

Baking times from 1min to 10mins were employed. Baking times of longer than 10 mins yielded a more rigid polymer layer which did not conform well to the transfer substrate and therefore impeding effective transfer. In these fabrication steps, a suitable baking temperature and time was found to be 180˚C for 2 mins followed by curing of the film for 1 hour in ambient cleanroom conditions. This yielded a film of PMMA-supported graphene, as depicted in Fig 3.1(b), which after etching was supple but not too fragile.

3.2.1.2 Plasma-Etching

During the CVD process, graphene growth is reported to occur on both the sides of the foil. [4][6][8]. This second layer of graphene, if not removed, can interfere with the complete etching of the Cu foil. It also has been observed to adhere to the edges of the PMMA film as rolled up and folded films. This affects the transfer of the intended graphene film to the desired substrate as the folds of the second layer tends to trap lots of impurities and can be hard to separate from the PMMA edges without risking damage to the main graphene film that we want to keep defect-free.

To avoid this, the underside of the graphene foil should be stripped of its graphene growth and cleaned before the etching process can begin. This is achieved in two steps. As mentioned in Sec 3.2.1.1, a blue Nitto tape with a mild adhesive that attaches to the back of the foil removes some of the grown graphene. However, it does not remove 100% of the graphene and it does leave a tape residue as well. This can be dealt with by introducing a cleaning step using

a Reactive Ion Etcher (RIE). Here, as depicted in Figure 3.1(c) the foil is placed with the Cu-face facing upwards in the RIE chamber (JLS Mini-Lab RIE 80 etching system) and an O_2 plasma of 10W for 30 secs is used to etch away any remaining organic material on the Cu surface. The PMMA/Gr/Cu foil is now ready to be placed in an Etchant solution.

3.2.1.3 Etching Copper

Several etchant solutions have been used to etch Cu in the transfer of CVD graphene including ferric chloride ($FeCl_3$), ferric nitrate ($Fe(No_3)_3$) and ammonium per sulphate ($(NH_4)_2S_2O_8$) [7-10]. Ferric chloride and APS were tested as etchants. For comparable concentrations (0.1 M), the etch times were longer using APS and there was no visible difference in the tear and defect density under examination from optical as well as SEM microscopy. Consequently, $FeCl_3$ has been used as the main etchant solution in the transfer and this is depicted in Figure 3.1(d).

After the cleaning step in the RIE, the Cu foil is placed directly on the surface of a 0.05M $FeCl_3$ solution which is filled to the brim of a 50ml beaker. The foil floats on the surface with the Cu side in contact with the Iron Chloride solution. The etching process times depends on the concentration of the etchant solution. Fast etching tends to leave the surface rough and with higher density of defects and tears. In the case of a 0.05M solution, the film was left in the solution for 8 hours.

Once the Cu is completely eaten away by the etchant solution, the PMMA/Gr film which can be seen as a thin, transparent film is removed from the etchant solution using a borosilicate spoon. The spoon is large enough to scoop up the film and some of the etchant liquid such that the film continues to float and does not come into contact with any other material. The film is then transferred into a new griffin beaker which is filled with ultra-pure De-ionised water. It is left in this water bath for 5 mins, to achieve the effect of rinsing the graphene surface. This process is then repeated atleast 5 more times, each time the film is placed in a fresh beaker with ultra-pure DI Water so as to remove any unwanted

chemical residues. On the final round of rinsing, the film is allowed to float in water for 4 hours as depicted in Figure 3.1(e). Some groups have reported including an additional cleaning step at this juncture such as mild RCA cleaning. [7] This was tried but found to be quite aggressive and introduced tears into the graphene film. Instead, the beaker with water along with the PMMA/Gr film floating on the surface is placed on a hot plate and gradually heated to about 60 ˚C. This causes a circulation of warm ultra-pure water under the surface of the graphene and acts as a final rinsing step before the film is ready to be transferred on to the desired substrate.

3.2.1.4 Transfer of PMMA/Gr

The desired substrate (typically Si/SiO_2 or glass) on which the PMMA/Gr film is to be transferred is aggressively cleaned by first boiling in 70˚C acetone, followed by sonication in IPA and then finally with an O_2 plasma in an RIE chamber (30W , 5mins).

The PMMA/Gr film is then gently scooped out by immersing the substrate into the beaker and positioning it under the film and lifting upwards to scoop up the film from the water's surface. During this process, residual water is also transferred and the PMMA/Gr film floats on this water layer on the substrate. A modified needle (in the form of a micropipette syringe nozzle) is used to pin one end of the film down in the required position and the sample is tilted so that large drops of water are drained away as depicted in Figure 3.1(f). A thin film of water still exists between the film and the substrate and this is removed by a gentle heating process in a furnace to about 40 ˚C for 30 mins as in Fig 3.1(g). The mild heat serves to remove the excess water in a gentle way as well as helps the film flatten and adhere smoothly to the substrate.

3.2.1.5 Removal of PMMA layer

Acetone is widely used in micro/nano fabrication to dissolve PMMA films. However, using Acetone at room temperature to dissolve the PMMA films left a lot of organic residues on the surface of the graphene. Immersing, the PMMA/Gr/substrate into 70˚C, boiling acetone reduced the amount of residue on

the surface, but it did increase the no. of tears, wrinkles and cracks in the graphene sheet. An alternate chemical that can be used to dissolve PMMA is chloroform ($CHCl_3$). Using chloroform left the surface of the graphene with consistently reduced impurities on the surface. In all of the above cases, the PMMA/Gr/substrate is introduced into the solution to remove PMMA and left in solution for 1Hr, followed by rinsing in acetone and IPA before the sample is finally dried using a N_2 gun. Figure 3.1 illustrates the entire process of the transfer of graphene on the desired substrate.

3.2.2 Contact deposition

The final stage of making a graphene electrode device involves the thermal evaporation of gold (Au) so that an electrical contact can be made from the graphene surface to the rest of the circuit. Cr/Au (10nm Cr 100 nm Au) is thermally evaporated on to the graphene using a suitable mask such that a gold pad is created. In the case of these experiments, graphene was transferred on to glass slides. This was necessary because electrochemical experiments it was required to have an electrochemically/electrically inert substrate. Since the Si substrate is heavily doped, it would conduct electricity, otherwise it would offer an alternative conducting path and might shunt the graphene electrode and interfere with the response from the graphene itself.

After the gold pad was deposited on the Gr/glass substrate, a metal wire contact was made with the use of silver epoxy. The remainder of the gold pad and the conducted surface of the epoxy was insulated by using an inert epoxy resin so that the conduction path could only occur through the graphene channel. Fig. 3.2 illustrates the final design of the device. The graphene strip is elongated to have a large surface area that can be immersed into the electrolytic solution. To the naked eye the outline of the graphene sheet is easily apparent, in Fig. 3.2, it is highlighted as the contrast in the photograph is not significant.

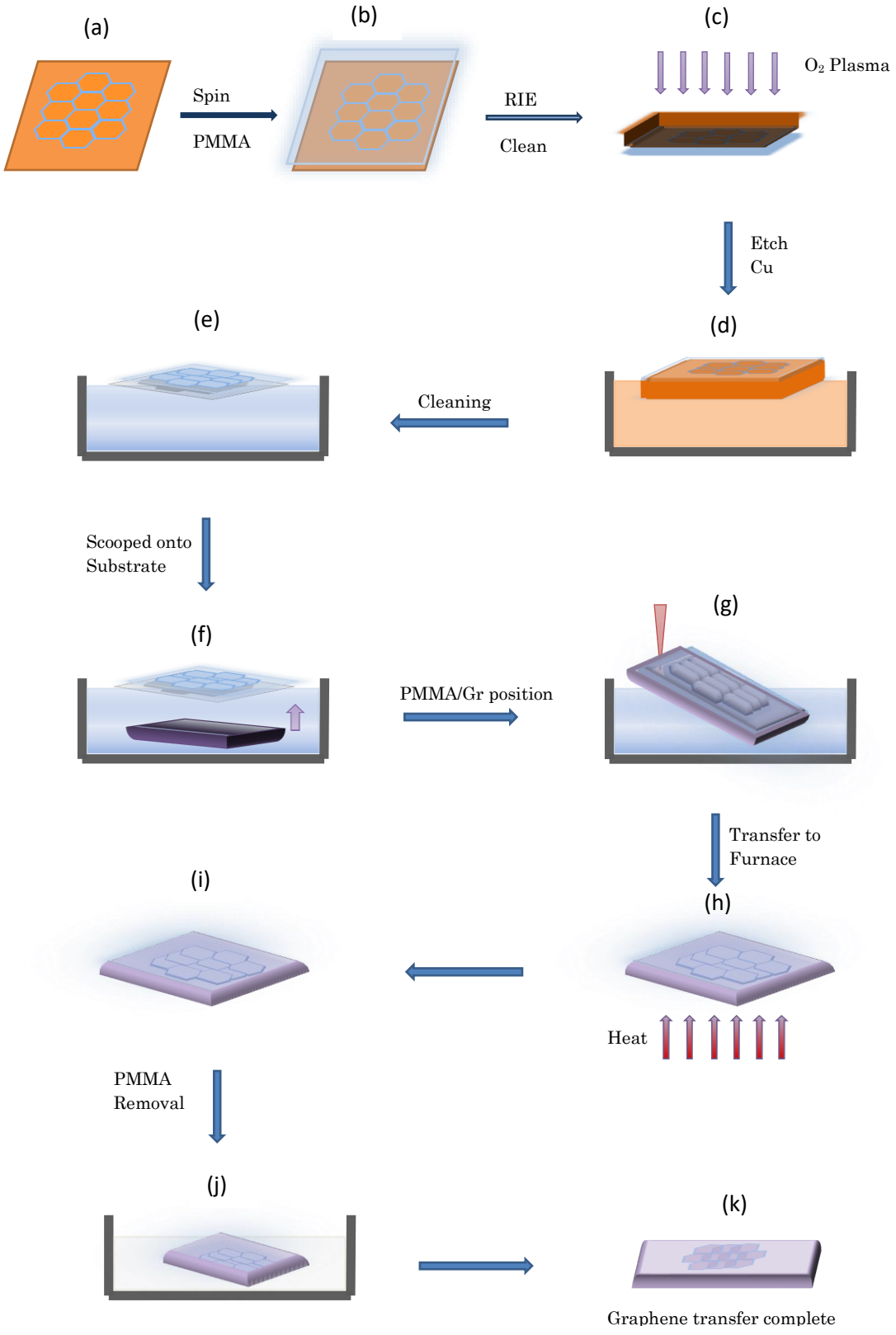

Figure 3.1: A schematic representation of the graphene transfer process from (a) as received graphene on Cu which is (b) spin coated with PMMA, followed by (c) plasma removal of graphene from the back layer. The (d) Cu is etched away and the Gr/PMMA/Tape layer is rinsed and (f) scooped onto the desired substrate, where (g) it is position and properly and (h) heated to adhere the graphene on the substrate and finally (i,j) the PMMA is removed and (k) the transfer is completed.

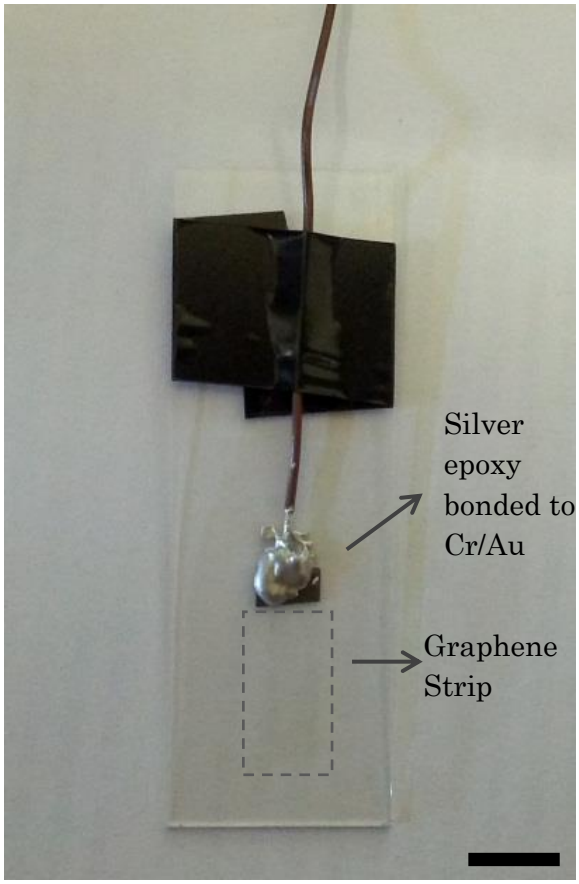

Figure 3.2: Graphene-on-glass electrode device. The image shows graphene transferred on a glass slide. (The black scale bar (bottom right) indicates 1cm.) A wire is bonded by silver epoxy to make contact with the Cr/Au contact that is deposited on one end of the faintly visible strip of graphene film.

3.2.3 Characterization of Graphene Electrodes

As discussed in section 2.6, the graphene devices are often characterized by optical microscopy and Raman spectroscopy. Fig. 3.3 shows a 200x250 µm window of graphene sheet transferred onto glass by the steps described in section 3.2.1. In fig. 3.3 (a), as a result of the transfer process, due to aggressive etching or excessive heat applied during the transfer, defects such as folds and tears are introduced. To counteract this, a gentle etch and gentle heating must be done. The chemical processing, particularly the etching of Cu and the removal of the PMMA using acetone, introduced residues and impurities. While

impurities trapped between the graphene sheet and the substrate are impossible to get rid of, the organic residues left on the surface of the graphene sheet can be removed through the process of thermal annealing. This is detailed in section 3.3.

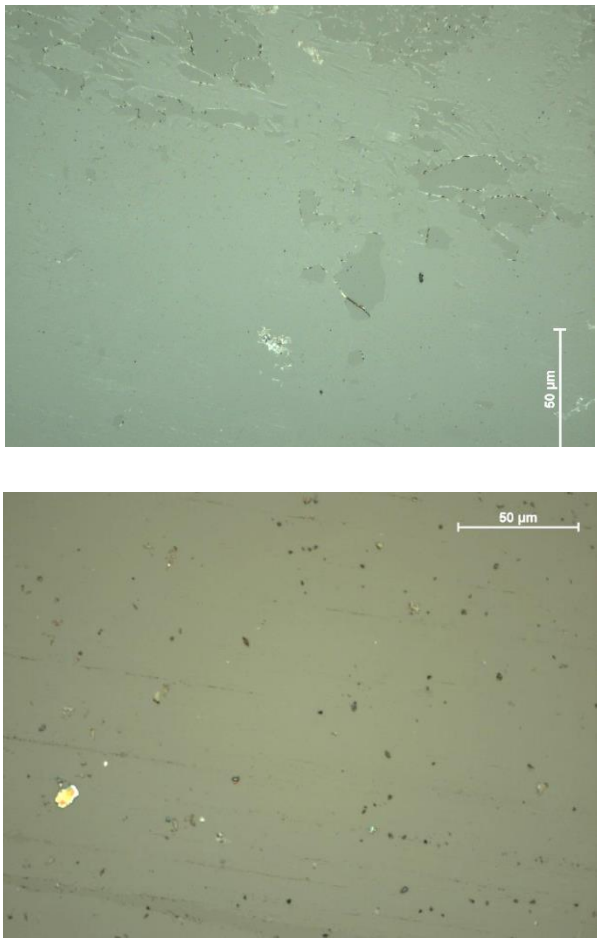

Figure 3.3: Optical images taken of large–area graphene transferred from Cu onto a glass substrate indicated tears and impurities caused during the transfer process.

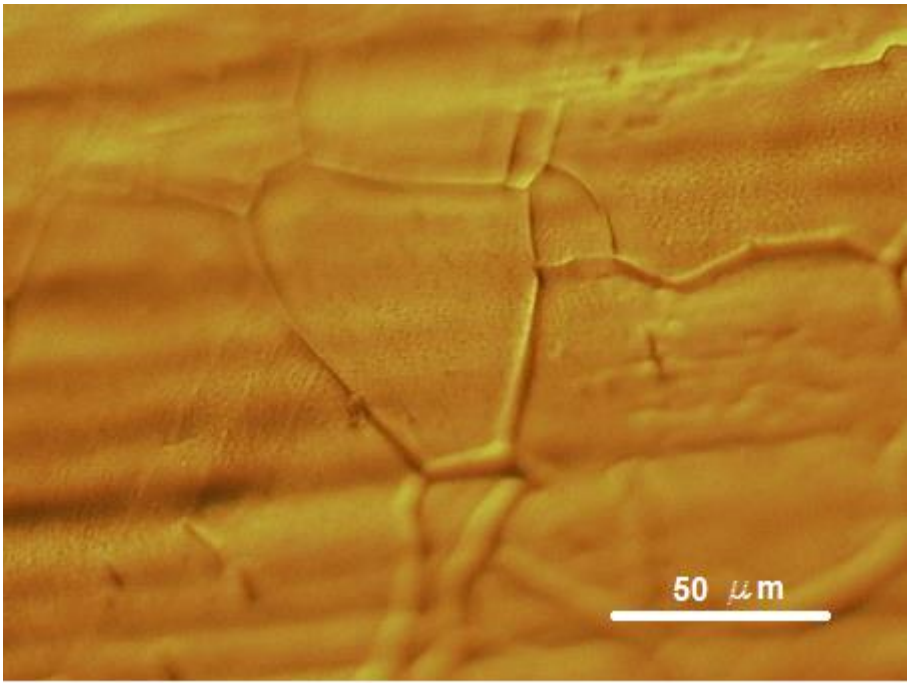

Figure 3.4: A 50x optical microscopy image of graphene on Cu foil, showing the grain boundaries on the Cu sheet, corresponding to the area where Raman spectrum was collected (in Figure 3.5)

The Raman spectra of graphene samples as received from Graphene Supermarket was taken. Figure 3.5 shows the spectrum of the as-received Gr on Cu. Due to the large background signal from the Cu, it is hard to get an accurate ratio of the G to 2D peaks to identify if the sample is indeed a monolayer. However, this can be ascertained by taking the Raman spectra of the sample after transferring it onto the desired substrate. Fig. 3.6 shows the Raman spectrum of CVD graphene using a laser of 532nm once it was transferred onto the glass slide. The data reveals the characteristic spectrum of monolayer graphene with a G-peak at 1585 cm^{-1} and a 2D-peak at 2675 cm^{-1}, where the ratio of the G-peak to the 2D peak is approximately 1:2. The Raman spectrum does indicate the presence of defects in the sample due to the presence of a significant D-peak at 1350 cm^{-1}. Another peak-ratio of importance is the D to G peak ratio. This is proportional to the density of defects, and the higher the density of defects, the greater the ratio of the D-peak to G-peak. In these samples, the likely source of the defects arises from the chemical processing involved in transferring the graphene on to the glass substrate.

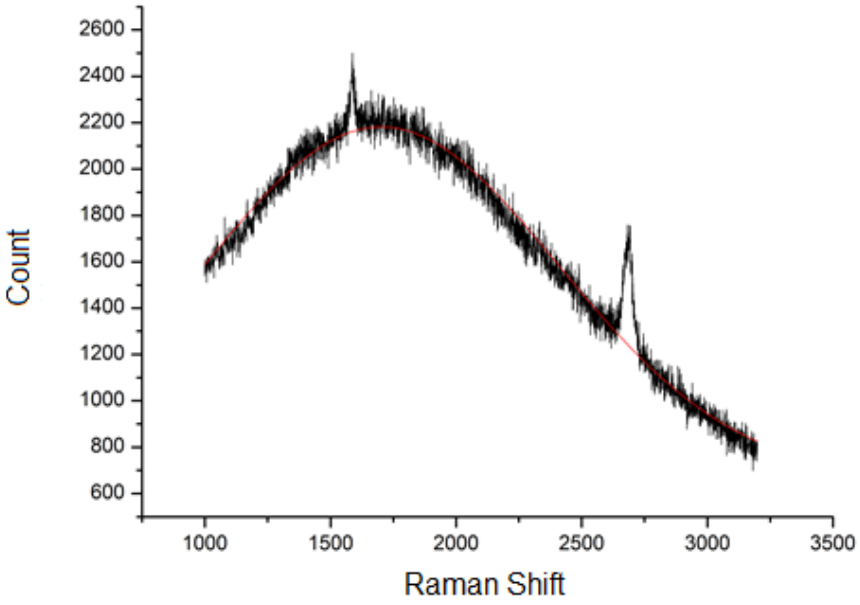

Figure 3.5 : The Raman spectrum of as received monolayer CVD graphene on Cu foil. The red line is an approximate fit for the Cu background.

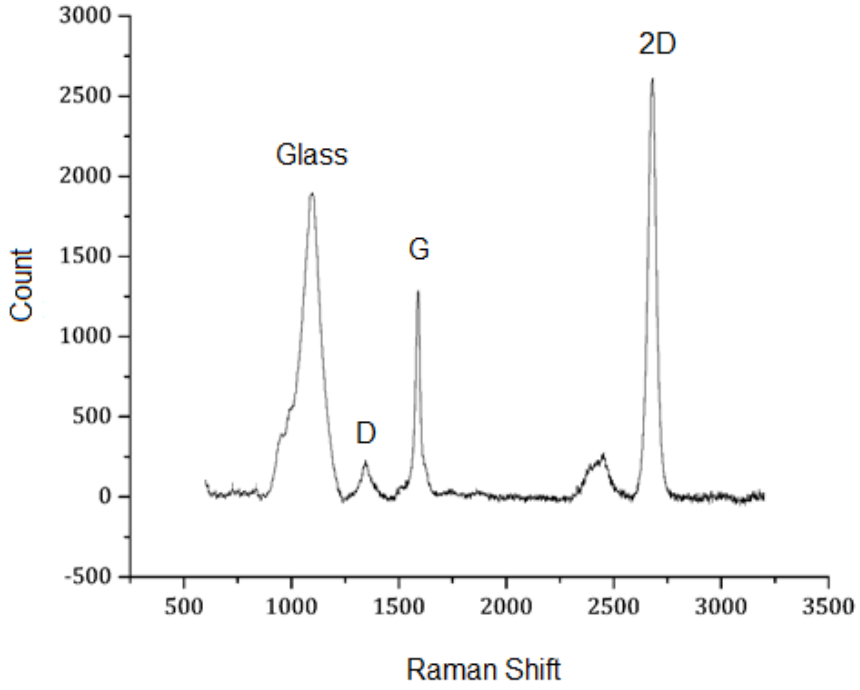

Figure 3.6: The Raman spectrum of graphene after it was transferred onto a glass substrate .

3.3 Fabrication of Large-Area Graphene Sheet Devices

The following section describes the device fabrication and the development of a large-area, graphene device. This device was designed with the goal to be able to bind large linker molecules onto its surface, which in turn allow antibodies and proteins they come into contact with, to bind to them. The device is designed in a very large hall-bar arrangement and was intended to be used to test if graphene can sense these antibodies and proteins that interact with this modified surface. One of the main design criteria required for this purpose was to have a large area sheet of graphene. More details about the design of these devices are described along with the results of the experiments carried out with these devices in Chapter 5. In this section we enumerate the keys steps of the fabrication process, Section 3.3.1 describes with the fabrication steps involved in patterning the large-area graphene sheet. Section 3.3.2 describes fabrication step utilised to contact this graphene sheet and mount and bond to it. And finally, section 3.3.3 describes the optical and Raman spectroscopy characterization used in this sample.

3.3.1 Patterning Large-Area Graphene Sheet

Commercially grown CVD graphene that was already transferred to SiO_2/Si is used a starting point for the fabrication process. As received from a commercial source, the graphene sheet covers the entire surface area of the SiO_2/Si substrate. It needs to be patterned or etched to the desired dimensions, leaving space for contacts to be drawn and deposited directly on the SiO_2 surface. This section describes the wet processing and the lithography step involved in the patterning of the graphene sheet.

3.3.1.1 Cleaning as-received Gr on Si/SiO_2 substrates

The fabrication process for the patterning of graphene commences with a cleaning step. The graphene on Si/SiO_2 is immersed into a solution of warm acetone for 10mins and placed on a hot plate at the temperature of 50C. This ensures that a circulating current of warm acetone washes over the surface, thus

rinsing the surface and ridding it of any organic residues. The sample is placed in a beaker of IPA for 5 mins to rinse off any acetone residues and then dried with a blast from a N_2 gun to remove the IPA. The sample is then transferred to a hot plate set to 80C to remove any remaining IPA.

3.3.1.2 Spin coating 2-layer resist.

A 2-layer resist is used to pattern either large areas or arrays of nanostructures with electron beam lithography. Here, a combination of a positive and a negative resist is used to pattern arrays of micron-scale strips of graphene. As illustrated in Fig. 3.7, a composite resist structure is created with a positive resist (PMMA) as the base layer. This layer acts as the sacrificial layer. A negative resist (HSQ) is spun on top of it and is exposed to the electron beam. This HSQ layer will get cross linked on exposure to the beam, will act as the protective layer and will not dissolve away when the sample is developed. The advantage of using a negative resist as the top layer is that the beam needs to be exposed only to the areas that need to be etched away, thus making it time-efficient to write in an EBL machine. HSQ is also used because of the extremely fine resolution that can be achieved with it (~10nm).

After patterning by the EBL machine, all the areas of top resist layer that were not exposed to the electron beam will get dissolved in the developer solution. The net result is, that it leaves areas of cross linked HSQ patterned in the shape of the graphene ribbons that are protected and areas where the surface is now only covered by the first resist layer (PMMA) that will be sacrificed.

Polymethyl methacrylate (PMMA) is a versatile, transparent thermoplastic and is commonly used as a positive resist for electron-beam lithographic purpose. Here, PMMA 950K A4 (4% in anisole) solution is dropped on the surface of the Gr/SiO_2/Si substrate and the spinner is run to 4000rpm for 1 min (10 sec to ramp up, 5 sec to ramp down and 45 sec of constant speed) to form a resist layer of about 200nm thickness. The substrate is then quickly transferred from the spin coater onto a hot plate with a temperature of 180C. This ensures the baking

process for the resist to set and the anisole to evaporate. The substrate is baked for 5mins and it is then ready for the second layer of resist to be spun.

The second resist layer that is spun on top is a negative resist called hydrogen silsesquioxane (HSQ). After the first layer of resist has been baked for 5 mins, a HSQ 2% solution in MIBK is pipetted onto the PMMA/Gr/SiO_2/Si substrate placed in the spin coater. The spinner is set to run to 3000rpm for 1min (10sec ramp up, 5 sec ramp down and 45 sec constant speed). This produces a very thin resist layer of around 400 Angstroms. The substrate is then quickly transferred from the spin coater onto a hot plate with a temperature of 220 C and baked for 5 mins. The substrate is now ready to be exposed to the electron beam.

3.3.1.3 Electron Beam Lithography

Electron Beam Lithography is a technique that is used to write patterns into an electron-sensitive resist layer that allows high resolution, great accuracy and with no masking required. It is a commonly used nanofabrication technique and is a crucial step in the fabrication of all kinds of nanostructures. The main principle behind this form of lithography is the exposure of a resist layer deposited on a surface, that changes in chemical composition wherever it is exposed to the electron beam. If the resist is positive in nature, the exposed area of the resist layer will be removed when it is immersed in a developer solution. If the resist is negative in nature, then all the areas of the resist that are not exposed will be removed by the developer solution. In this case, the electron beam is used to write a pattern that is designed using Autocad. When the top layer of HSQ is exposed to the electron beam, it will get cross linked and will act as a protective layer. When the sample is developed after patterning in the EBL machine, all the areas of HSQ surface that were not exposed to the electron beam get dissolved. This leaves areas of cross linked HSQ under which the PMMA and graphene layers sit and areas where the surface is now only covered by the first resist layer (PMMA).

A developer solution is specific to the resist that is being used. In the case of HSQ, a commercially available developer solution by MicroPosit called MF CD-

26 is used to remove all areas of the HSQ layer that are unexposed to the electron beam. Once the sample is removed from the EBL machine, it is transferred into a beaker containing 30ml of MicroPosit CD-26 developer. The sample is left in the beaker undisturbed for 4mins, after which it is retrieved and placed in a beaker of ultra-pure de-ionised water and rinsed to remove residues of the CD-26 and the HSQ. This step is repeated twice more to ensure that all the residues have been removed and the sample is dried with a blast from the N_2 gun and then placed on a hot plate with a temperature of 100C for 2 mins to remove any residual moisture on the substrate.

3.3.1.4 Reactive Ion Etching

Reactive ion etching is a dry etching technology that is commonly used in nanofabrication processes. In RIE, the sample is placed in a vacuum chamber where it is exposed to chemically reactive plasma. The plasma reacts with chemicals on the surface of the substrates and etches into the bulk of the material in a top-down manner. Because of the nature of the plasma, RIE can produce a strongly anisotropic etch profile, where the etch is predominantly in the vertical profile rather than the lateral. The etching capacity of an RIE system depends strongly on many parameters, including the nature of the reactive ions, the pressure, gas flow and RF power.

RIE may be used to get rid of a whole host of impurities and residues and is often employed to clean substrates as a first step in a nanofabrication process. Here we discuss its use as a plasma etcher to remove the unwanted areas of PMMA and graphene that have become exposed after the HSQ is developed. After testing a variety of recipes for exposure time and RF power, the following recipe was found to be reliably etch through and remove 200nm of PMMA and a monolayer of graphene that sits under it.

The sample is placed in the RIE chamber and pumped down to a pressure of 80mT. An O_2 flow of 10sccm, with the RF power set to 20W generates an O_2 plasma in the chamber which runs for 4mins. During this time, the cross linked

HSQ and all the layers under it are left unaffected and the exposed PMMA/Gr layer is etched away leaving a pristine SiO_2/Si substrate underneath.

3.3.1.5 Lift -Off

The final step involves removing the protective bi-layers of resist by dissolving the sandwiched PMMA layer in warm acetone which separates the resist structure on top from the graphene sheet. This is achieved by a process known as lift-off where the resist layer (PMMA) is immersed in warm acetone in a beaker and placed on a hot plate with a temperature of 60C for about 2 hours. The unwanted resist layers are lifted off as the PMMA layer slowly dissolves in the acetone, thus removing the HSQ layer along with it. After 2 hours, the substrate is gently rinsed in IPA and dried off with a N_2 gun with special care being taken as the graphene strips are now sitting on the SiO_2/Si substrate with no other support. Care and much patience must be taken during this step to ensure that there is complete lift-off and no damage or tears to the graphene sheet. The resultant graphene sheet is too large (~500 cm^2) to be viewed completely under 5x magnification in an optical microscope, however Figure 3.7 shows a schematic diagram of the fabrication process from the patterning of the graphene upto the contacting of graphene.

3.3.2 Contacting Graphene: Second lithography step and Metallization

The large-area graphene sheet is contacted by using a very large Hall-Bar arrangement of contacts. This consists of source and drain electrical contacts along with four voltage probes on the left and four voltage probes on the right. Once the graphene sheet is patterned, the next step in the process of fabrication is contacting it. This step requires a second iteration of lithography.

When the design for the graphene is drawn into the CAD file, a second layer representing the contacts is drawn as well, that is superimposed on top of the graphene sheet, this is evident in the CAD diagrams in fig. 3.8.

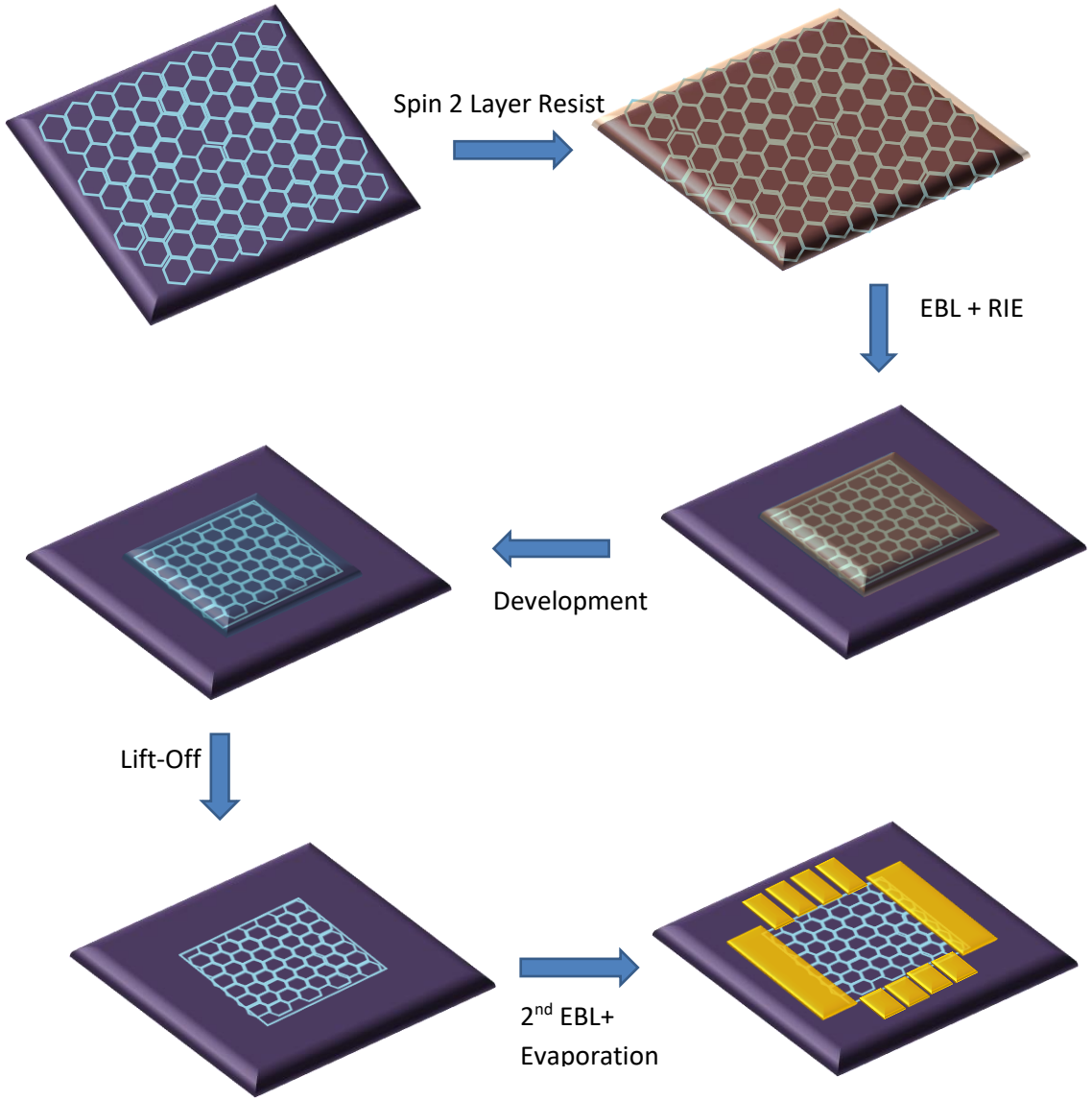

Figure 3.7: A schematic showing the steps involved in the fabrication of the large-area graphene sheet.

The second step of lithography is required to create trenches in a resist layer after the development is done, and these trenches are then filled by evaporating a metal such as Au that will allow the graphene sheet to be electrically contacted. This requires a repeat of some of the steps described above in Section 3.2.2, namely spin coating a positive resist layer, which is followed by electron beam lithography and then developing the substrate.

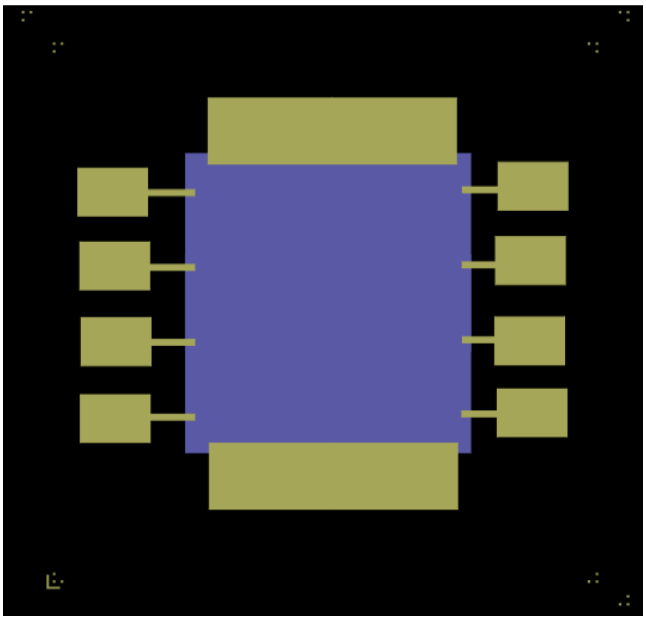

Figure 3.8 A CAD diagram of the layout of the large area graphene device.

To make these trenches, PMMA 950K A4 (4% in anisole) solution is dropped on the surface of the Gr/SiO_2/Si substrate placed in a spin coater and the spinner is run to 4000rpm for 1 min (10 sec to ramp up, 5 sec to ramp down and 45 sec of constant speed) to form a resist layer of about 200nm thickness. The substrate is then quickly transferred from the spin coater onto a hot plate with a temperature of 180C. At this stage a longer bake time is employed of about 10mins. This ensures better lift-off after the metallization process.

The substrate is then placed in the EBL machine to draw the desired pattern for the contacts into the resist layer. Following this, it is placed in a beaker filled with freshly prepared developer solution. This developed solution is specific to PMMA 950K and is prepared by mixing 15 parts IPA (Iso-propyl alcohol) , to 5 parts of MIBK (methyl iso-butyl ketone) and 1 part of EMK (ethyl methyl ketone).

The sample is immersed in this solution for 20 seconds and quickly transferred to a beaker with IPA. It is then dried with a N_2 gun and checked under the microscope to see if the development process is complete and the trenches are clean. This is essential for the metallization process to be successful as if there

are residues, then the metals will not adhere to the surface, causing significant contacting problems which are only discovered after all the processing is complete when the sample is measured.

In order to contact the graphene, thin films of metal are coated into the trenches onto the edges of the graphene sheet and are then linked to contact pads on the edges of the chip which can be bonded at a later stage. To achieve this, we use a thermal evaporator machine to deposit thin films of chromium and gold. This is done at low pressure with the sample kept in a chamber of about $1x10^{-6}$ mbar. The desired metal that requires coating is placed in a carrier boat which is typically made of tungsten. This boat is then heated up by passing a large current through it and the metal starts to evaporate.

The resulting effect is that vapourised metal particles make contact with the substrate and form a thin film all across the substrate. For these samples we have evaporated a thin film of 10nm of Cr followed by 100nm of Au. The Cr layer acts as a binding layer and is used to help the gold adhere well to the graphene and the substrate. For the quality of the thin film to be good and for the film to be uniform, two criteria are of particular importance. Firstly, it is very important that the chamber pressure is low and stays around the order of 10^{-6} mbar for the entire process of evaporation. Another important criterion is the rate at which the thin film is deposited. For the best quality films, a low rate is preferred (~ 1 As^{-1}) such that the film is grows slowly and more uniformly.

After the desired quantity of metal is deposited, which can be ascertained by the inbuilt and calibrated thickness monitor in the thermal evaporator, the chamber is vented and the sample is removed. In the evaporation process, the metal film makes direct contact with the graphene sheet as well as the substrate in the areas with no resist. The rest of the metal that has deposited lies on top of the layer of resist and needs to be removed by a lift-off process. The superfluous metal film is carried away by placing the substrate in a beaker of warm acetone on a hot plate set at 80C for 2-4 hours till all the PMMA has dissolved. The sample is then rinsed in fresh acetone twice and then finally in IPA before it is dried using a N_2 gun. Due care is given to ensure that no residues are left

behind that could affect the surface of the graphene. Following this, the substrate is then mounted on to a 44pin, 1cmx1cm chip package and the back gate is connected via silver epoxy. Wire bonding of the sample is then very carefully done to ensure no damage is done to the substrate, and connections are made from the source, drain and voltage probes to the pins on the commercially procured chip carrier package. This process is described in detail in Section 3.3.4.

3.3.3 Mounting and Bonding the sample

To study the electrical response of the graphene sheet to any molecules that it comes into contact with, it is necessary that electrical connections are made from the metallic contacts that are fabricated on the chip to the real-world electronics equipment that allow us to provide electrical inputs and monitor electrical responses. The interface that allows this to happen is a chip carrier. The chip carrier is commercially procured and here the chip is mounted onto a 44-pin sample package holder able to hold a 1cmx1cm chip.

To mount the sample correctly, the chip carrier is first washed in hot acetone, rinsed in IPA and then dried with a N_2 gun. The bottom surface of the SiO_2/Si chip is attached to the holder using silver epoxy. The epoxy is a commercially procured mixture of a silver epoxy with a hardener that is mixed in a 1:1 ratio. The silver solution is then dropped on to the chip carrier and a conductive path is traced to the gate pin (pin 7 on the commercial package) so that when the chip is placed in the carrier, the Si substrate which is p-doped and conducting can be used as an electrical back gate.

Once the chip is placed in the silver epoxy it is allowed to cure at remove temperature and hardens in the course of a couple of hours, holding the chip in place. A wire bonder is a machine that melts the tip of a gold wire and using an ultrasonic pulse at the time of contact with a metal surface, bonds the gold wire to the surface. The bonding process is a particularly sensitive part of the entire fabrication process as sometimes, the bonding can damage the substrate if too much force is applied at the point of contact with the metal pad on the substrate. In certain cases, it can even scratch the surface or puncture holes through the

metal film and into the oxide layer of the substrate, thus causing holes in the oxide layer, which make the substrate leak electrical current during measurement.

3.4 Fabrication of Graphene-based Transistor Arrays

The following section describes the device fabrication and the development of a graphene arrays on Si/SiO_2 substrates with flow channels embedded on top that allow the flow of micro-litre volume liquids across the surface of several graphene strips in an array. The experiments carried out with these devices are described in chapter 6.

This section describes the fabrication issues involved in graphene transfer for this particular sample design starting with the steps involved in achieving arrays of graphene strips. The process of contacting the patterned graphene is described, followed by the fabrication steps involved in producing micron-scale flow channels to enable the flow of liquids across the array of graphene FETs. Finally, the fabrication steps taken to complete the device and make it measurement-ready by mounting and bonding the sample to a chip carrier are described.

3.4.1 Graphene Transfer

To fabricate arrays of graphene FETs, using micro-mechanical deposition of graphene from HOPG was not feasible as the yield of monolayer graphene sheets, as well as their sizes, and their positioning were random, and could not be predetermined. Although some groups have reported methods of repositioning graphene flakes to desired locations, the high yield of large size flakes was hard to consistently achieve. Therefore, CVD graphene was used as the source of graphene, because large areas of graphene sheets could be easily transferred onto Si/SiO_2 substrates.

Initially, CVD graphene on Cu foil as sourced from graphene supermarket was used. Graphene was transferred on to the substrate according to the steps enumerated in detail in section 3.2. However, as evident in fig. 3.9 and fig. 3.10,

the results achieved were not entirely satisfactory for two reasons. Firstly, despite the most careful processing, micron scale tears and folds were hard to avoid altogether However, due to the precise positioning required, this affected the outcome of the lithography steps (section 3.4.2) used for the patterning of the graphene FET array. Secondly, chemical residues that were introduced as a result of the transfer process between the graphene sheet and the substrate could not be eliminated by any cleaning steps after the transfer was complete. This affected the quality of the graphene sheet required for these experiments. While these drawbacks did exist also in the devices developed in the previous experiment, since the impurities present were electrochemically inert, they didn't affect the outcome of the results. The tears and folds were also less significant for the graphene on glass devices, as most of the film was continuous.

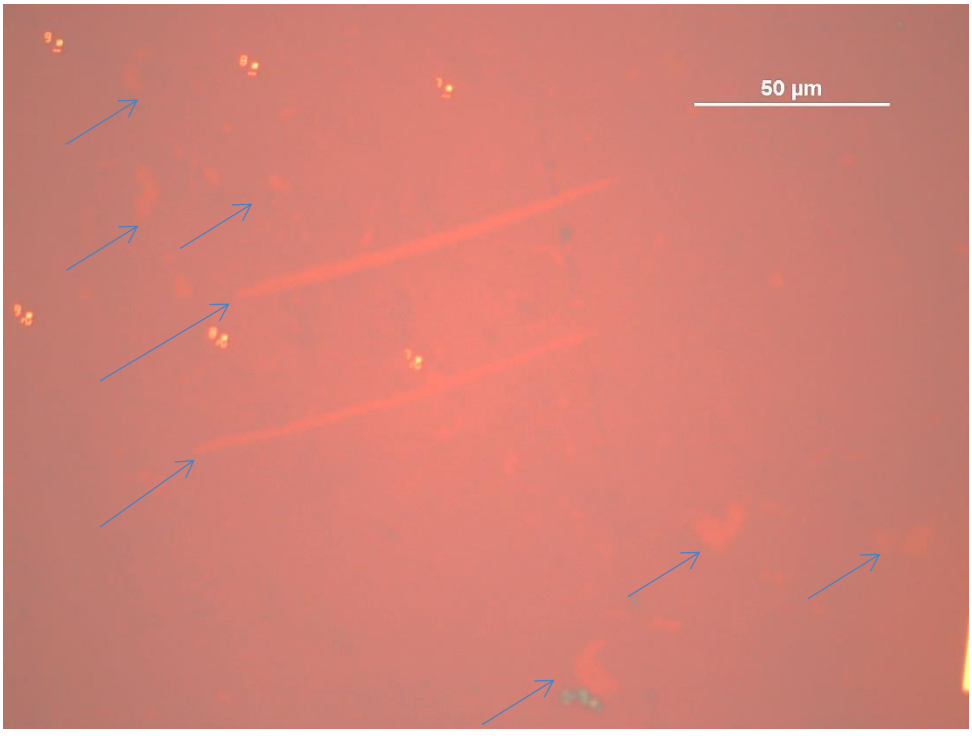

Figure 3.9: Optical microscope images of micron scale tears in the graphene sheet introduced during graphene transfer process. The arrows indicate the tears and impurities left behind.

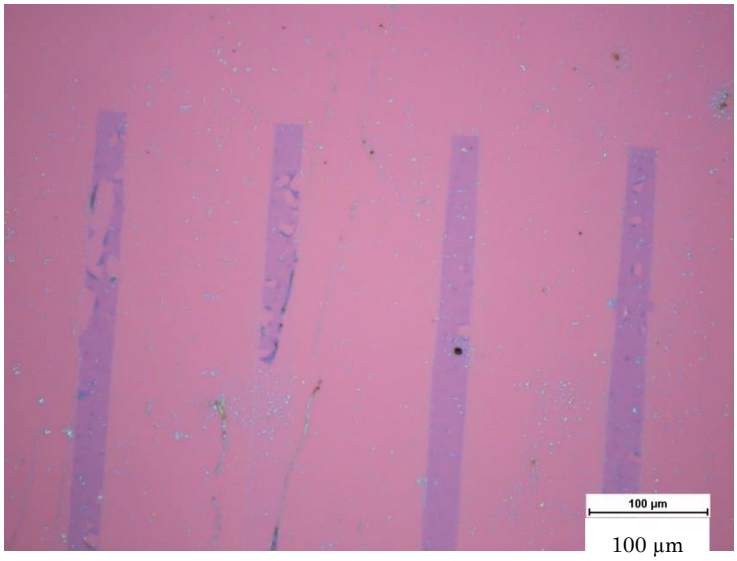

.

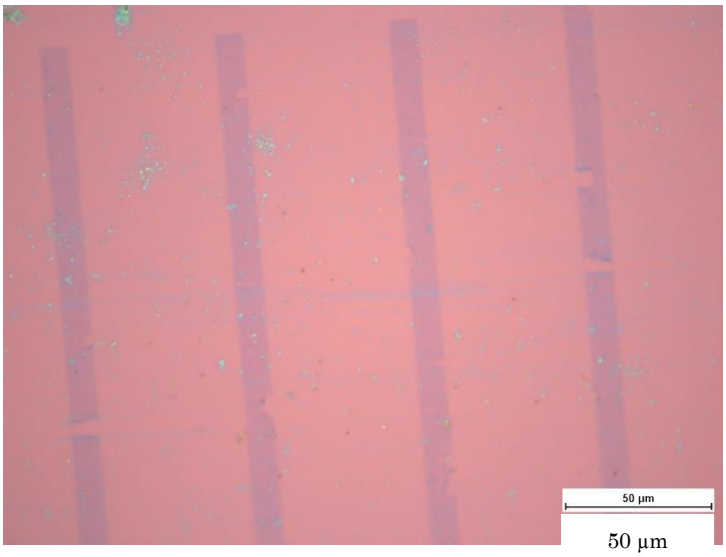

Figure 3.10: Optical microscopy image of graphene strips fabricated through EBL showing tears, residue and folds in the graphene.

3.4.2 Patterning Graphene into FET arrays

As a result of the issues with quality caused during the process of transferring of graphene (section 3.3.1), and the fabrication challenges it presented, a decision was made to procure commercially grown CVD graphene that was pre-transferred onto a $Si/Si0_2$ substrate.

The quality of the graphene sheet as procured from Graphene Supermarket was characterized optically and with Raman spectroscopy to confirm that the CVD graphene on Si/SiO_2 as received was suitable for purpose. Fig. 3.11 shows a Raman spectrum obtained from a sample of transferred graphene as received from Graphene Supermarket. The Raman spectra was captured at different regions in the sample to ensure that the film was predominantly continuous and that it was monolayer graphene.

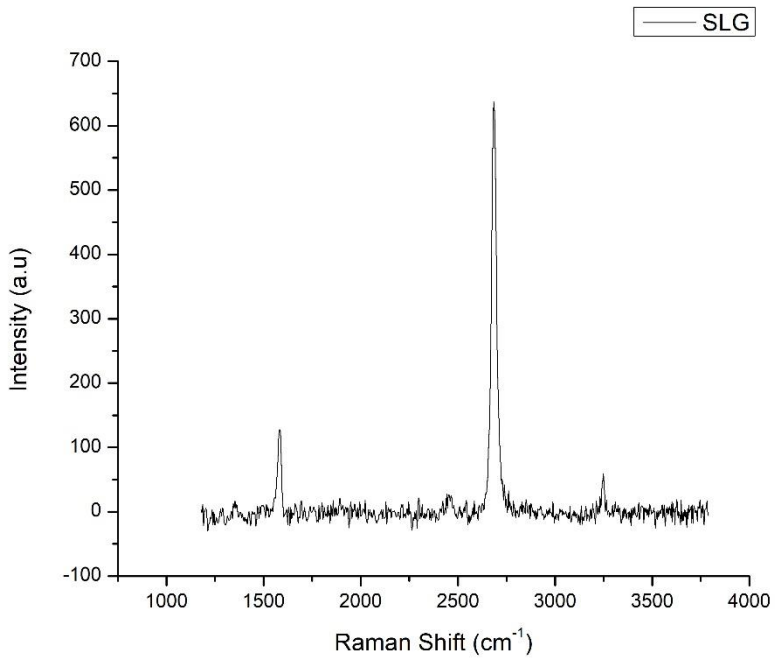

Figure 3.11: Raman Spectrum on as received CVD graphene on SiO_2/Si.

The steps followed to pattern the graphene are identical to those described in section 3.2, in this case the graphene sheet was patterned into arrays of graphene strips. The $Gr/Si/SiO_2$ is immersed into a solution of warm acetone for 10mins and placed on a hot plate at the temperature of 50 C. The sample is then placed in a beaker of IPA for 5 mins to rinse off any acetone residues and then dried with a blast from a N_2 gun to remove the IPA. The sample is then transferred to a hot plate kept at 80C to remove any remaining IPA. A 2-layer resist is used in order to pattern arrays of micron-scale ribbons of graphene. As illustrated in fig. 3.12, a composite resist structure is created with a positive resist (PMMA) as the base layer. This layer acts as the sacrificial layer.

PMMA 950K A4 (4% in anisole) solution is dropped on the surface of the $Gr/SiO_2/Si$ substrate and the spinner is run to 4000rpm for 1 min (10 sec to ramp up, 5 sec to ramp down and 45 sec of constant speed) to form a resist layer of about 200nm thickness. The substrate is transferred onto a hot plate at 180C. The substrate is baked for 5mins and it is then ready for the second layer of resist to be spun.

A HSQ 2% solution in MIBK is pipetted onto the $PMMA/Gr/SiO_2/Si$ substrate placed in the spin coater. The spinner is set to run to 3000rpm for 1min (10sec ramp up, 5 sec ramp down and 45 sec constant speed). This produces a very thin resist layer of around 400Å. The substrate is transferred from the spin coater onto a hot plate at 220 C and baked for 5 mins before it can be exposed to EBL.

Electron beam lithography is used to write a pattern of arrays of graphene strips. When the top layer of HSQ is exposed to the electron beam, it gets cross linked and acts as a protective layer. When the sample is developed after patterning by the EBL machine, all the areas of HSQ surface that were not exposed to the electron beam get dissolved. This leaves areas of cross linked HSQ under which the PMMA and graphene layers sit and areas where the surface is now only covered by the first resist layer (PMMA).

Once the sample is removed from the EBL machine, it is transferred into a beaker containing 30ml of MicroPosit CD-26 developer. The sample is left in the beaker undisturbed for 4mins, after which it is retrieved and placed in a beaker of ultra-pure de-ionised water and rinsed to remove CD-26 and HSQ residues. This step is repeated thrice to ensure that all the residues have been removed and the sample is dried with a N_2 gun and placed on a hot plate at 100C for 2 mins to remove any residual moisture. The sample is then placed in the RIE chamber. At a pressure of 80mT, an O_2 flow of 10sccm with the RF power set to 20W generates an O_2 plasma in the chamber which runs for 4mins and the exposed PMMA/Gr layer is etched away leaving a pristine SiO_2/Si substrate underneath.

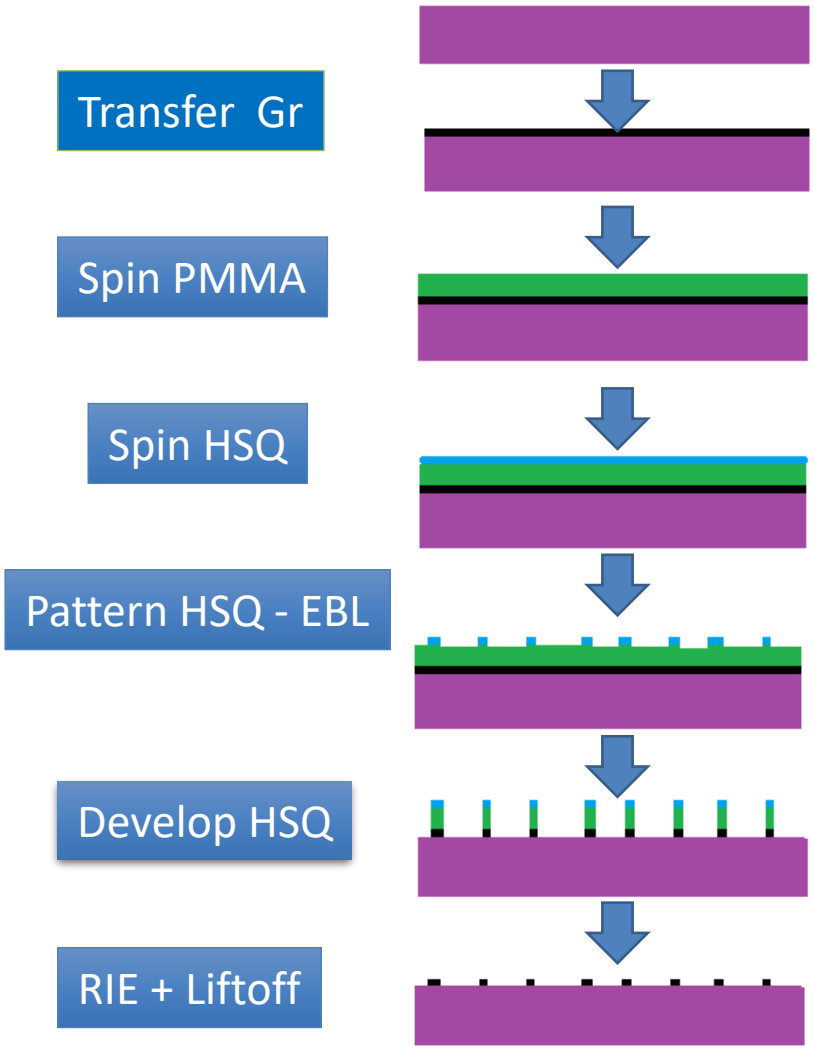

Figure 3.12: A schematic diagram showing the various steps involved in fabricating the graphene strips.

The final step to make the graphene array is to remove the HSQ/PMMA layers that are sitting on top of the patterned graphene. This is achieved through lift-off, where the resist layer (PMMA) is immersed in warm acetone in a beaker and placed on a hot plate at 60C for 2 hrs. The PMMA layer slowly dissolves in the acetone, thus removing the HSQ layer on top along with it. After 2 hrs, the substrate is gently rinsed in IPA and dried off with a N_2 gun with special care being taken as the graphene strips are now sitting on the SiO_2/Si substrate with no other support. Figure 3.13 shows 4 microscopy images taken during various stages of the wet processing.

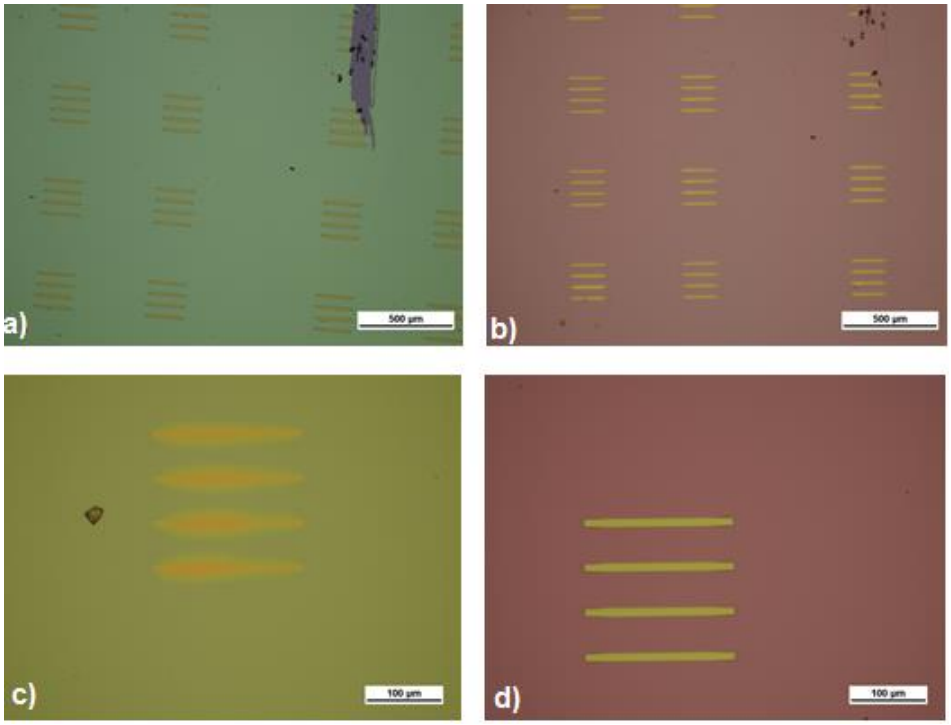

Figure 3.13: Optical microscopy images showing the graphene strips during processing, a) and c) are taken immediately after exposure to the EBL at 5x and 50x magnification respectively and b) and d) are images taken after RIE once the PMMA layer is removed at 5x and 50x magnification respectively.

3.4.3 Contacting the patterned Graphene: Second lithography step and Metallization

Once the graphene strips are patterned, they need to be contacted. This step requires a second iteration of lithography. When the design for the graphene strips is drawn into the CAD file, a second layer representing the contacts is drawn as well and is superimposed on top. The second step of lithography is used to create trenches in a resist layer after the development, and these trenches are filled by evaporating a metal such as Au that will allow the graphene ribbons to be electrically contacted. This requires a repeat of the steps described above in Section 3.3.2, namely spin coating a positive resist layer, which is followed by electron beam lithography, developing the substrate, thermal evaporation of Cr/Au and finally, lift-off. Figure 3.14 shows optical images of the substrate after the contacts are drawn and deposited.

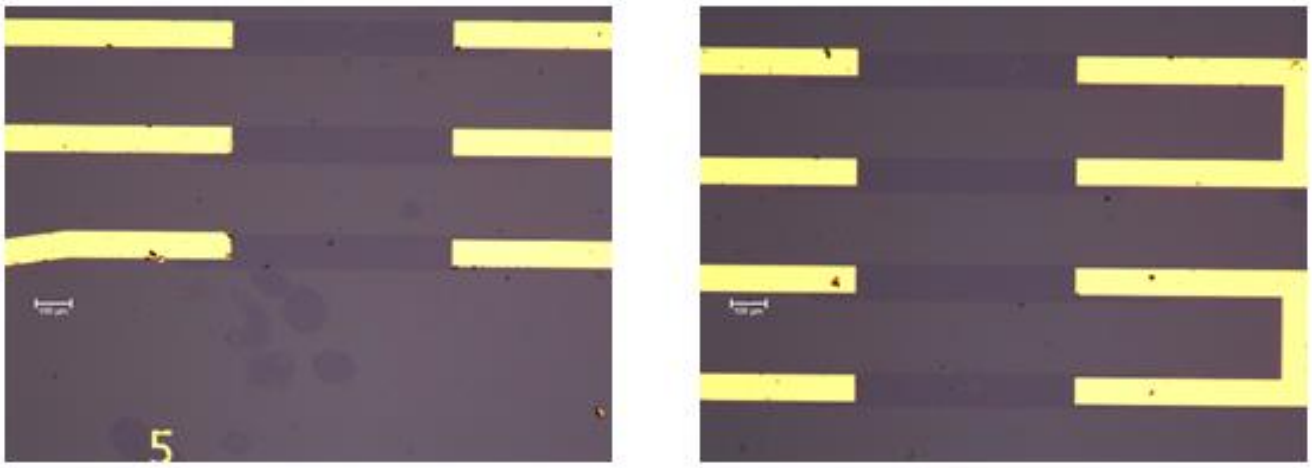

Figure 3.14: Optical images at 5x magnification of two arrays of graphene ribbons after being contacted. The scale bar in both images indicates 100μm.

3.4.4 Embedding Microfluidic Channels on the over the substrate: Third Lithography step.

The final stage of fabrication of the device involves the embedding a microfluidic channel over the graphene strips. The design for this device was finalised after trying 5-6 other prototypes and several options for how to create a flow channel. The criteria and the design are discussed in more detail in Chapter 6.

Here we focus on the fabrication of the design as it was finalised for experimental use. Fig. 3.15 depicts the design of the device using a CAD drawing. Here we see that micron-scale trenches are cut using an electron beam into a thick resist layer. The resultant effect is the height of the trenches are 2 microns, the width of the trenches varies between 5 and 50 microns.

The first stage of fabrication required spin-coating an extra thick layer of resist. Several methods and recipes were tried, and the results were analysed after the lithography step to identify which would yield a consistent height and edge profile.

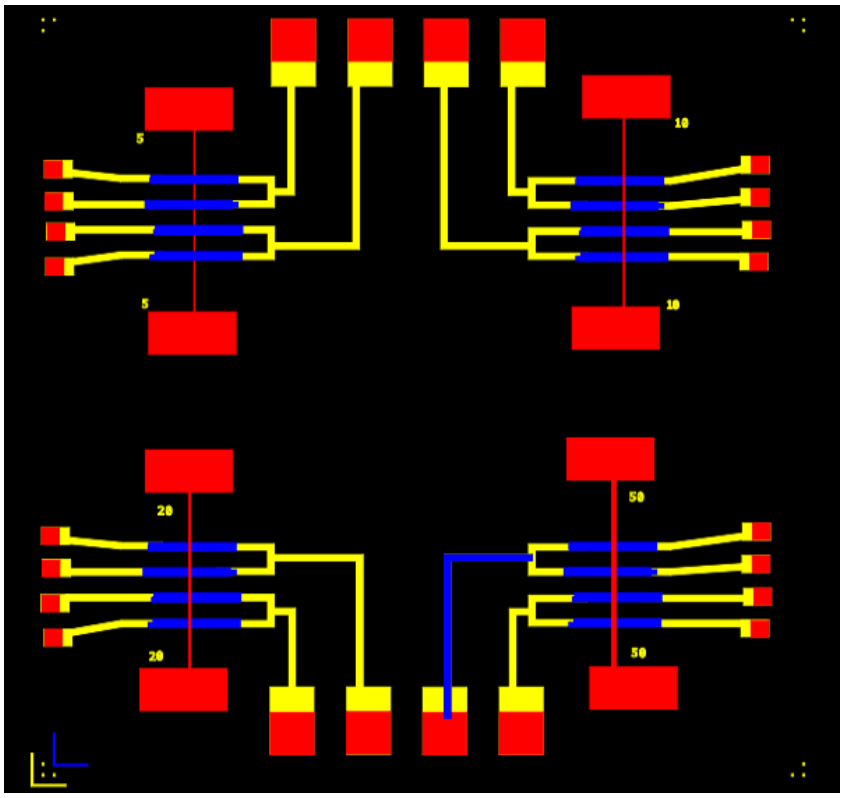

Figure 3.15 shows a schematic of typical device once it is full fabricated. The Blue strips represent the graphene ribbons. The yellow represents the metallised contacts. And the red represents the fluidic channels and trenches.

It was found that using PMMA 950K A11 (11% in anisole) and when the spinner is run to 4000rpm for 1 min (10 sec to ramp up, 5 secs to ramp down and 45 sec of constant speed), a resist layer of about 2000nm (or 2microns) is formed. The substrate is then baked at 180C for 10 mins to allow it to cure properly and then put in the EBL machine to write the pattern of the flow channels.

To identify the right recipe, and because of the unusual thickness of the resist, several dose tests were performed to verify the best parameters for the EBL. Figure 3.16 and Figure 3.17 show a microscope image and an SEM image respectively of test channels that were created in 2 micron thick resist after the correct dose was identified. It shows that the channel has linear profile and uniform width.

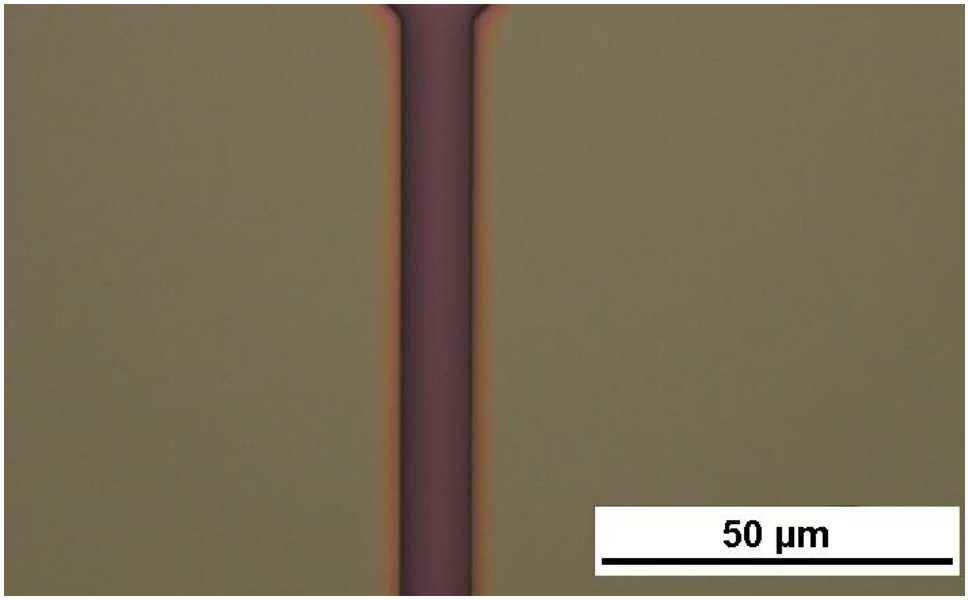

Figure 3.16: An optical image taken at 50x magnification of a test channel that is 5µm wide.

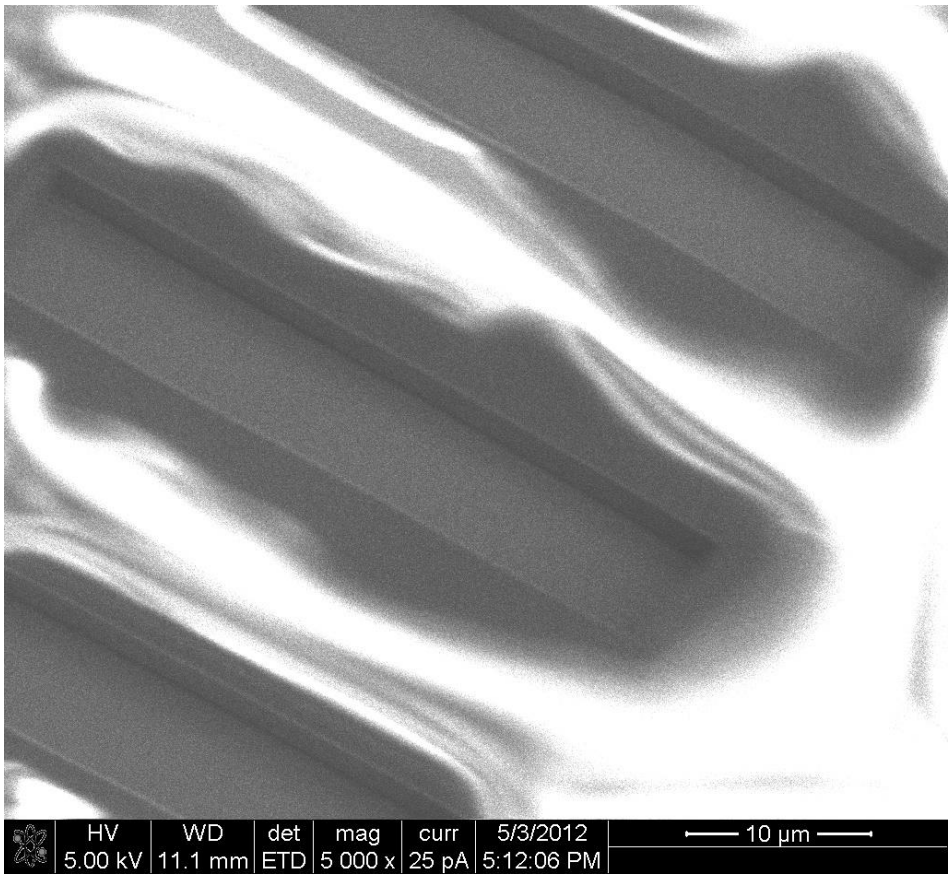

Figure 3.17: An SEM image taken at 5000x magnification of a test channel showing the profile of the resist that is 10µm wide and 2µm deep.

Once the lithography was completed, the sample needed development. The recipe for the developer solution was the same as describe in section 3.3.3 (15 parts IPA ,5 parts of MIBK and 1 part of EMK) however because of the thickness of the resist, the amount of time the substance was immersed in the solution was 45 seconds. After checking for the trenches were completely developed, the sample is then ready to be put in a chip carrier and bonded. Figure 3.15 shows optical microscopy images of varying thicknesses of the flow channels and the thick resist layer that sits on top of the substrate. Here, the graphene strips and contacts are visible through the layer of resist.

Figure 3.18: Optical images at 5x magnification showing flow channels of 3 different widths. Top left - 5µm, Top right- 20µm and Bottom left - 50µm. For all three images, the scale bar indicates 100µm

The final stage of fabrication of a measurable device is mounting and bonding the sample. In order to study the electrical response of the graphene strips to any molecules that it's surface comes into contact with, it is important that electrical connections are made from the metallic contacts that are fabricated on the chip to the real-world electronics equipment that allow us to provide electrical inputs and monitor electrical responses. The sample is mounted on a commercially procured 44-pin chip carrier package which is able to hold a 1cmx1cm chip. The sample mounting and bonding are performed as described in detail in section 3.3.4

3.5 Summary of Devices Fabricated

A complete list of all the devices, fabricated towards this work and used in experiments (discussed in chapters 4-6) is listed in the table below.

Sample	Graphene Source	Substrate	Device Type	Device Yield	Purpose of Device
EG1	CVD Gr /Cu foils from GrSu	Glass	2 cm^2 graphene on glass	80%	Electrochemical characterisation of graphene
EG2	CVD Gr /Cu foils from GrSu	Glass	2 cm^2 graphene on glass	80%	Electrochemical characterisation of graphene
EG3	CVD Gr /Cu foils from GrSu	Glass	2 cm^2 graphene on glass	80%	Electrochemical characterisation of graphene
EG4	CVD Gr /Cu foils rom GrSu	Glass	2 cm^2 graphene on glass	80%	Electrochemical characterisation of graphene

Sample	Graphene Source	Substrate	Device Type	Device Yield	Purpose of Device
EC1	CVD Gr /Cu foils from GrSu	Glass	1cm^2 graphene on glass	80%	Electrochromic experiments with graphene
EC2	CVD Gr /Cu foils from GrSu	Glass	1cm^2 graphene on glass	80%	Electrochromic experiments with graphene
EC3	CVD Gr /Cu foils from GrSu	Glass	1cm^2 graphene on glass	80%	Electrochromic experiments with graphene
EC4	CVD Gr /Cu foils from GrSu	Glass	1cm^2 graphene on glass	80%	Electrochromic experiments with graphene

TS1	CVD Gr /Cu foils from GrSu	Glass	1cm^2 graphene on glass	50%	Control experiments for sensing PCT
TS2	CVD Gr /Cu foils from GrSu	Glass	1cm^2 graphene on glass	50%	Control experiments for sensing PCT
TS3	CVD Gr /Cu foils from GrSu	Glass	1cm^2 graphene on glass	50%	Control experiments for sensing PCT
S1	CVD Gr on SiO_2 from GrSu	SiO_2/Si	Large-area 'hall-bar'	50%	Functionalising graphene and detection of PCT
S2	CVD Gr on SiO_2 from GrSu	SiO_2/Si	Large-area 'hall-bar'	50%	Functionalising graphene and detection of PCT

Sample	**Graphene Source**	**Substrate**	**Device Type**	**Device Yield**	**Purpose of Device**
S3	CVD Gr on SiO_2 from GrSu	SiO_2/Si	Large-area 'hall-bar'	50%	Functionalising graphene and detection of PCT
S4	CVD Gr on SiO_2 from GrSu	SiO_2/Si	Large-area 'hall-bar'	50%	Functionalising graphene and detection of PCt
S1	CVD Gr on SiO_2 from GrSu	SiO_2/Si	Gr-FET arrays	30%	Studying the effect of water on graphene through MF channels
S2	CVD Gr on SiO_2 from GrSu	SiO_2/Si	Gr-FET arrays	30%	Studying the effect of water on graphene through MF channels

Table 3.1: List of all the devices fabricated for use in experiments along with their purpose of use, yield, graphene source and device type.

3.5 Bibliography

1. A. K. Geim & K. S. Novoselov Nature Materials 6, 183 - 191 (2007)
2. A. Reina, X. Jia, J. Ho, D. Nezich, H. Son, V. Bulovic, M. S. Dresselhaus, and J. Kong 2009. Nano Letters, 9(1):30, 2009.
3. X. Li, W. Cai, J. An, S. Kim, J. Nah, D. Yang, R. Piner, A. Velamakanni, I. Jung, E. Tutuc, S. K. Banerjee, L. Colombo, and R. S. Ruoff Science, 324(5932):1312, 2009.
4. Kim, K. S., Zhao, Y. Jang, H. Lee, S. Y. Kim, J. M. , Kim, K.S., Ahn, J. H., Kim, P.; Choi, J. Y.; Hong, B. H. Nature 2009, 457, 706-710.
5. Henrique Guimaraes Rosa, José Carlos Viana Gomes and Eunézio A Thoroh de Souza 2D Materials 2015, Volume 2, Number 3
6. Shao, Y. Y., Wang, J., Wu, H., Liu, J., Aksay, I. A., Lin, Y. H. Electroanalysis 2010, 22, 1027–1036
7. Alwarappan, S., Erdem, A., Liu, C., Li, C. Z. J. Phys. Chem. C 2009, 113, 8853–8857
8. Wan Li,Cen Tan,Michael A. Lowe,Hector D. Abruna, D. C. Ralph. ACS Nano 2011, Vol.5, No.3, 2264-2270
9. Dresselhaus, M.S.; Dresselhaus, G.;. Adv. Phys. 2002, 51, 181–186.
10. Kolmakov, A., Moskovits M., Annu. Rev. Mater. Res. 2004, 34, 151–180.

Chapter 4

Electrochemistry of Graphene

4.1 Introduction

Beginning with its theoretical study as early as in the 1940s, and only intensified by its experimental discovery in 2004, graphene as a material has captured great amount of interest for its novel properties [1][[2]. The study of graphene and its electrochemical properties is a burgeoning area of research towards its use in applications such as a bio-sensing, electrocatalysis and for energy storage.[3]

Electrochemistry is an interfacial technique and is used to gain an understanding of the surface of a material by studying processes that dominate at solid-liquid interface. [5] It is a useful tool because it is very sensitive to interactions between the surface and environment. Electrochemical techniques can be employed for specific detection of analytes, as well as being a low-cost technique for characterisation of materials. Graphene being a material with exceptionally high electrical performance including high electron mobility, the possibility for large-surface-area devices, and a high degree of transparency to visible light, lends itself as a very suitable choice for its use as an electrochemical transparent electrode material.[4][5] Furthermore, as the research on

functionalisation of graphene progresses, more potential emerges for use of graphene with specific, designed properties that can be utilized towards an array of applications.

This chapter begins with an overview of graphene as an electrochemical electrode. This followed by introducing some fundamental electrochemical concepts that are required to discuss electrochemical experiments in section 4.2. Subsequently, a description of the two electrochemical methods that are primarily used in the experiments, namely Cyclic Voltammetry and Chrono-Amperometry are detailed in section 4.3. And finally, section 4.4 describes the results of experiments performed on electrochemical characterization of graphene electrodes using Cyclic Voltammetry and a demonstration of the reversible electrochromic measurements performed graphene-on-glass electrodes.

4.2 Electrochemical Concepts

Electrochemical redox reactions occur at the interface of an electrode and an ionic conductor in solution, known as the electrolyte. Such reactions take place as a result of the transfer of electrons between the electrode and the electrolyte species where both species undergo a change in their oxidation state. [5][6] This typically happens as a result of the application of an external voltage where one species (atom/molecule/ion) suffers the loss of electron(s) and gets oxidized, which is then absorbed at the electrode-electrolyte interface by other species which then is said to be reduced. The charge transfer process is a complex one, and several factors can affect it, including the electrochemical properties of the electrode surface, defects on the electrode surface, surface roughness, the properties of the electrolyte solution, the diffusion rate through the solution, electrode geometry and the presence of impurities which may restrict the total in-contact area of the electrode and electrolyte species [6][7]. To begin to explain

these factors, a simple electrochemical cell is described in Section 4.2.1 which will be used as the basis to understand the various aspects of electrochemical redox reactions.

4.2.1 A standard Electrochemical Cell

A standard electrochemical cell used for voltammetry experiments (as will be further described in section 4.2.2) in the electrochemical study of graphene consists of three electrodes: The reference electrode (RE), the working electrode (WE) and the counter electrode (CE). All three electrodes are immersed into a conducting ionic solution known as the electrolyte. In this set-up, a potential is applied across the WE and the CE. This potential facilitates the charge transfer between the WE and the electrolyte solution. The set up as pictured in figure 4.1 can be thought of as two half-cells. The first half cell is between the working electrode and the reference electrode, which consists typically of a material with a well-known reduction potential. The reference electrode serves as the reference to measure the potential of the working electrode and is not involved in the current flow of the circuit. The second half-cell of the set-up consists of the counter electrode which serves to complete the circuit by allowing a charge transfer to take place through at redox reaction at its interface with the electrolyte. However, it should be noted that typically, a counter electrode is shown such that it is much larger in size compared to the working electrode. This means that the processes and interactions that determine the current flowing through the circuit will be directly limited by the reaction at the working electrode interface, thus giving a way to probe and evaluate the rate of the reaction at the working electrode.

4.2.2 Current – Overpotential Relation and Butler-Volmer Equation.

For the given model cell as illustrated in Figure 4.1, the redox reaction that takes place at the working electrode can be represented by a simple reaction

$$O + e^- \underset{k_O}{\overset{k_R}{\rightleftharpoons}} R \qquad [4.1]$$

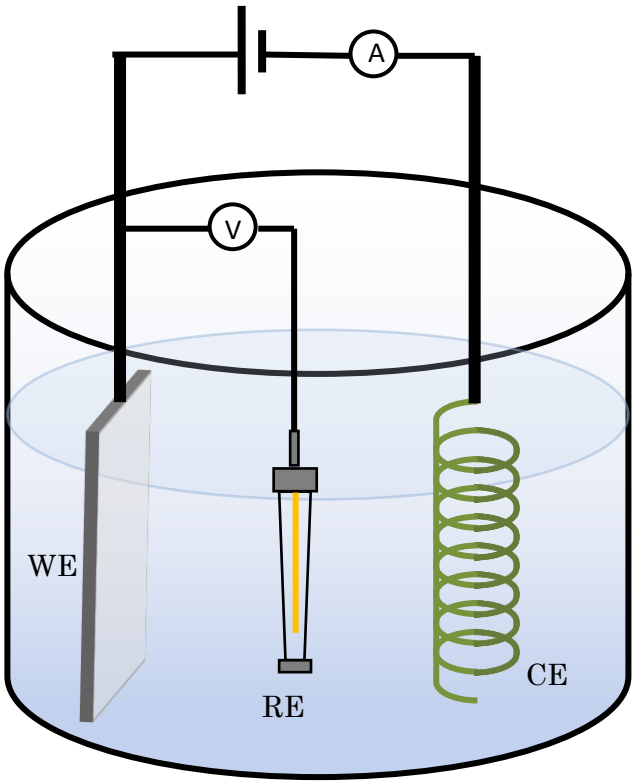

Figure 4.1: A schematic diagram showing the three-electrode electrochemical cell.

where O is the oxidized species, which accepts an electron e^- to be converted into R, the reduced species. The rate of the forward reduction reaction is given by rate constant k_R and the rate of the oxidation reaction is represented through a rate constant k_O .

For reversible redox reaction such as this, the equilibrium state of the reaction can be described by the Nernst equation which relates the equilibrium potential of the electrode to the concentration of the reactants as well as the product, as given by the equation,

$$E_{eq} = E^{o\prime} + \frac{RT}{nF} ln \frac{C_O^{\infty}}{C_R^{\infty}} \qquad [4.2]$$

where $E^{o\prime}$ is the formal potential for the redox couple, R is the gas constant, T is the temperature, F is Faraday's constant, n is the number of electrons exchanged in the reaction and C_R and C_0 denote the bulk concentrations of the oxidation and reduction species.

When a current is passed through the electrochemical cell, a reaction at the electrode surface takes place. However, since the reaction cannot be perfectly reversible, there exists always a deficit of potential that must sustain the current in a way that the actual electrode potential differs from the equilibrium potential by a factor η which is referred to as the overpotential.

The total current that passes from the electrolyte to the working electrode can be derived by finding the difference of the anodic current i_a and the cathodic current i_c , which are given by the equations:

$$i_a = nFAk_O C_O(0,t)$$

and [4.3]

$$i_c = nFAk_R C_R(0,t)$$

where $C_O(0,t)$ and $C_R(0,t)$ refer to the concentrations of the oxidation and reduction species at the interface of the electrolyte and working electrode at a given time t, such that 'x' the distance from the electrode interface is zero. F denotes the Faraday constant, and A refers to the surface area of the working electrode.

The total current therefore, is given by

$$i = i_a - i_c = nFA\,[k_O C_O(0,t) - k_R C_R(0,t)] \qquad [4.4]$$

where the rate constants for the reactions are given by the Arrhenius theory

$$k = k^0 e^{\frac{-E_a}{RT}} \qquad [4.5]$$

where E_a is the activation energy – the energy barrier that has to be surmounted for the reaction to occur, R is the gas constant and T is the temperature. The activation energy ca be written as a linear function of the overpotential η, defined as the difference between the applied potential (potentials are measured between working and reference electrodes) and the zero-current potential, $E_{eq.}$

If we assume that oxidation and reduction rates are equal at equal concentrations, then we can see that

$$E_{eq} = E^{0\prime} \qquad [4.6]$$

and consequently, we can also write $k_R = k_O = k^0$, which is referred to as the standard rate constant and relates to the intrinsic kinetic facility of the electrode reaction. In effect this means that the larger the value of k^0 the quicker the system will achieve equilibrium and consequently, high values also yield a large current for a small overpotential.

In such a case, the expressions for the oxidation and reduction rate constants can be written in terms of

$$k_{ox} = k^0 e^{\left[\frac{(1-\alpha)nF}{RT}(E-E^{0\prime})\right]}$$

and [4.7]

$$k_{red} = k^0 e^{\left[\frac{-\alpha nF}{RT}(E-E^{0\prime})\right]}$$

where, α is the transfer coefficient, and refers to the fraction of the total energy change by which the activation energy is reduced at the electrode-electrolyte interface when an overpotential η is applied. For the oxidation reaction this becomes a factor of 1-α

As a result, the total current can now be re-written to include the above rate equation and gives the generalized relation for the current on an electrode,

$$i = i_O \left[\frac{C_R(0,t)}{C_R^{\infty}} e^{\left[\frac{(1-\alpha)nF}{RT}\eta\right]} - \frac{C_O(0,t)}{C_O^{\infty}} e^{\left[\frac{-\alpha nF}{RT}\eta\right]} \right] \qquad [4.8]$$

where the current i_O is referred to as the exchange current, and given by the equation:

$$i_O = nFAk^0 (C_O^{\infty})^{(1-\alpha)} (C_R^{\infty})^{\alpha} \qquad [4.9]$$

Such that, at equilibrium $i_O = i_c = i_a$.

The Butler-Volmer equation is an approximation of equation 4.8. It describes the relationship between the current on an electrode and the electrode potential if there are both anodic and cathodic reactions occurring on the same electrode when there are limiting factors on the kinetics of the reaction or on the diffusion of species from electrolyte to interface.

In this situation, equation 4.8 reduces to

$$i = i_O \left[e^{\left[\frac{(1-\alpha)nF}{RT}\eta\right]} - e^{\left[\frac{-\alpha nF}{RT}\eta\right]} \right] \qquad [4.10]$$

This means that for high values of applied overpotential, the current is dominated by one particular current, either anodic or cathodic depending on whether the value of the overpotential applied is positive or negative. Furthermore, as is evident in equation 4.10, the exchange current is a function of the standard rate

constant of the redox couple and indicates the rate of response of the system to achieve a particular current without having to apply a large overpotential. This means that application of a very small potential on top of the equilibrium potential will result in a high current, for systems which have a large exchange current value. For those that have small values of exchange current, the kinetics of the system are very sluggish and large values of overpotential need to be applied. Notably, for large overpotentials, the rate of charge transfer is dominated by mass transfer and diffusion limits to the electrode. Both of these effects can clearly be observed by looking at the graph of the total current as a function of the applied overpotential in Figure 4.2.

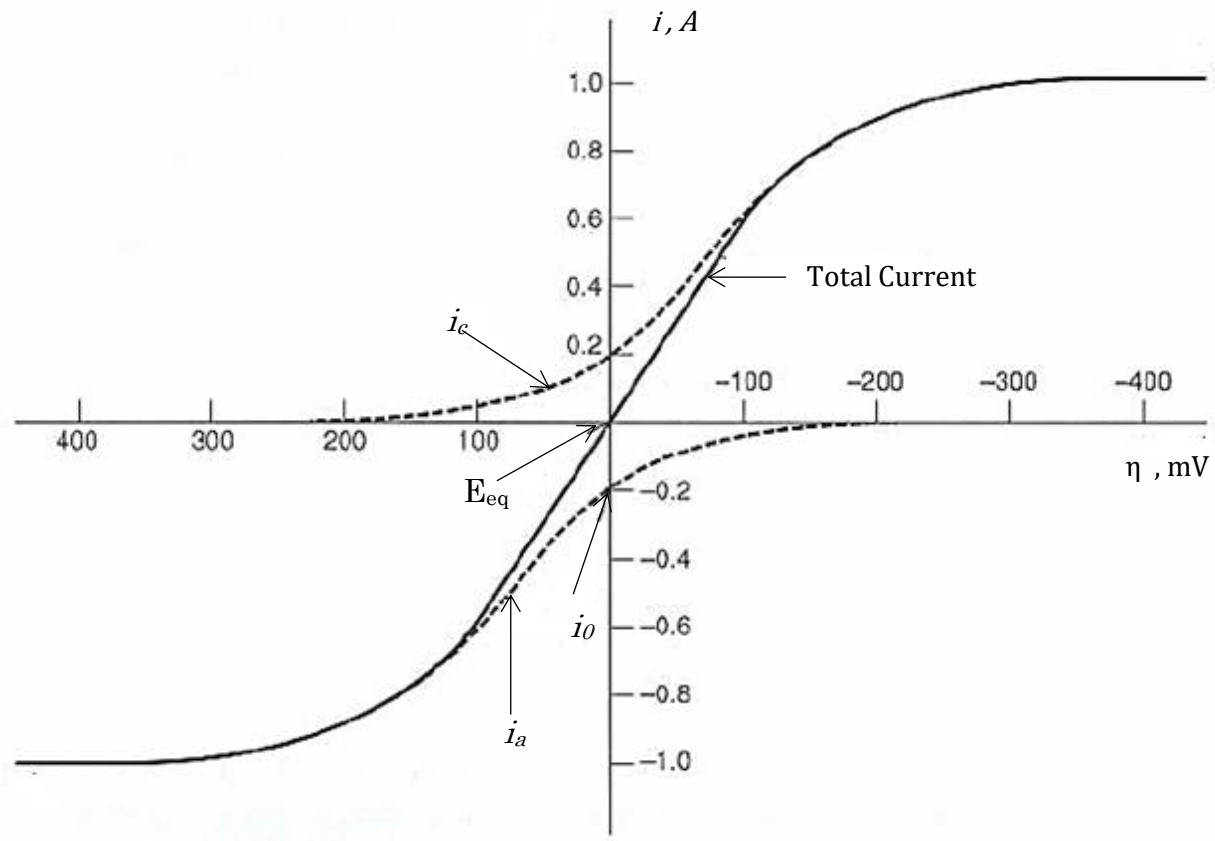

Figure 4.2: Total current as a function of applied potential at the electrode-electrolyte interface, as the sum of cathodic and anodic partial currents. The total current is represented as a solid line and the partial currents as dashed lines for a value of $\boldsymbol{\alpha = 0.5}$ Adapted from [6]

4.2.3 Mass Transfer and Diffusion limitations

Mass transfer refers to the movement of material through a solution as a result of a electrical or chemical potential difference. For the simplest electrode reactions, the kinetics of electron transfer and chemical reactions are extremely rapid in comparison to mass transfer mechanisms. Typically, this means that the reactions quickly attain equilibrium and the electrode potential for these can be described by the Nernst equation. For such reactions, the limiting factor on the reaction is determined by the rate at which the electroactive species are brought to the surface of the electrodes by mass transfer. Mass transfer can take place as a result of migration, which is the movement of a charged species under the influence of electric fields in solution. Diffusion refers to the movement of species under the influence of a chemical potential gradient or concentration gradient and convection, which refers to transport as a result of stirring or any kind of flow gradients. Altogether, mass transport can be described by the Nernst-Planck equation for one-dimensional mass transfer.

$$J_i(x) = -D_i \frac{\partial C_i(x)}{\partial x} - \frac{z_i F}{RT} D_i C_i \frac{\partial \phi(x)}{\partial x} + C_i \vartheta(x) \qquad [4.11]$$

where, $J_i(x)$ is the flux for a species i at a distance x from the surface, D_i is the diffusion coefficient and $\frac{\partial C_i(x)}{\partial x}$ refers to the concentration gradient at a distance x, and $\frac{\partial \phi(x)}{\partial x}$ is the potential gradient and z_i and C_i are the charge and concentration for the given species i respectively.

For a voltammetric cell set-up as described in section 4.2.1, mass transport is primarily limited by diffusion processes, and contributions from migration and convection are negligible. This means that the Nernst-Planck equation reduces to contribution from just the diffusion term. If we consider a reaction as in equation 4.1, where a species O accepts an electron, to become R. Then, as the reaction at the electrode surface progresses, the species O is gradually consumed resulting in a depletion of the concentration of O around the vicinity of the electrode surface. This depletion layer causes a concentration gradient to form,

such that for any further progress of the reaction, the species O must diffuse from regions of higher concentration towards the electrode surface. Such a diffusion process is governed by Fick's first and second laws of Diffusion and the contribution to current density can be determined solving for them,

namely,

$$J_{\mathrm{O}}(x,t) = -D_{\mathrm{O}} \frac{\partial C_{\mathrm{O}}(x,t)}{\partial x} \qquad [4.12]$$

and

$$\frac{\partial C_{\mathrm{O}}(x,t)}{\partial t} = D_{\mathrm{O}} \frac{\partial^2 C_{\mathrm{O}}(x,t)}{\partial x^2} \qquad [4.13]$$

where, $C(x,t)$ represents the concentration profile and $i(t)$ denotes the diffusion limited current and $J_{\mathrm{O}}(x,t)$ and $C_{\mathrm{O}}(x,t)$ are respectively the flux and concentration of oxidized species at position x and time t, and D_{O} is the diffusion coefficient of the oxidised species.

For a given reaction as in equation 4.1, the number of electrons that are transferred between the electrode and electrolyte has to be proportional to the number of the O species that is diffusing the the surface of the electrode per unit time. For such a system, the relation between the current and the concentration profile for the species O can be derived so as to give the equation,

$$\frac{i}{nFA} = -D_{\mathrm{O}} \left[\frac{\partial C_{\mathrm{O}}(x,t)}{\partial x}\right]_{x=0} = D_{\mathrm{R}} \left[\frac{\partial C_{\mathrm{R}}(x,t)}{\partial x}\right]_{x=0} \qquad [4.14]$$

This means that the current at the electrode surface is directly proportional to the slope of the concentration profile at the surface of the electrode. This relation is used in typical voltammetry experiments (as described in section 4.3) where the potential of the electrode is driven to higher values and the corresponding current is measured. Figure 4.3 (b) illustrates the relationship between the current-voltage curves along with a corresponding change in the concentration profile (a). In figure 4.3(b) as the larger positive potential is applied, it drives the system away

from its equilibrium potential causing the oxidation reaction to become dominant. Consequently, a depletion of the reduction species begins to occur, setting up a concentration gradient and increases the value of the slope in equation 4.14. This leads to an increase in the current which has a maximum when the surface of the electrode is depleted of the reduced species R. As the depletion region extends beyond the vicinity of the surface, the slope of the concentration profile begins to decrease and correspondingly the current also decreases. The height of the maximum of the current curve is proportional to the bulk concentration of the reduced species R and is known as an oxidation peak. Similarly, the converse happens on the application of a negative potential and a reduction peak occurs.

For systems with slower kinetics, more the oxidation and reduction peaks occur further away from the equilibrium potential than for systems with faster kinetics because it requires more energy to be supplied to the system, in order to see the same peak current response. This feature effectively means that by studying the current-potential curves of the redox couple, information about the nature of the electrode, the concentration of the bulk species as well as an insight into the kinetics of the system.

Finally, the diffusion rate of the bulk species is dependent on the rate of change of potential that is applied to the electrode. In measurement terms, this corresponds to the sweep rate for the voltage applied to the system. This is because, the faster the potential changes, the shorter is the time for the concentration gradient to extend into electrolyte away from the electrode surface. This corresponds to the height of the oxidation/reduction peak as it is proportional to the concentration of the bulk species. This is illustrated in Figure 4.4. where the left graph shows the concentration profiles as a function of distance from the electrode and the right graph represents corresponding current-potential curves taken at the working electrode for three different sweep rates. Here, as the sweep rate is increased from 1 to 2, we can see the height of the peak increases and the slope of the concentration profile becomes steeper. However, beyond a point the kinetics are limited and a much larger potential is required to reach the current peak.

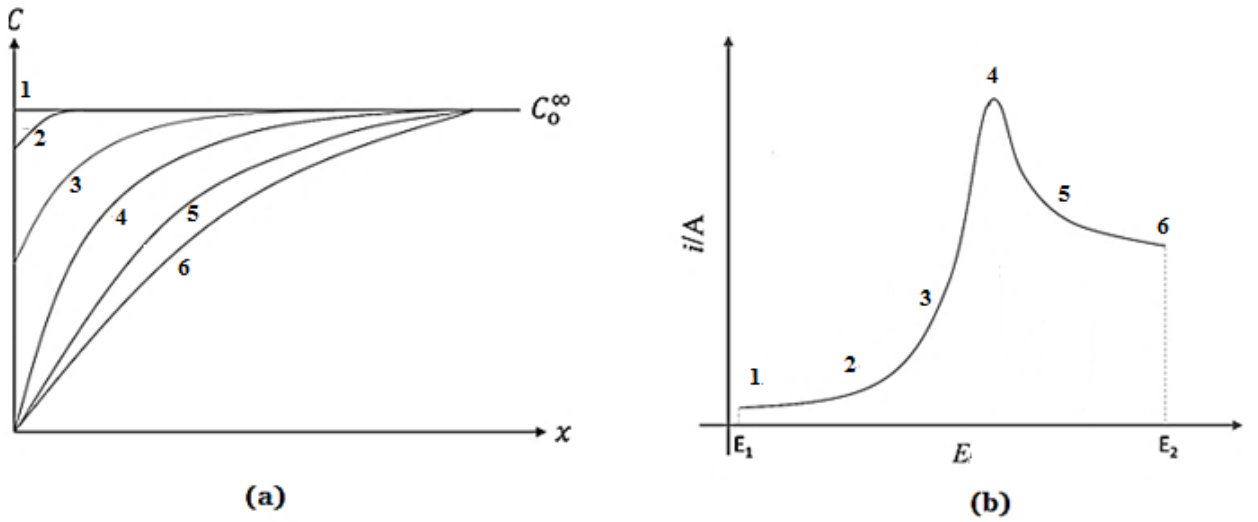

Figure 4.3: Graphs showing (a) Time-dependent concentration profiles of the oxidized species for a redox couple. The numbers 1 to 6 correspond to increasing time and so increasingly negative values of E (b) Current-potential profile of a redox couple when the potential at the working electrode is varied linearly from E_1 to E_2 as a function of time. Adapted from [5][6]

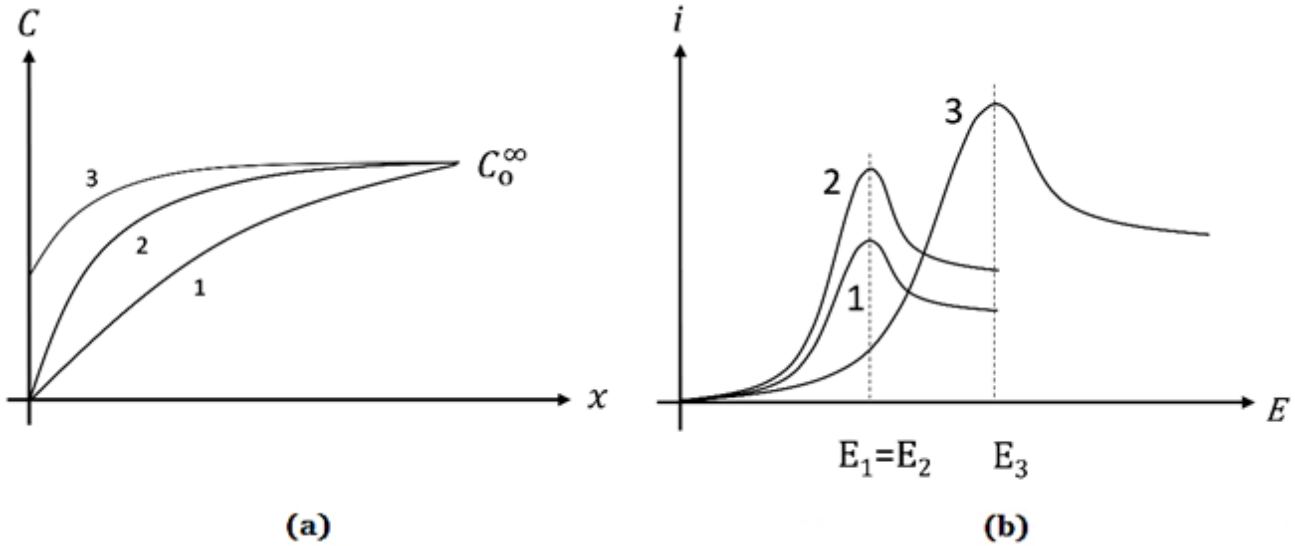

Figure 4.4: Graphs showing (a) Influence of the scan rate v (V s^{-1}) of the potential applied at the working electrode on the concentration profile at the working electrode. The numbers 1, 2 and 3 correspond to increasing scan rates. Right: Influence of scan rate on the reduction current peak height. Adapted from [5][6]

4.3 Electrochemical Methods

Several electrochemical methods are available to study electrode reactions and understand electrode charge transfer processes – amongst them voltammetry and amperometry are the most widely used techniques have been reported to be used in the characterization and development of graphene-based devices in electrochemical based applications. This is due to their simplicity, low-cost and high level of sensitivity that they can achieve. [17] These techniques, belong to a group of potentio-static measurements where an electrode potential is applied and used as the driving force for a redox reaction to occur. The resultant current is then analysed to give information about the nature of the electrode, the nature of the redox reaction, the kinetics of the reaction, and in the case of sensing - the detection of an analyte substance. Below, two methods are enumerated that are used in the experiments section 3.5 and 3.6 – namely, cyclic voltammetry and chrono-amperometry.

4.3.1 Cyclic Voltammetry

Potential sweep methods including cyclic voltammetry are widely used to study electrode processes. They typically entail applying a time-varying potential to the working electrode which results in oxidation/reduction reactions taking place at the electrode-electrolyte interface and then studying the current-potential characteristics of the system. This type of method is used to understand electrode reaction mechanism, identification of species present in the solution and for quantitative analysis of rate reactions [21]. Cyclic voltammetry involves the application of potential to the working electrode. The potential has a triangular wave form with linear ramp rate in cyclical phases. (illustrated in figure 4.5). The potential is applied between the working and the reference electrode and the current is measured between the working and the counter electrode (as illustrated in the schematic Figure 3.1). The current is monitored and plotted against the applied potential. This graph is referred to as a voltammogram.

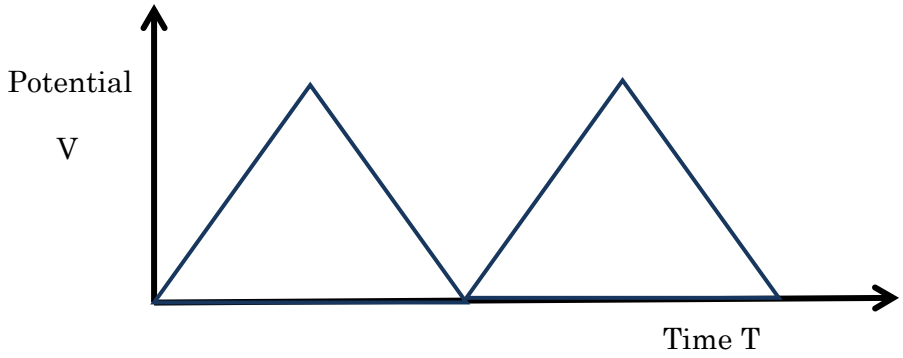

Figure 4.5: A typical Cyclic Voltammetry Potential Waveform

Figure 4.6 illustrates a typical cyclic voltammogram for a reversible redox reaction like equation 4.1. A – where the reaction is electrochemically reversible with very quick electron transfer. And B – where the reaction of the redox couple is not perfectly reversible, which means, considerable overpotentials are required to drive the reaction. Two parameters that are obtained from this graph are the current peak ratio, $\frac{i_p}{i_a}$, and the current peak potential separation, $\Delta E_p = E_c - E_a$. By studying the current response to the potential applied to the electrode, one can understand from the nature of the curve and the extent of reversibility of the redox reaction.

In the case A, of a fully reversible reaction, the reaction is extremely rapid and Nernst equation applies. This means the system very quickly reaches equilibrium and the concencetration of the oxidation and reduction species quickly equilibrate. For such systems, the peak potential separation given as ΔE_p is very small. And ratio of the peak heights is equal to one. The potential at which the peaks occur are also independent of the sweep rate v and the peak current is proportional to $v^{1/2}$. From figure 3.9, it is evident that for irreversible electrochemical reactions, the ΔE_p is much larger and considerable overpotentials are required to drive the reaction. This is also evidenced by the peak height for the forward reaction occurring being at a greater potential. Furthermore, no inverse peak appears on the reversing the scan direction as the current decay continues.

In reversible reactions, the electron transfer rate is always greater than the rate of mass transport and peak potential is independent of the sweep rate. When the system is quasi-reversible mass transport rate effects become comparable to electron transfer rates. This means that peak potentials are affected by the applied sweep rate and increase with increase sweep rates. For irreversible reactions, the mass transfer rates are much larger than electron transfer rates. This can be quantitatively described by the introduction of a parameter ζ as a quantitative measure of reversibility of a reaction which denotes effectively the ratio of kinetics is to transport and defined as

$$\zeta = \frac{k_0}{\sqrt{FD\nu/RT}} \qquad [4.15]$$

Different ranges of the value have been suggested for different processes. For stationary planar electrodes, a process is said reversible if $\zeta \geq 15$, quasireversible if $15 \geq \zeta \geq 10^{-3}$ and irreversible if $\zeta \leq 10^{-3}$. [22]

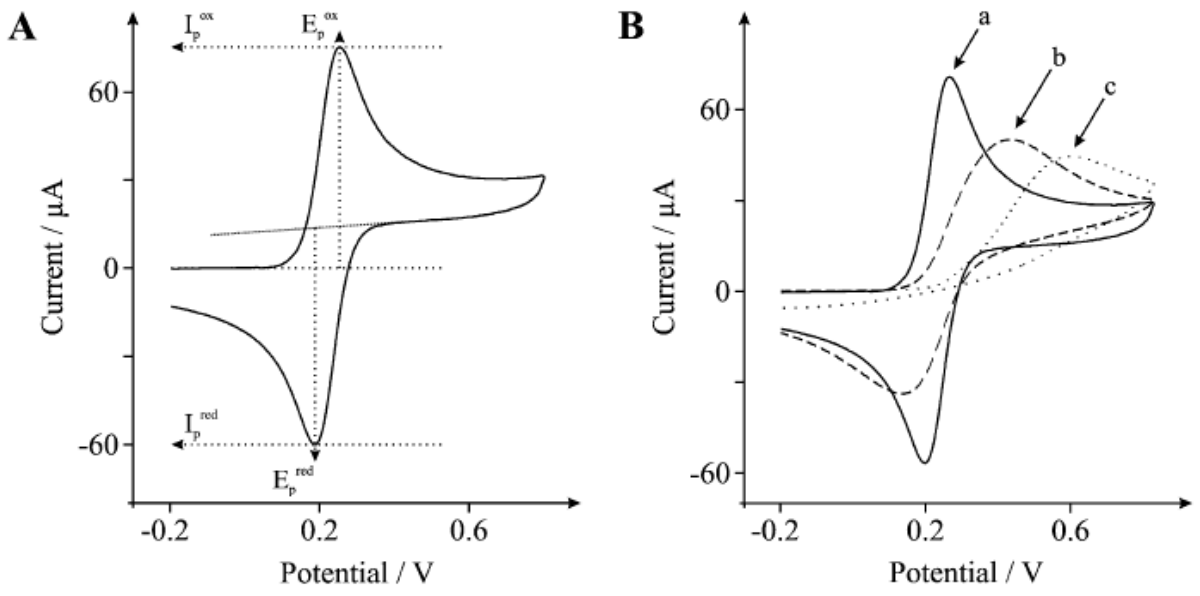

Figure 4.6: Typical cyclic Voltammogram depicting peak position E_p , peak height I_p for (A) reversible reaction (B) Cyclic voltammograms for (a) reversible (b) quasi-reversible and (c) irreversible electrode reactions. Adapted from [22]

For Quasi-reversible reactions, the shape of the I-E curve and the peak separation ΔE_p are dependent on a number of factors. Namely, the transfer coefficient α, the standard rate constant $k^0$and the sweep rate ν. k^0 can be determined from the peak separation within the range 90mV- 250mV by introducing a dimensionless parameter ψ which can be tabulated for varying values of ΔE_p , where it is defined as,

$$\psi = \frac{\left(\frac{D_O}{D_R}\right)^{\alpha} k_0}{\sqrt{\pi a D_O}} \qquad [4.16]$$

where $a = \frac{nF\nu}{RT}$ and D_o and D_R are diffusion coefficients for the oxidation and reduction species, F is the faraday constant, the transfer coefficient is denoted by α , R is the gas constant, T the temperature and the sweep rate is given by ν. This can be further simplied when $D_O \cong D_R$ and α can be neglected which gives

$$\psi = k_0 \frac{1}{\sqrt{\pi \frac{nFD_O}{RT}}} \nu^{-1/2} \qquad [4.17]$$

And this means that the rate constant can be extracted from the slope of the plot of ψ as a function of scan rate.

4.3.2 Chronoamperometry

Chronoamperometry is an electrochemical technique where a step potential is applied to the working electrode and the current response is plotted as a function of time. Chronoamperometry experiments are most commonly either single potential step, in which only the current resulting from the forward step as described above is recorded, or double potential step, in which the potential is returned to a final value (E_f) following a time period, usually designated as τ, at the step potential (E_s). In both cases, when a step potential is applied to the electrode surface, two main processes occur. First, a Faradaic current response is observed as a result of the electron transfer due to the electrochemical reactions at the electrode surface. Secondly, a capacitive current is also caused as a result of the charging at the electrode surface due to potential variation. Such a

capacitive current does not reflect any charge transfer and only causes build-up of charge on the surface of the electrode and in the surrounding electrolyte solution. Typically, under potentiostatic conditions, this charging process is extremely quick and any capacitive current will decay in a very short time (order of milliseconds) and can be neglected for measurements having longer time-scales. The Faradaic current contribution in chronoamperometry can be described by an equation known as the Cottrell equation. This equation describes the observed current for a planar electrode at any time following a large forward potential step in a reversible redox reaction (or to large overpotential) as a function of $t^{-1/2}$.

$$I(t) = \frac{nFAD^{1/2}C_{\infty}}{(\pi t)^{1/2}} \qquad [4.18]$$

where n = number of electrons transferred in the reaction; F is the Faraday's constant, A is the electrode area (cm^2), C_{∞} is the bulk concentration of electroactive species (mol/cm^3), and D_0 is the diffusion constant for electroactive species (cm^2/s).

Here, as used in the case of the electrochromic experiments described in section 4.4, a double potential step chronoamperometry technique is explained. In this technique, a step potential is applied alternatingly between two values. As shown in figure 4.7, a forward potential is applied from E_i to E_s and held for a duration τ , enabling the forward reaction. The potential is then stepped down back to its initial value inverting the electrode reaction and also held for the same duration. The current for the forward step is described the Cottrell equation and has a $t^{-1/2}$ dependence which decays with time. The reverse current-time trace is more complicated and is given by

$$I(t) = nFAD^{\frac{1}{2}}C_{\infty}\left\{\frac{1}{(\pi[t-\tau])^{\frac{1}{2}}} - \frac{1}{(\pi t)^{\frac{1}{2}}}\right\} \qquad [4.18]$$

Comparing the forward and reverse current for the given interval following a step change in potential is a useful indicator of the reversibility and complexity of the electrode redox reactions. For an uncomplicated, reversible the ratio of the forward

current to reverse current measured after the same time interval, say a time equal to τ/2 after the potential step, should theoretically be about 0.293. If the reaction is not completely reversible then the ratio of the currents in the forward and reverse direction will not adhere to this theoretical value. This gives an indication of the reversibility of the process that is being examined. Additionally, chronoamperometry is a useful technique to accurately measure electrode area (A) by use of a well-defined redox couple (known n, C_0, and D_0). With a known electrode area, measurement of either n or D_0 for an electroactive species is easily accomplished.

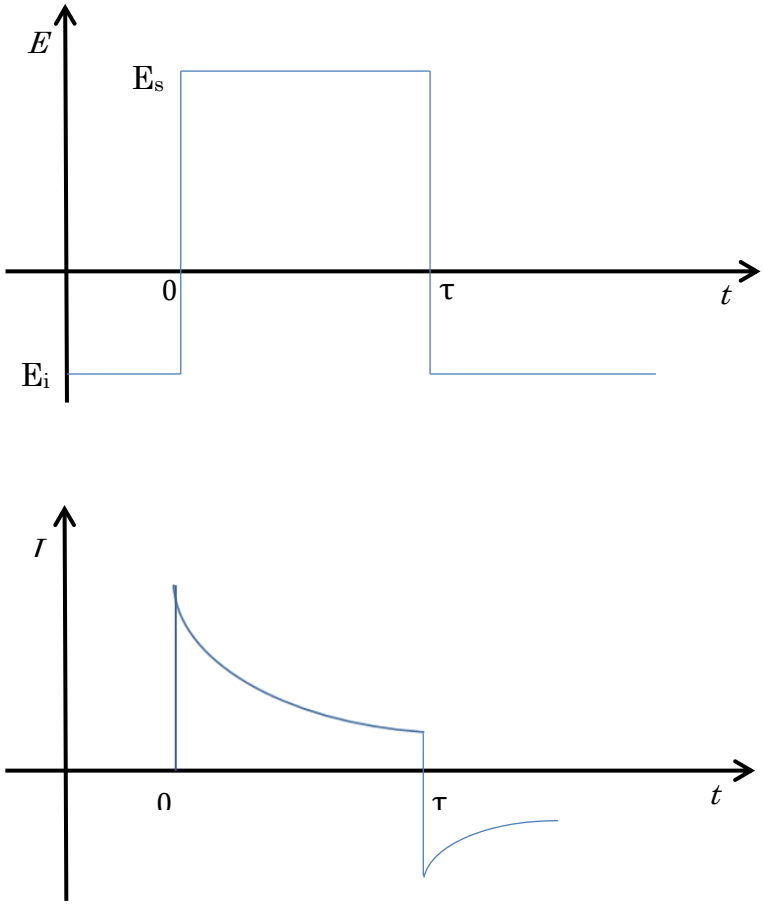

Figure 4.7: A double-step Chronoamperometry Current-time response is shown in the bottom graph, for an input potential-time profile as shown in the top graph.

4.4 Results and Discussion

4.4.1 Electrochemical Characterisation of Graphene Surface

A common method of understanding the electrochemical properties of an electrode material are by studying the surface sensitivity to inner-sphere and outer-sphere redox probes. The electron transfer kinetics differs substantially in response to these two kinds of probes and can indicate the presence of defects, impurities and inconsistencies in surface structure. Outer-sphere redox probes are referred to as 'surface insensitive' because the K^0 value is not affected by the cleanliness, presence of oxygen atoms or other neutral adsorbates. This type of probe does not depend on direct surface interaction with electrode surface for charge transfer. Rather, the electron transfer process occurs through the electrolyte medium and the electrode surface serves primarily as a source or sink for electrons and the voltammetry measurement yields information about the electronic structure and density of states in the electrode material.

Inner-sphere redox probes on the other hand are extremely sensitive to the surface and the K^0 value is very strong affected by defects, embedded impurities, and other surface adsorbates. Electron transfer occurs with the participation of surface sites, through direct contact with the electrode surface. Thus, using such a redox probe gives an indication about the surface of the electrode – in particular, the heterogeneous charge transfer rate constant is sensitive to the surface and can indicate the presence of adsorbed material or impurities on the surface, that either hinder or enhance the electron transfer characteristics. Therefore, in order to characterise an electrode surface, the responses to both inner-sphere and outer-sphere electrodes are required.

Here, the CVD grown, large-area graphene-on-glass electrode is characterised using ruthenium hexamine (an outer-spere redox probe) and potassium ferrocyanide (an inner-sphere redox probe). Cyclic voltammetric measurements using these two redox couples yield insights into the electronic and surface

structure of the graphene electrode. In Figure 4.8, a CV measurement of the electrode is shown using potassium ferrocyanide with a gold RE. This redox probe is highly sensitive to the surface impurities and from the CV measurement, it is clear that the curve is not symmetric. This indicates that the reaction is not reversible, which is supported by the current peak ratio that is approximately 0.31.

The peak-to-peak separation that is observed is around 530mV, which is much larger than for the gold electrode and indicates that there is a dearth of active sites on the graphene electrode. This is most likely due to presence of tears, small graphitic islands, and impurities introduced during the graphene transfer process. These results are supported by previous studies of CV measurements on CVD grown graphene which describe how CVD graphene exhibits a response that is similar to a distribution of randomly spaced microelectrodes. This result also ties in well with Raman data taken at different positions of the sample as well as optical and SEM microscopy images which show that there is significant impurities and defects induced in the graphene sheet.

Figure 4.9 shows the cyclic voltammetry measurements for the graphene on glass electrode using ruthenium hexamine chloride. This measurement was performed to understand the electrochemical response of the graphene sheet as a whole, towards characterising it. Because this redox probe is surface insensitive, it was observed that the graphene electrode showed a more classical cyclic voltammetry profile like a large area macro-electrode would, utilising all available active sites in the electrode area for electron transfer to take place.

The curve is however not perfectly symmetric, and the current peak ratio is 1.2, which indicates that the reaction is only quasi-reversible. This measurement was observed for a scan rate of 100mV/sec, where the peak-to-peak separation is 161mV. This is consistent with previous studies where it has been argued that the since a majority of the graphene electrode participates in the reaction, there is a heavy overlapping of diffusion zones that causes a macro-electrode behaviour.

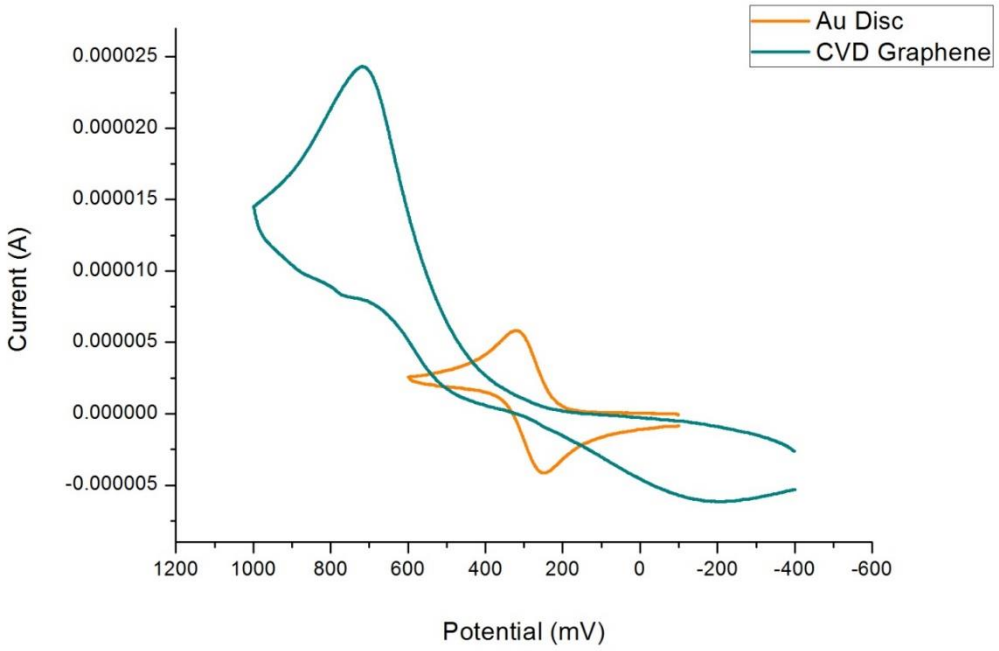

Figure 4.8: A Cyclic Voltammogram taken of CVD graphene on glass using Potassium Ferrocyanide as an inner sphere redox couple at 50mV/sec.

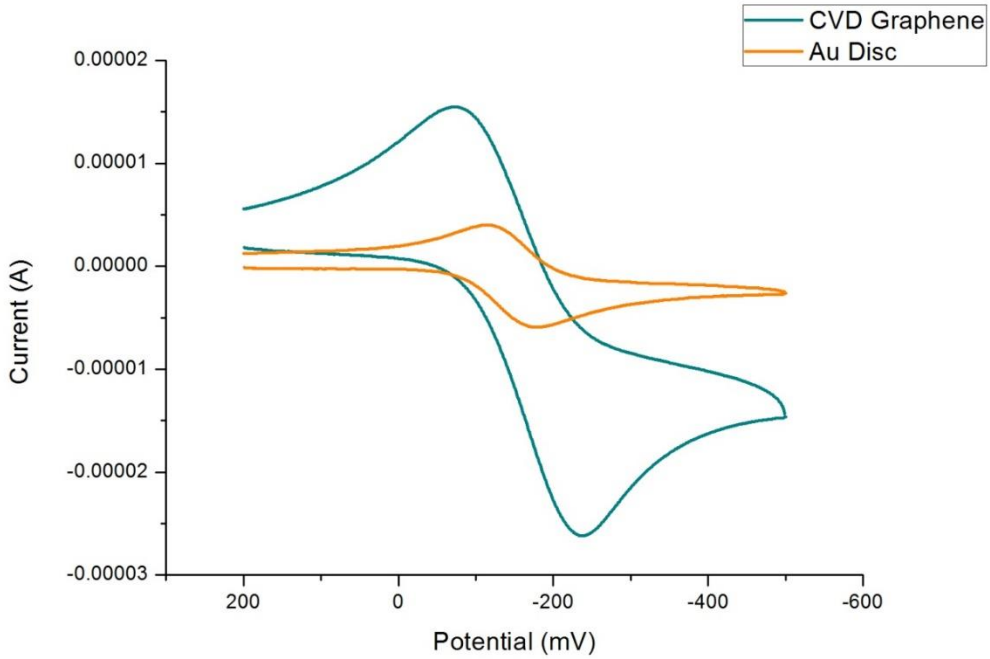

Figure 4.9: A Cyclic Voltammogram taken of CVD graphene on glass using Ruthenium Hexamine Chloride as an outer sphere redox couple at 100mV/sec.

As mentioned in section 4.3, in cyclic voltammetry experiments, in order to calculate the value for rate constant K^0, CV measurements for different scan rates are made. This is then used to calculate values for a dimensionless parameter of ψ which is inversely proportion to the square root of the scan rate. Figure 4.9 shows a plot for 8 measurements of the graphene electrode using the Ruthenium Hexamine Chloride redox probe, with scan rates ranging from 10mV/sec to 500mV/sec.

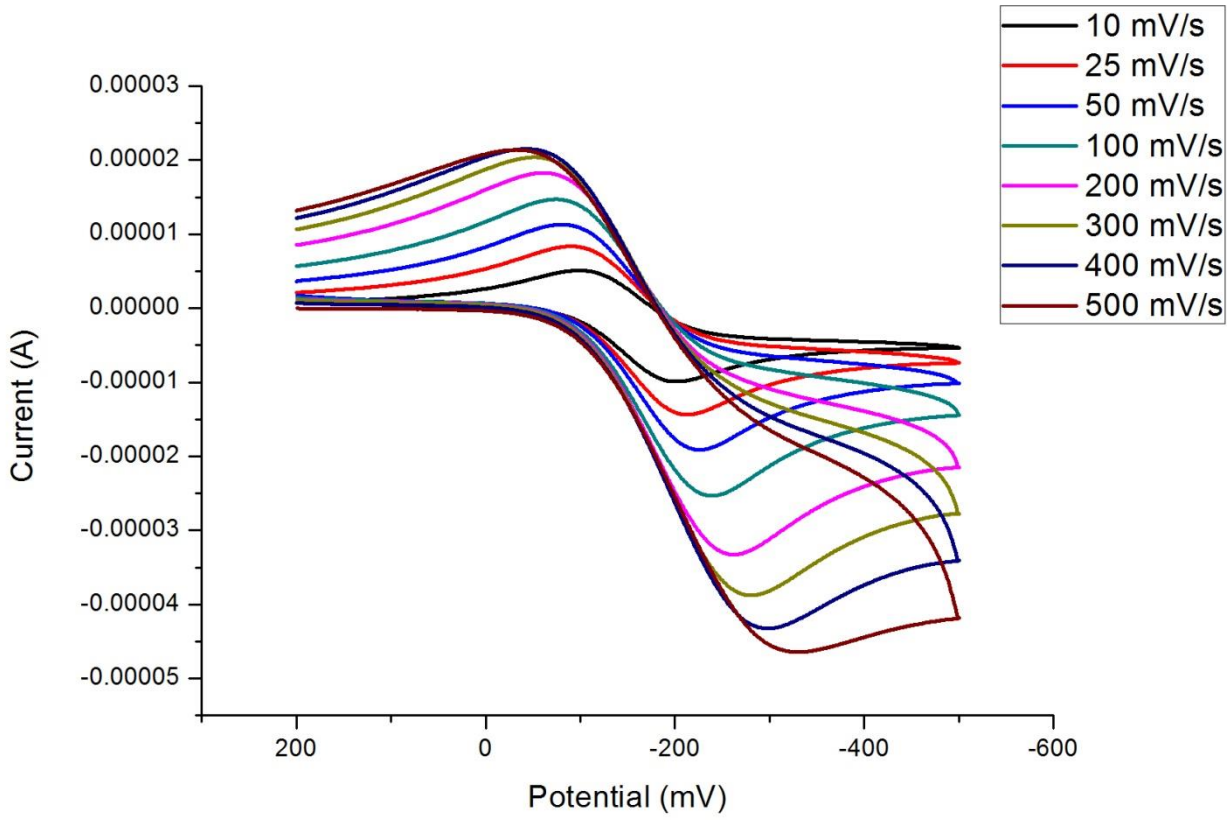

Figure 4.10: 8 Cyclic Voltammograms of CVD graphene on glass using Ruthenium Hexamine Chloride as an outer sphere redox couple from 10mV/sec to 500mV/sec.

Once the measurements are recorded for the different scan rates, the results are tabulated as in Table 4.1. Here the values of ψ are obtained for each measurement and substituting the peak separation and scan rates into equation 4.17, the value of k^0 is extracted from this.

v (mV/sec)	ΔE_p (V)	Ψ
10	102	0.55
25	123	0.36
50	143	0.24
100	161	0.195
200	200	0.12
300	226	0.095
400	254	0.07
500	295	0.045

Table 4.1: A table with the scan rate, peak separation, ψ corresponding to the data plotted in Figure 4.10

Figure 4.10 shows a plot of ψ vs. $v^{-1/2}$. As discussed in section 4.3, the rate constant of the redox reaction is proportional to the slope of the line of best fit for this graph ($5.7 * 10^{-2}$) and is found to be $k^0 = 5.73 * 10^{-5}$ cm s^{-1}. Although this is considerably slower than the gold reference electrode ($k^0 = 3.33 * 10^{-2}$).

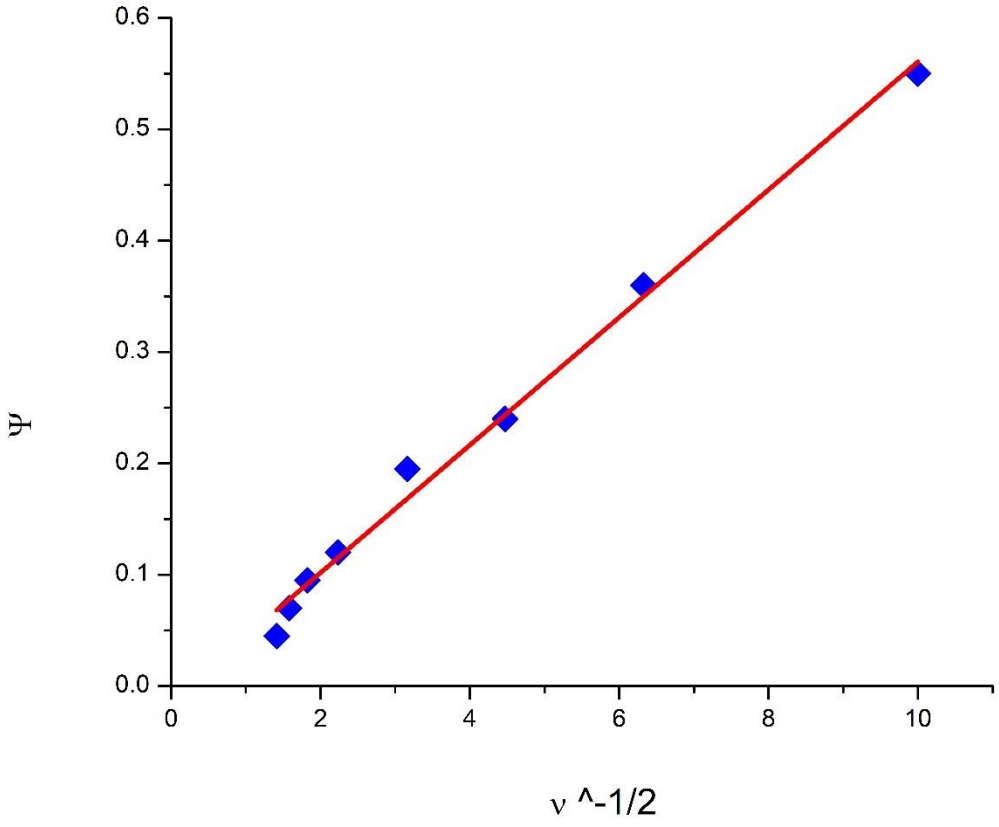

Figure 4.11: Plot of ψ vs. $v^{-1/2}$ for CVD graphene on glass using Ruthenium Hexammine Chloride as an outer sphere redox couple from 10mV/sec to 500mV/sec.

This value for the rate constant is an order of magnitude smaller than what has been reported by other groups including Velicky et al. [24]. They reported a mean value for $k^0 = 9x10^{-4}$ for similar scan rates and concentration of ruthenium hexamine used in this work, in their CV measurements on mechanically

exfoliated graphene. It must be noted however, that their experiments were formed on freshly cleaved mechanically exfoliated graphene, whereas in this work, CVD graphene has been used as the electrode surface. This would naturally affect the rate constant. Other groups such as Brownson, Banks et al. have reported values of $k^0 = 2.22 * 10^{-5}$ for similar measurements on CVD graphene. This is in general agreement with the results obtained in these experiments. [24]

4.4.2 Reversible electrodeposition of Lead on CVD Graphene

The reversible electrodeposition of metals on to transparent electrodes was first proposed in the late 1920s to affect a modulation of the optical properties of the electrode. Devices that utilise the application of an electric potential in contact with an electrolyte to cause a change in colour or transparency of the electrode are referred to as electrochromic devices. Currently, electrochromic devices have numerous applications ranging from smart windows and smart glasses to military stealth equipment.

The main requirements for such devices are that they have low power consumption and are inexpensive as well as lightweight. Essentially these devices consist of a simple electrochemical cell where transparent electrode material is the working electrode and the electrochromic material contained in the electrolyte solution is coated onto the surface the working electrode affecting its transparency.

In this configuration, the transparent electrode is the most expensive element of the configuration. In recent studies, such as by Avellaneda et al., ITO, the most used transparent conducting electrode is used as the basis for reversible electrochromic device.[18] They showed the reversible electrodeposition of $PbNO_3$ onto ITO electrode. However, due to the increasing price of raw materials required for the production, using ITO as an electrode material is increasingly cost restrictive and alternatives are being sought. Additionally, ITO is also a

very brittle in nature which makes coating it onto thin flexible substrates quite problematic.

In this work, a graphene device is demonstrated to show reversible electrochromic behaviour. Graphene is fast becoming a transparent conducting material of choice to substitute for ITO, with its attributes of being extremely light, inexpensive and unparalleled conductive properties and is a material of interest to fabricate electrochromic devices as it can be transferred onto any substrate and lends itself well to integration with hybrid organic electronic structures.

The CVD graphene on glass electrode was fabricated as described in Section 3.2. It was placed in a three-electrode electrochemical cell configuration as in Figure 4.1, with graphene as the working electrode, a reversible Ag/AgCl electrode as reference electrode and a platinum auxiliary electrode. An aqueous solution with 1.0×10^{-2} mol/L Pb(NO3)2 and 1.0 mol/L NaNO3 in the presence of 10^{-3} mol/L Cu(NO3)2 ·3H2O and ultra-pure water was used as the electrolyte solution. Copper nitrate is added. It was initially electrochemically characterized and verified that electrodeposition of the electrolyte material was possible and the optical transmission of graphene films was modulated by reversible electrodeposition of Pb onto the graphene film.

Chronoamperometric measurements as detailed in section 4.3.2 were made on this electrochemical cell. A voltage of -1V was used as the positive step voltage. The voltage was applied and the resulting deposition of Pb is studied by measuring the changing current as a function of time. The current is then switched to the negative potential of +1V so as to reverse the deposition process, causing the dissolution of the accumulated lead back into the electrolyte solution. A current-time profile is recorded during the cyclic deposition-dissolution process of lead metal on the graphene film.

Figure 4.11a shows the potential that was applied as a function of time and Figure 4.11b is a record of the current response. As described in section 4.3.2, this potential profile is a modified double-step chrono-amperometric profile. The

potential was cycled between -1V for a period of 20 secs and +1V for a period of 20 secs with a small time lag of 5secs at 0V. The current response for the graphene electrode showed the characteristic correspondence to the Cottrell equation for the dissolution of the Pb from the graphene surface and $t^{-1/2}$ dependence. The transparency of the electrode was also observed to switch from transparent to opaque reversibly and Figure 4.12 shows screenshots from a video which was taken over 20 cycles of the switching of the potential showing the reversible electrochromic behaviour.

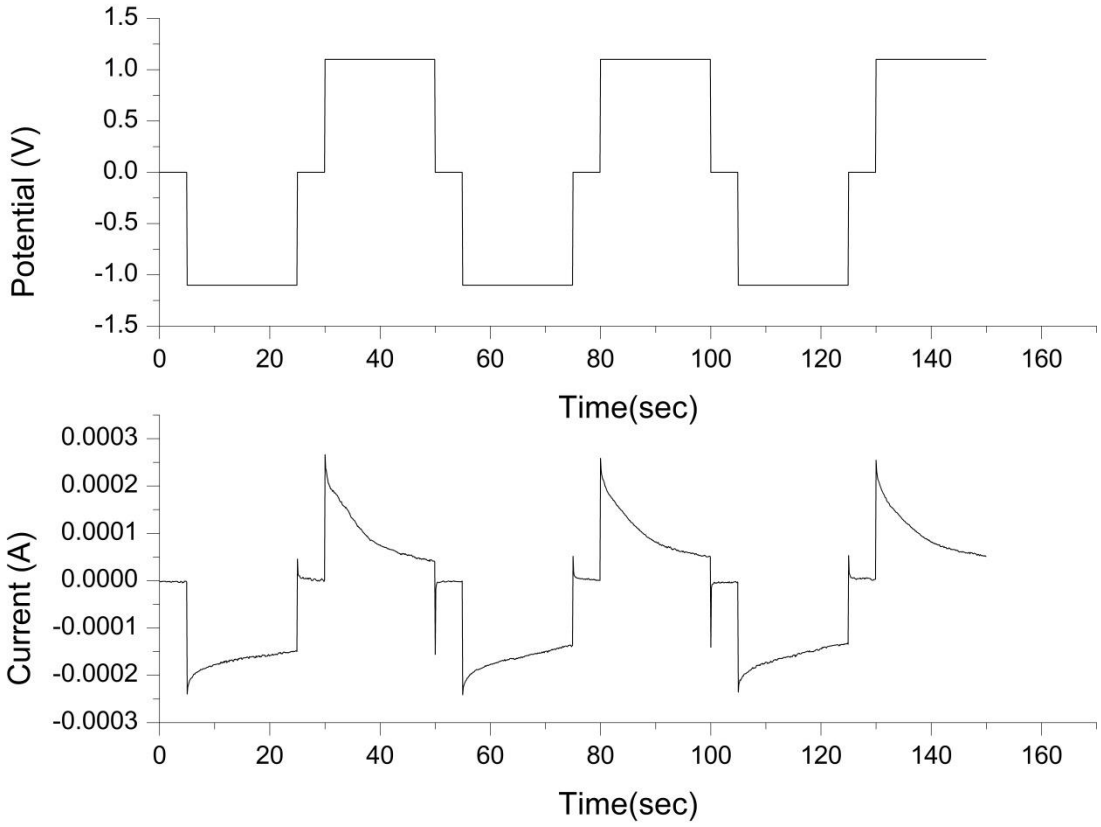

Figure 4.12: Graphs showing a) The potential-time profile that the graphene electrode is subjected to. b) the corresponding current-time profile observed.

Additionally, the ratio of the dissolution current to the deposition current taken after half the time period for this measurement run is 0.266, which is close to the

theoretical value of 0.293 and reveals that the reaction is close to being completely reversible. Moreover, this technique can be used to calculate the effective surface area of the electrode that is actually in electroactive using equation 4.18. Using a diffusion constant for $Pb(NO_3)_2$ as 1.273 and a bulk concentration of 0.01M, the active electrode area was found to be 0.5726 cm^2. This is roughly about 80% of the transferred area that is free to interact with the electrolyte species. This discrepancy is accounted for by the tears and defects on the graphene surface that interfere with a particular area of the electrode interacting with the electrolyte species. And this can also be visualised in Figure 4.13c where some area within the electrode window have not been coated with the Pb.

In the course of experiments, 4 graphene devices were measured. It was observed in all of them that the graphene electrode was able to show reversible deposition-dissolution characteristics in all of them for atleast 30 cycles. After 30 cycles, the graphene electrode began to show some saturation behaviour. That is, the deposition current was getting smaller and smaller and the active surface area reduced dramatically.

This was correlated with a non-reversal of the transparency back to the original state. Figure 4.14 shows a current-time response after 30 cycles are completed. The first deposition current shows a characteristic behaviour. However, despite elongating the duration of the voltage of the dissolution, the current characteristics are anomalous and appear to be flat for the duration of potential step. This is interpreted as due to the saturation of the surface with Pb and an entanglement of the Pb within the graphene films impurities.

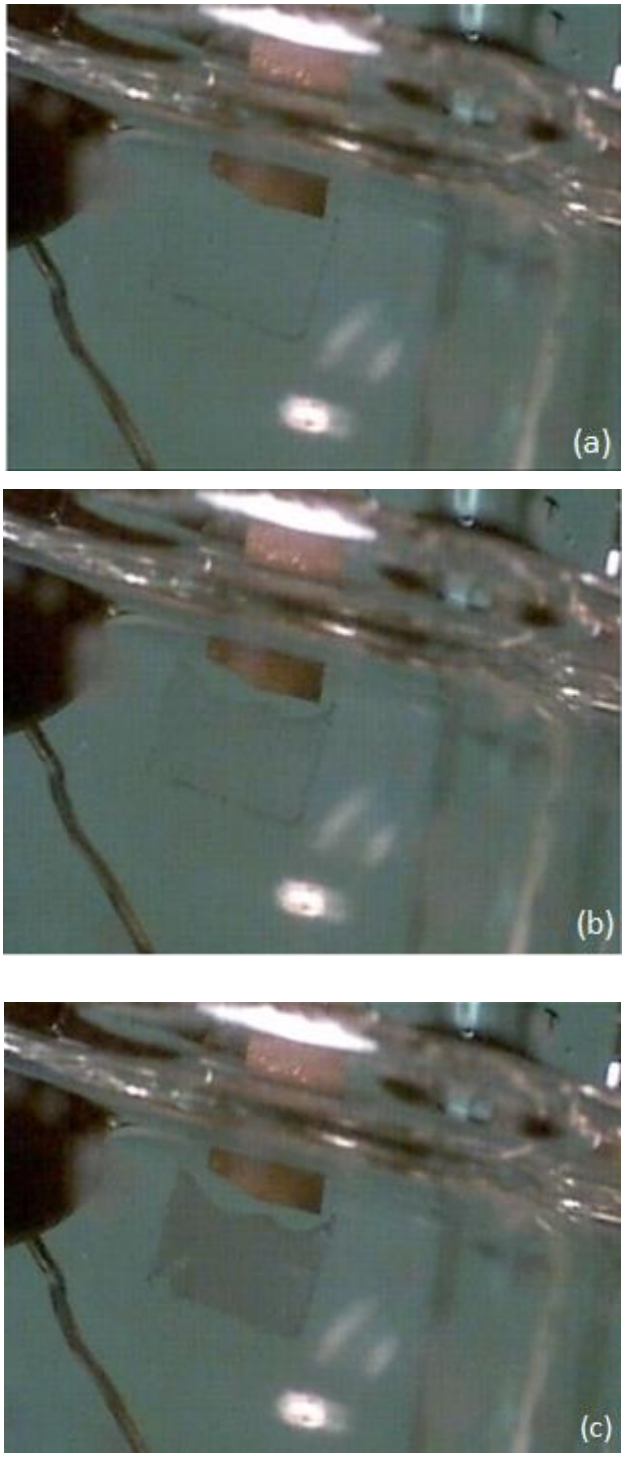

Figure 4.13: Photographs a), b) and c) are screenshots from a video taken 5 seconds apart during the electrodeposition of Pb as the voltage is swept from at a) t=0secs b) t= 5sec and c) t=10secs after the voltage is switched from 0 to -1V. It is clearly seen that a change in the transparency takes place as a result.

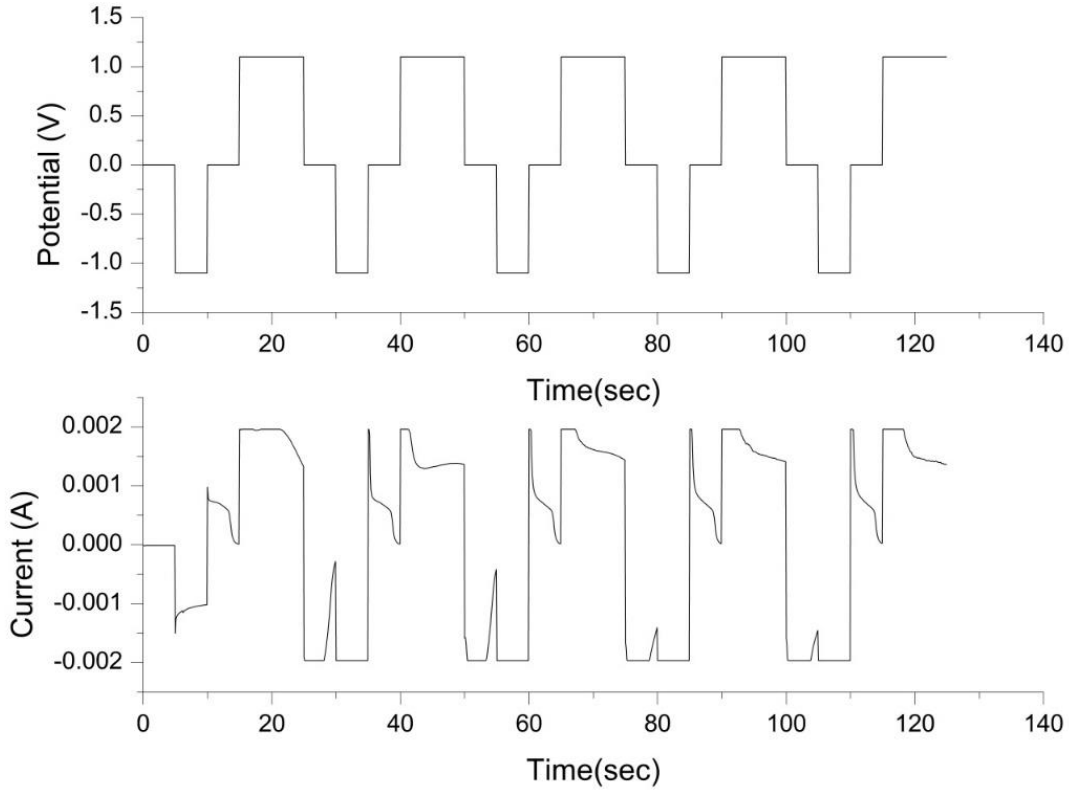

Figure 4.14: The potential-time profile applied and the current-time profile measured showing the impaired performance of the graphene electrode due to accumulation of Pb in graphene film.

To investigate if the Pb could be removed, a positive potential was repeatedly applied as in Figure 4.14, so as to act as a stripping voltammetry potential. This is a technique used to remove metallic impurities from electrode surface that can be oxidised and dissolved into solution. It can be seen from the current response that successive application of the positive potential does result in removal of the Pb, such that after 6 cycles, the current response then reaches a plateau. This is understood to be the point beyond which trapped Pb could no longer be oxidised into solution.

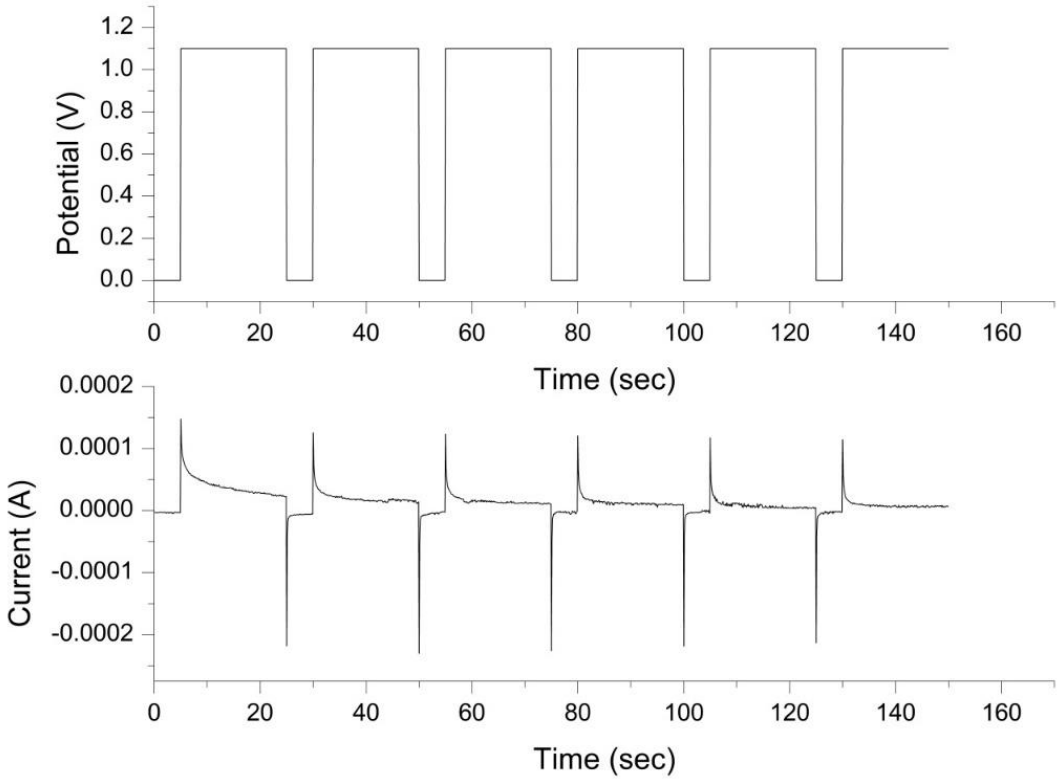

Figure 4.15: A potential-time profile applied to remove residual Pb on the graphene electrode surface.

Furthermore, this was verified by performing the chronoamperometry measurement again on the same sample. Figure 4.15 shows the current response to applied positive potential steps for 5 cycles and it is clear by observed the improved current response to the application of a negative potential that some of the surface is restored and deposition of Pb is able to take place. However, the response is not characteristic as described in section 4.3.2 and the current ratio value has significantly shifted.

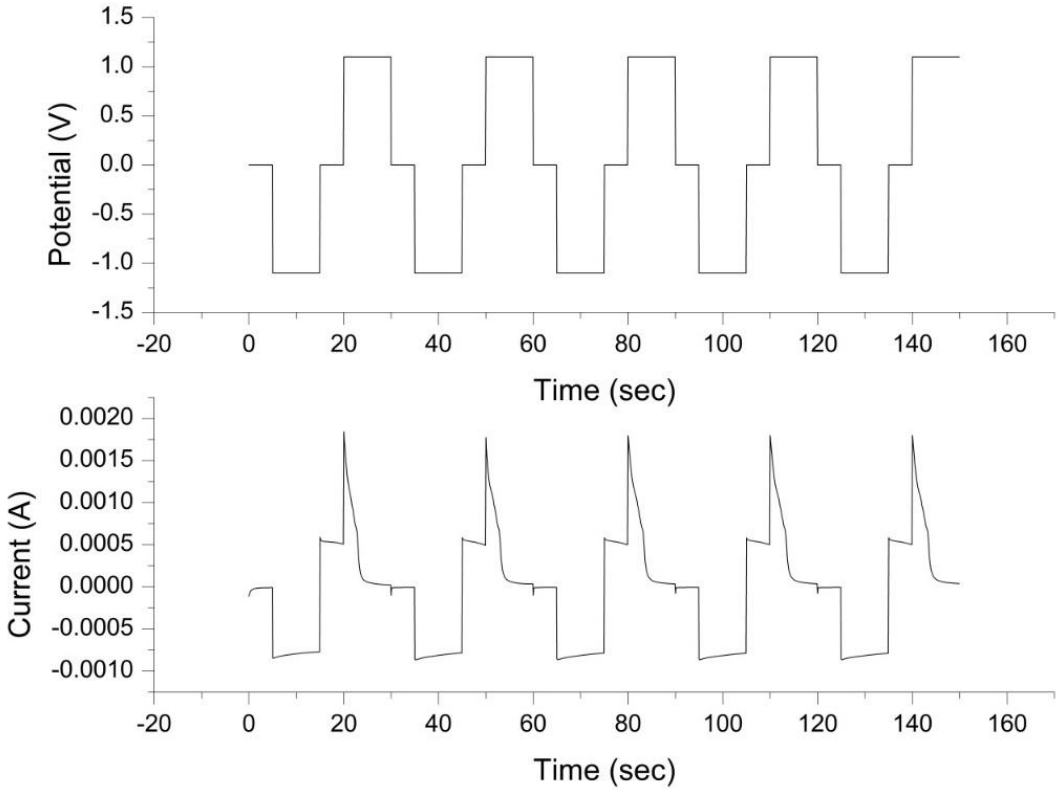

Figure 4.16: A potential-time profile after the electrochemical dissolution of accumulated Pb on the graphene electrode surface.

This demonstrates that after about 30-40 cycles the graphene surface starts to degrade. While some of the electroactivity can be restored through cycling through positive potential steps to facilitate the removal of adhered metal, the surface is not completely restored. Several factors including the cleanliness and defect density of the graphene can affect the sample's electrochromic performance. Therefore, cleaner and defect-free devices need to be prepared to elongate the life cycle of the device. Additionally, Pb is not a very environmentally friendly material to work with and alternate metal complexes could be investigated for their use in graphene based electrochromic devices.

4.5 Conclusion

The electron transfer behaviour studies of graphene using cyclic voltammetry (CV) of redox couples, $[Fe(CN)_6]^{-3/-4}$and $[Ru(NH_3)_6]^{+3/+2}$ were studied and it was shown that the graphene exhibited well-defined redox peaks. Both anodic and cathodic peak currents in the CVs are linear with the square root of the scan rate, which suggest that the redox processes on graphene-based electrodes are predominantly diffusion-controlled. It was verified that $[Ru(NH_3)_6]$ is a nearly ideal outer-sphere redox system that is insensitive to most surface defects or impurities on electrodes and can serve as a useful bench-mark in comparing electron transfer of various carbon electrodes; $[Fe(CN)_6]$ is was also shown to be "surface- sensitive" but not "oxide-sensitive. The apparent electron-transfer rate constants calculated from cyclic voltammograms on graphene are $5.73*10^{-5}$ cm/s for $[Ru(NH_3)_6]$. This indicates that the unique electronic structure of graphene, especially the high density of the electronic states over a wide energy range endows graphene with fast electron transfer. The rate for $[Fe(CN)_6]^{-3/-4}$ on graphene was calculated to be $4.9*10^{-3}$ cm/s. These results are comparable results to studies in the literature. These indicate that the electronic structure and the surface physico-chemistry of graphene are beneficial for electron transfer and thus can form a good platform for electrochemical sensing of biomolecules.

Further, graphene was used as a working electrode to create an electrochromic device where the optical transparency of the graphene was modulated and the electrochemical characteristics of the graphene device were examined. It was seen that graphene could sustain reversible electrodeposition of Pb onto its surface for up to 40 cycles. After this, some degradation of the surface was observed. The surface was renewed by applying a positive potential step to oxidise the deposited Pb and dissolve it into solution. However, this was not able to fully refresh the surface and restore it to its original state. In this regard, more work needs to be done to improve the longevity of the electrochromic device as well as explore the usage of other electrolytic solutions.

4.6 Bibliography

1) Dragoman, M., Dragoman, D, Prog. Quantum. Electron. 2009, 33, 165–214.

2) Novoselov, K.S., Jiang, D., Schedin, F., Booth, T.J., Khotkevich, V.V., Morozov, S.V., Geim, A.K. Two dimensional atomic crystals. PNAS 2005, 102, 10451–10453.

3) Ping An Hu, Jia Zhang, Le Li , Zhenlong Wang , William O'Neill, Pedro Estrela, Sensors 2010, 10, 5133- 5159

4) Wan Li,Cen Tan,Michael A. Lowe,Hector D. Abruna, D. C. Ralph. ACS Nano 2011, Vol.5, No.3, 2264-2270

5) D.A.C. Brownson and C.E. Bank, The Handbook of Graphene Electrochemistry Springer 2014

6) Allen J Bard and Larry R Faulkner, Electrochemical Methods Fundamentals and Applications. J Wiley and Sons 1980

7) Christopher M A Brett, Ana Maria Oliveira Brett Electrochemistry – Principles, Methods and Applications Oxford University Press 1993.

8) D.A.C. Brownson and C.E. Bank, Phys. Chem. Chem. Phys., 13 (2011) 15825-15828.

9) Dale A C Brownson, Dimitrios K Kampouris and Craig E Banks, Chem Soc Rev 2012 , 41, 6944-6976

10) Li, X., Cai, W., An, J., Kim, S., Nah, J., Yang, D., Piner, R., Velamakanni, A., Jung, I., Tutuc, E., Banerjee, S. K., Colombo, L., Ruoff, R. S. Science 2009, 324, 1312-1314

11) J Won Suk, Alexander Kitt, Carl W. Magnuson, Yufeng Hao, Samir Ahmed, Jinho An, Anna K. Swan, Bennett B. Goldberg, and Rodney S. Ruoff *ACS Nano*, 2011, 5 (9), pp 6916–6924

12) Pumera, M et al., 2009. Chem. Rec. 9, 211–223.

13) W. J. Lin, C. S. Liao, J. H. Jhang, Y. C. Tsai, Electrochem.Commun. 2009, 11, 2153.

14) L. H. Tang, Y. Wang, Y. M. Li, H. B. Feng, J. Lu, J. H. Li, Adv. Funct. Mater. 2009, 19, 2782.

15) N. G. Shang, et al, Adv.Funct. Mater. 2008, 18, 3506

16) M. Zhou, Y. M. Zhai, S. J. Dong, Anal. Chem. 2009, 81,5603.

17) Shao, Y. Y., Wang, J., Wu, H., Liu, J., Aksay, I. A., Lin, Y. H.. Electroanalysis 2010, 22, 1027–1036

18) Cesar O. Avellaneda_, Marcos A. Napolitano, Evandro K. Kaibara, Luis O.S. Bulh˜oes Electrochimica Acta 50 (2005) 1317–1321

19) Yuan Huang, Eli Sutter,Norman N. Shi, Jiabao Zheng, Tianzhong Yang, Dirk Englund, Hong-Jun Gao, and Peter Sutter *ACS Nano*, 2015, 9 (11), pp 10612–10620

20) *A.K Geim Science* 19 Jun 2009: Vol. 324, Issue 5934, pp. 1530-1534

21) Adriano Ambrosi, Chun Kiang Chua, Alessandra Bonanni, and Martin Pumera Electrochemistry of Graphene and Related Materials *Chem. Rev.*, **2014**, *114* (14), pp 7150–7188

22) Liang et.al., Toward Clean and Crackless Transfer of Graphene,ACS Nano, 2011, 5 (11), pp 9144–9153

23) Li et.al., Transfer of Large-Area Graphene Films for High-Performance Transparent Conductive Electrodes, Nano Lett., 2009, 9 (12), pp 4359–4363

24) Velicky et al. ACS Nano VOL. 8 ' NO. 10 ' 10089–10100 ' 2014

Chapter 5

Electronic Sensing of PCT with Graphene

5.1 Introduction

Graphene is being investigated exhaustively for its potential as a sensing element in a whole array of different sensors. It is believed to be highly promising for the development of new types of chemical/biological sensors with ultrahigh sensitivity because it is a two-dimensional material and every atom can be exposed to the surface adsorbates. [1] Moreover, due to synthesis methods such as CVD, large surface area can be achieved, which increases the available area of interaction of graphene with the analyte. Graphene's exceptional conductive properties along with a zero-band gap are also extremely beneficial for conducting electrons across the biomolecule-graphene interface.[1][2] Additionally, properties of graphene such as large domain size that ensure a low level of excess (1/f) noise caused by thermal fluctuations, high signal to noise ratio, ease of functionalization, high mechanical strength, high thermal conductivity[3-5], high carrier mobility and carrier density along with the fact that graphene is sensitive to both electron-donor and acceptor molecules, renders graphene-based devices of great interest for sensing applications[1][2].

Graphene has been studied extensively as an electrode material in Electrochemical sensors due to its wide anodic potential range, chemical inertness, low cost and high surface area. The large surface area has been demonstrated to be highly sensitive to electrochemical redox reactions occurring near the surface and many studies have reported high sensitivity to the electrochemical detection of molecules such as dopamine, serotonin, Ascorbic Acid, Glucose etc. [7] Hybrid sensors that involve both electrochemical response in conjunction with optical detection methods are also widely explored.[7] However, while most of these reports do indicate the superior performance and sensitivity of graphene electrode sensors in terms of sensitivity, not all of them are suitable for large-scale manufacturing, which is essential for commercialization of a bio sensing platform. And this is where electronic sensing platforms can offer the potential to scale-up. [8]

5.1.1 Graphene-Based Electronic Sensors

Graphene-based Nano-electronic devices are of special interest as sensors because of graphene's incredible electrical properties. Many reports have shown the successful realization of graphene/graphene-functionalised FET sensors for a whole array of chemical and biological species including DNA sensors, gas sensors (H_2, CO, NH_3, Cl_2 , NO_2 O_2 etc.) glucose, and pH sensors.[6-9]

Graphene nano-electronic sensors have several advantages over other sensing methods such as electrochemical sensors. Firstly, they utilize the exceptional electrical properties of graphene and have been shown to be exceptionally sensitive to any electron transport at the surface. They are extremely versatile to work with and can be patterned and incorporated into any desired architecture with standard nanofabrication techniques. Moreover, the graphene channels are easily miniaturized or scaled up as required and can be readily integrated into lab-on-chip applications. As a result, there is great potential for creating low-cost, large scale and low power consumption devices with high sensitivity in the sensor platform. Additionally, graphene-based FET channels offer the possibility of integration with other detection techniques (such as fluorescence, plasmonic etc.) to analyze and detect multiple analytes simultaneously. [6][10][11]

A FET device relies on an electric field to manipulate and control the conduction through the channel. Graphene-based FET devices have been used to detect DNA, proteins, bacteria and even malarial parasites. Additionally, a lot of interest has been shown to solution gated FETs because the electrolyte solution can be gated and offer additional control over the conductivity of the channel. Modulation of the conductance channel in solution-gated FETs can be achieved by applying a gate potential across the electrolyte, which acts as a dielectric. Because of the ambipolar characteristics of graphene, both hydroxyl (OH-) and hydroxonium (H3O+) ions are proposed to be able to modulate the channel conductance of graphene-based FETs. Electrolyte-gated graphene-based FET for detecting protein adsorption were demonstrated by Ohno et al. [12] The monolayer graphene channel was not functionalized and exhibited a linear increase in the conductance depending on the electrolyte pH, thus indicating its potential use in a pH sensor. Their work further suggests that the conductance of the graphene-based FET increased with the adsorbed protein (bovine serum albumin) at a level of several hundred picomolars. This implies that that the graphene-based FET can be used for highly sensitive electrical biosensors.

Chen et al. demonstrated that CVD-grown large-sized graphene films were used to fabricate liquid gated transistors for a DNA sensor with a detection concentration as low as 0.01 nM, they found that adding AuNPs on the surface of graphene devices can extend the upper limit of DNA detection due to the increase in loading of probe DNA molecules. [14] Single layer graphene FETs made fabricated from CVD graphene were also used to demonstrate the use of graphene as a glucose sensor by Huang et al. [15] They demonstrated real-time sensing for glucose and glutamate molecules. This was done by linking a specific enzyme (glucose oxidase or glutamic dehydrogenase) to the graphene surface and studying the conductance change of the graphene transistor as a result of the analyte molecules being oxidized by the enzyme. Their work indicates that graphene, and CVD graphene in particular, has potential that can be utilized towards making real time nano-electronic biosensors.

5.1.2 Sensing Proteins

A biosensor is a device that responds to changes in the biological environment and produces a signal in response that can be read out and interpreted to gives us information about the environment. A biosensor typically consists of three parts. The first part is the biologically sensitive element – this could be anything from enzymes and antibodies to DNA or other bio-active surfaces which are artificially engineered which is responsible for interacting with the analyte species. The second part of the sensor is the detector (or transducer). The mechanism of detection could be chemical, optical, electrochemical etc. Essential, the detector converts a signal from the interaction of the analyte in the environment with the biologically sensitive element into some signal that can be easily measured. The third part of the sensor consists of the associated read-out electronics that allow us to access the information about the analyte in a sensible way.

There are primarily two requirements to fulfil when designing a sensor, namely, how sensitively it responds to changes in the environment and how specific the response is to the analyte that one desires to sense. Ideally, for commercial usage, it should also be inexpensive, non-invasive if possible, have a large and appropriate range of detection, be easy to use and reliable in its response over a long period of time.

A special kind of sensor that is designed to be able to detect proteins is called an Immunosensor. An immunosensor is a biosensor where the sensing element is an antibody, where the basis of the detection is the specific affinity and molecular interaction between an antibody and the protein that the sensor is designed to detect. An antibody is a large Y-shaped protein molecule, also known as an Immunoglobulin that is produced by the immune system in response to an infection by a pathogen. They typically consist of 2 distinct types of chains of amino acids constituting the Y-Shaped structure, 2 heavy chains and the other 2 being lighter chains. The antibody is designed to be able to recognize and neutralize foreign substances in the body known as antigens. The tip of the

'Y' structure contains a paratope that is specific to an antigen allowing the two molecules to bind to each other using what is known as complementary determining regions that correspond to the topography of the binding sites and making them unique in their interaction with detected molecule or epitope.

This type of binding mechanism has two consequences. Firstly, it tags pathogen molecules with the primary amine sulph-hydryl and carbohydrate groups from the antibody and enables the immune system to recognize and attack them. Secondly it also blocks key sites in the pathogen molecule that are associated with key reproductive or infective processes, thus effectively impairing the pathogen molecules. Most pathogens trigger antibody response in a human immune system. It is believed that there are over 10 billion different antibodies that the human system is capable of synthesizing. Consequently, detection of specific antibodies is often highly indicative of a specific pathogen or its associated disease and medical diagnostic techniques routinely include tests for specific antibodies. Additionally, many autoimmune diseases can also be associated with the incorrect immune response where antibodies bind the body's own epitopes.

Immunosensors employing a variety of different detection mechanisms have been reported (fluorescence, electrochemical, FET etc.) Some of them employ labels such as enzymes or fluorescent molecules that can be optically detected and other methods for label-free detection assays using such as surface plasmon resonance, or direct electrochemistry have also been reported. [16-19]

If a label, such as an enzyme is used, then the technique is referred to as a labelled Assay. These types of sensors are designed to measure the presence and quantity of an antibody and antigen by labelling the molecule with some kind of tag that is luminescent, fluorescent or even radioactive. For instance, the most commonly employed immunosensor assay in clinical diagnosis is called ELISA or Enzyme-Linked Immunosorbent Assay. The time of Assay is used to correlate the event of a specific enzyme labeled antibody with the antigen it is meant to detect and convert it into a optical or electrochemical signal. Although ELISA is extensively used and highly sensitive and reliable, there are some drawbacks

with this type of assay. For instance, long incubation period, complex apparatus, complicated storage conditions (to ensure the Enzyme does not denature), short shelf life, does not lend itself well to point of care devices etc.

The alternative to labelled immunosensors are referred to as label-free sensors. This category of sensors enables the direct measurement of physico-chemical changes that are triggered at the point of the antibody-antigen complex formation. This is a useful technique and has some advantages. Firstly, there are several different mechanisms by which the signal can be transduced – typically electronically, optically or electrochemically. Reports also demonstrate transduction using piezoelectric measurements such as A quartz crystal micro-balance in the detection of Glucose. [20]

The most common method of label-free signal transduction is by using electrochemical measurements such as amperometry, voltammetry, electrochemical impedance spectroscopy etc. Optical methods include detection of changes in colour, absorption, reflectance as a result of a binding event. Surface plasmon resonance is another technique that is recently being developed and used for the detection of protein molecules. Piezo-electric transducers are also able to recognize a binding event due to an increase in the mass of the antibody complex and finally electrically transduction can be used to detect changes in current, conductance modulations, charge accumulation in response to a binding event that happens near the sensing element.

5.1.3 Sepsis and Procalcitonin

Sepsis is a very serious medical condition where the immune system in the body responds to an infection and then begins to attack the body itself and cause serious damage the organs and tissues. The onset and progression of Sepsis through 4 different stages, starting with systemic inflammatory response (SIRs), then moving through the stages of sepsis, severe sepsis and septic shock can be rapid and fatal if proper treatment is not administered. Without rapid and accurate diagnosis and treatment, the risk of death in a patient rises significantly (For sepsis stage upto25%, severe sepsis upto50% and septic shock upto75%) with every

passing hour. The mortality rates of all patients that suffer sepsis is about 30% and children and elderly patients have even lower recovery rates.[21] In order to properly diagnose the onset, clinicians increasingly rely on biomarkers that are associated with sepsis, to differentiate between the different pathogens that might be a cause of the infection, so that appropriate antibiotic treatment may be administered if the cause of the infection is bacterial. Conventional diagnostic methods like blood culture tests take upto 48 hours and can delay the diagnosis and treatment. And it has been shown that Antibiotic treatment is most effective when administering antibiotics is commenced within 4 hours of admission to hospital. [21]. More recently, other techniques such as ELISA and DNA extraction assays have been developed that shorten the duration to 4-6 hours, and while they have reduced the time for diagnosis, there is still a need for real time monitoring of the levels of the biomarker which is not possible with these methods. This real-time measurement would be extremely useful to keep track of how the patient is responding to treatment and whether the infection is being successfully combatted. [21][22]

There are a few biomarkers that are associated with sepsis namely, procalcitonin, tumor necrosis factor-alpha and C- reactive protein. Of these, the biomarker most strongly associated with the onset of sepsis as a result of a bacterial infection is procalcitonin. Procalcitonin (PCT) is a protein that consists of 116 Amino Acids. It is produced in certain cells in the thyroid and in the lungs and intestines of humans. Healthy humans have negligible quantities of procalcitonin in their blood (<0.01 µg/L), however, the onset of sepsis has been linked to a sudden increase in the concentration of PCT and an increasing concentration of PCT in the blood is associated with increasing severity of the Infection and a progression of Sepsis into its further stages. SIRS is associated with PCT concentrations of 0.5-2 µg/L, Sepsis is indicated when PCT concentrations lie between 2-10 µg/L and Severe Sepsis and Septic shock are associate with PCT levels from 10 µg/L upto 100 µg/L.

Recent studies have developed optical, fluorescence and electrochemical methods of detecting the presence and quantity of PCT in blood. Additionally, it has been shown that simultaneous detection of PCT, TNFa and CRP can be achieved using

a microfluidic lab-on-chip device. These techniques are an improvement over existing commercial assays and use various techniques (fluorescence, chromatographic) to produce quantitative results in under 1h. However, these tests do not yet allow for point of care measurement of PCT and continuous monitoring of the biomarker levels. Therefore, designing a sensor that could not only be utilized as a point-of-care test but that could also be integrated into a larger system to allow continuous monitoring would be of great value.

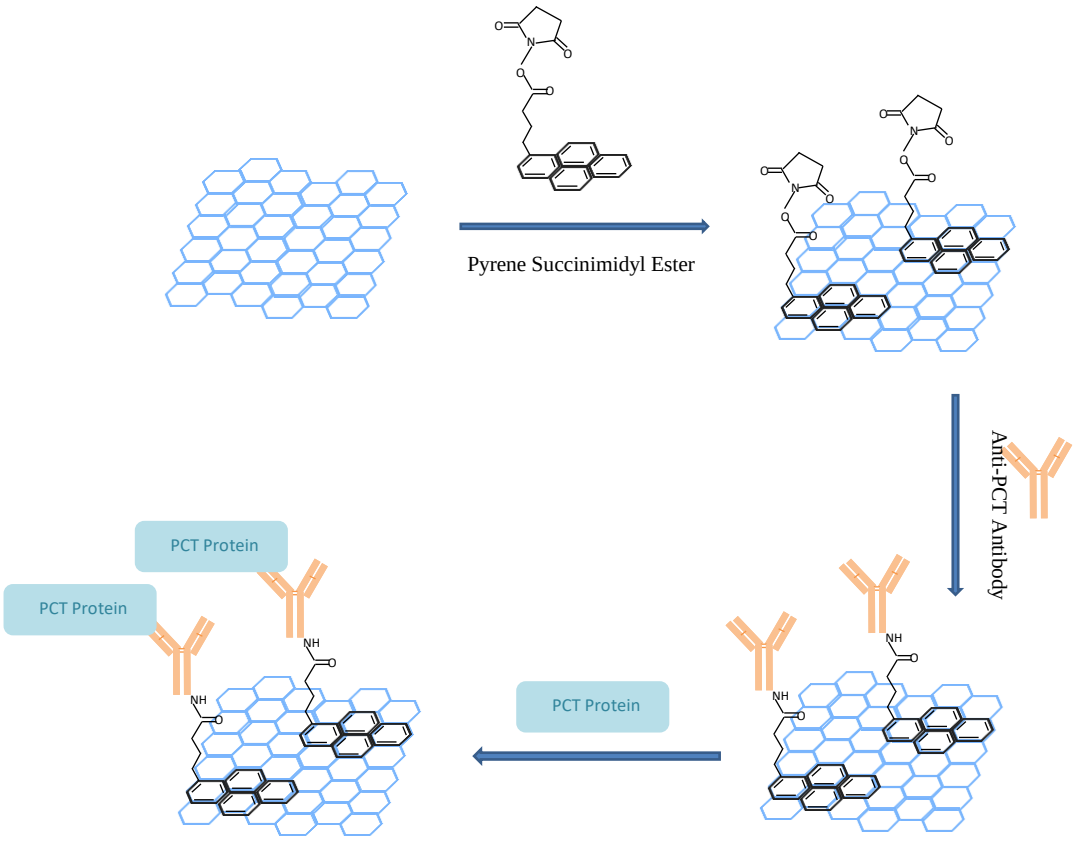

Figure 5.1: A Schematic of the binding events of PSE to graphene, Antibody to PSE and finally PCT to Antibody.

In this chapter, the development of a proof of graphene-based FET device for use as an immunosensor for the sensitive detection of Procalcitonin using a label-free electronic transduction mechanism is discussed. This type of device can lend itself well to sensitive, selective, detection in real-time with the potential to be integrated into portable point of care system.

5.1.4 Functionalization of Graphene

As discussed in section 6.1.2, in order to be able to sense the presence of a protein, in this case PCT, a complementary molecule or antibody is needed. In this experiment, Anti-PCT antibodies, which are the complementary antibodies for the PCT, need to be electrically coupled to the graphene surface. In other words, the graphene surface needs to be functionalized with the antibody such that the conductance of the graphene sheet is affected by the PCT-antibody binding event.

This functionalization is best achieved through a non-covalent bonding of the linker molecule to the graphene sheet using what is known as π–π stacking interactions. This is a special kind of bonding interaction that occurs typically between two large non-polar organic compounds that have aromatic rings, overlapping π orbitals and delocalised electrons. In terms of the strength of the bonding, they are comparable to covalent bonds and much stronger than other kinds of inter-molecular interactions like hydrogen bonding and coordinate bonding. Moreover, π–π stacking does not disrupt the highly conjugated structure of the graphene sheet, and therefore does not impact on the electronic and structural properties of graphene that are relied upon for high sensitivity of the sensor. Many studies report, that graphene sheets functionalised with π–π stacked molecules that are stably adsorbed, have been successfully utilised in sensor platforms. [16][18][20] Chen et al studied the effect of different groups on the electronic structure of graphene, showing how some like tetrafulvalene (TTF) tend to p-dope the graphene sheet, whereas other molecules such as hexaazatriphenylene-hexacarbonitrile (HATCN) tend to cause n-doping of the graphene.[20]

In this work, an aromatic Pyrene-based linker molecule is used as the bridge between graphene and the Anti-PCT antibody. 1-Pyrene Butanoic Acid Succinimidyl Ester (PBASE)is an aromatic molecule that has been widely used as a linker to attach biomolecules to a graphene surface. The role of the linker is to serve as the anchor to attach the recognition element of the sensor to the

graphene sheet. It has previously been shown that PBASE has a strong affinity to the graphene sheet and adsorbs in a stable configuration on the graphene surface.

This molecule consists of two parts: the four-benzene ring aromatic base and connected by a short chain, an active ester group. Since graphene can be regarded as an infinite aromatic molecule and pyrene has 4 π–π binding sites, the interaction between PBASE and graphene is such that they are stacked parallel to each other, with the PBASE- graphene stacking distance is 2.3 Å , thus maximizing their interaction and making the linker very stable. The aromatic base pyrene moiety is the part of the molecule that stacks on to the basal plane of graphene. And the ester group which can act as a binding site for various biomolecules such as antibodies, enzymes etc. It is the ester group that is responsible for being able to link directly to a biomolecule which has an amine group at one end, through the formation of an amide bond. G.Wu et al have shown that effect on the electronic properties of the graphene sheet after PBASE is stacked on it. It was shown that the PBASE molecule has an electron withdrawing nature and this results in the p-doping of the graphene sheet, causing the dirac point to shift to the right on the order of about 0.25V [24].

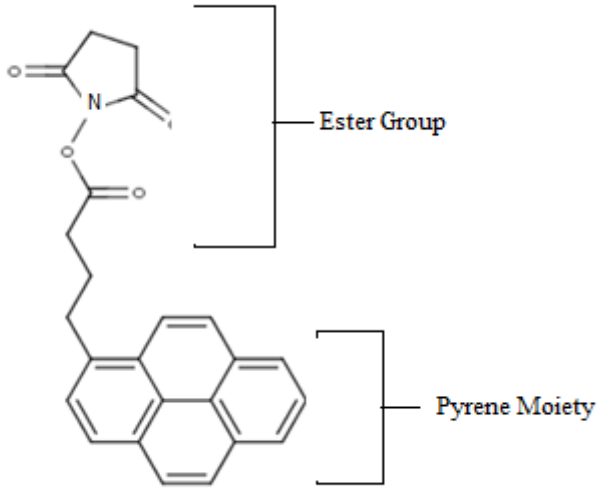

Figure 5.2: The structural representation of the PBASE molecule

5.2 Experimental Methods

The step-by-step fabrication of the CVD graphene device on a SiO_2/Si substrate that is used in the experiments (as discussed in section 5.3) has already been detailed fully in section 3.3 . This section describes the experimental methods required for the measurement of the device starting with the functionalisation of the graphene surface, followed by the device layout, the measurement set up and reagents that were to study the electrical response of antibody and PCT binding events on a functionalised graphene surface.

5.2.1 Functionalization of Graphene

As described in Section 5.1.4, the graphene sheet needs to be functionalized with the PBASE linker molecule. In order to achieve this, the following steps were performed:

1) After all stages of lithography and lift off are complete, and the graphene sheet is contacted to metal contact pads, the graphene/ SiO_2/Si substrate is gently cleaned by rinsing in acetone and IPA for two minutes each. It is then immersed into a beaker containing PSE dissolved in methanol for 20 mins.
2) The substrate is then rinsed in methanol followed by rinsing in ultra-pure DI water after which is dried using an N_2 gun and placed on a hot plate for 5 mins at 100C to remove any excess water or methanol.
3) The substrate is then placed into a chip package and bonded using a wire-bonder.

It is important to note that this step cannot be performed after the wire bonding is complete because it requires immersion into methanol, which is a solvent that would affect the adhesion of the substrate to the chip package due to interaction of the methanol with the conductive silver paint. In section 5.4.1, the presence of

the linker molecule is verified chemically to show that functionalization is stable and robust and unaffected by further processing steps (like the bonding).

5.2.2 Device Layout and Measurement Set-up

As enumerated in detail in section 5.2.1, functionalization of the graphene surface is required to be able to sense the protein PCT. The linker molecule PBASE that is required to adhere to the graphene surface is a large pyrene moiety. Studies have shown that the distribution of pyrene functionalized on graphene is uniform across the sheet. However, the molecules that are required to bind to the linker such as the antibody and the protein are large molecules and can have a shielding effect and passivate the surface hindering recognition binding events from taking place, therefore suppressing a signal. In order to counteract this, the device was designed such that a large surface-area of graphene will allow for multiple binding sites. Here, a large area graphene sheet on SiO_2/Si is contacted using a hall-bar type arrangement of metal contacts. Four voltage probes on either side of the sheet (L1, L2, L3, L4 on the left and R1, R2, R3, R4 on the right) are designed so as to measure fluctuations of the conductance in the channel in different sections of the graphene sheet in response to the addition of an analyte

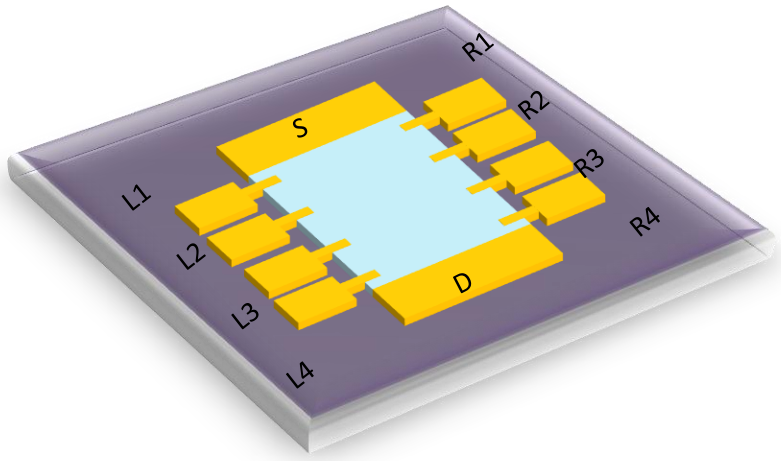

Figure 5.3: A Schematic of the hall bar arrangement of contacts on a large area graphene sheet.

The total dimensions of the graphene sheet are 4585 µm width and 4990 µm in length. The distance between the source and drain contacts is 4660 µm and the separation between the voltage probes are designed to be 1140 µm apart. Many devices were fabricated in order to arrive at the correct configuration of device layout and during the intial stages of measuring the sensor response. In this work, for the measurements described in section 6.3, a total of 4 devices were used. They are referred to S1, S2, S3 and S4. To carry out electrical measurements, the substrate is bonded to a 44-pin commercially procured 1cmx1cm chip package using a wire-bonder. The chip package is then slotted into a custom-built substrate holder that is pre-wired and connected to a 22 pin port which can be easily interfaced with a standard D-connector. The substrate holder was designed such that it could be used for room temperature measurements as well as for low temperature measurements by interfacing directly with a liquid helium dipstick that could be immersed directly into a liquid helium dewar.

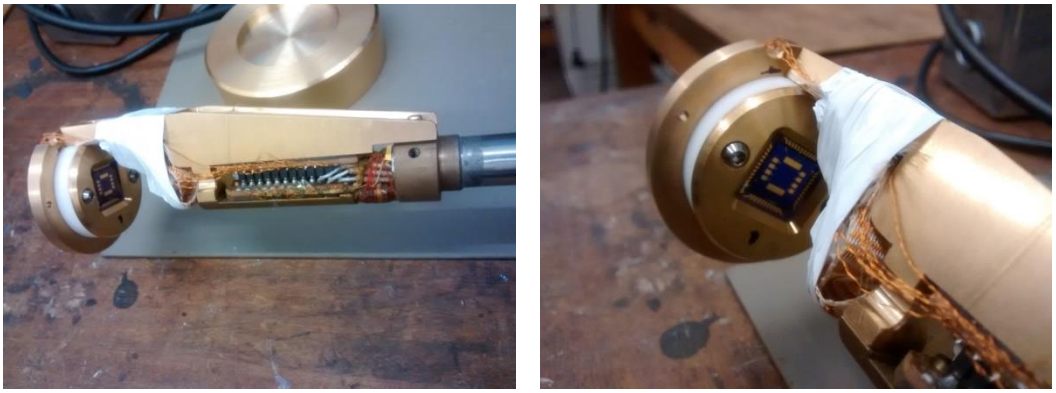

Figure 5.4: Substrate holder for the chip package Left: Side view showing wired connections to a port that is interfaced with a dipstick for low temperature measurements. Right : Top view showing the device architecture.

The drain contact pad on the graphene channel is connected to the oscillator of the lock-in amplifier, which acts as a voltage source. The source of the graphene channel connected to the ground terminal and the back gate is connected using silver conductive paint to the gate pin in the chip carrier which is controlled by a Keithley 2400 sourcemeter. The voltage probes are connected to the A and B

connections on the Lock-In Amplifier which give a readout of the potential difference across the two contacts. The lock-in amplifier and the Keithley 2400 are both interfaced to a computer using digital ports and a software called CryoMeas is used to control the instrumentation and record and store the data.

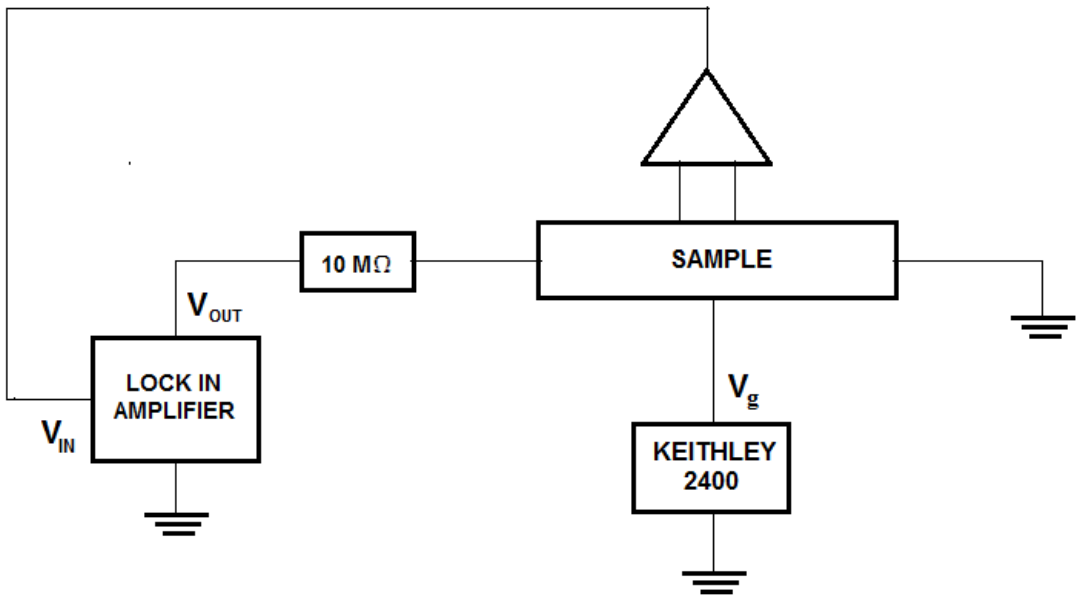

Figure 5.5: A Schematic Diagram of the circuit used to measure the I-V_g characteristics of the device.

The voltage across the source and drain is set at 1V. Through a large resistor placed in series with the graphene channel (10M Ohm), a constant current (10^{-7} A) is kept flowing through the channel. The R-V_g characteristics of the graphene sheet (between source and drain) as well as each individual set of voltage probes are measured using the circuit configuration as depicted in Figure 5.5. to give a baseline measurement for the resistance of the whole graphene sheet as well as different sections of the graphene sheet before any analyte is introduced.

The electrical measurement of response to an analyte was carried out by using a carefully calibrated micropipette to position a 2 µL drop of the desired analyte

onto a section of the graphene sheet between two voltage probes (for instance, in the region between L3 and L4) during which the R-T response is measured. Before the next measurement is made, the sample is characterized again used R-V_g sweep to get the new baseline for the resistance, measure any shift in the R-V_g characteristics and to ensure the sample is stable and any changes in the resistance that will be measured are a result of the analyte, and not due to any other factors.

5.2.3 Reagents Utilized

Several reagents were required to perform this experiment. PBASE was used to functionalise the graphene. A carbonate bi-carbonate (CBB) (of 7.7 μg mL^{-1}) buffer was made up to a pH = 9.2 which is required for the binding of the Anti-PCT antibody to the PBASE molecule. The antibody solution was made by diluting the as received antibody into the CBB solution. A phosphate buffer solution (PBS) made upto pH=7.4 (5 μg mL^{-1}), required for the binding of PCT to the antibody, was then used to make 4 different solutions of procalcitonin of 50ng/L (PCT1), 100ng/L (PCT2), 500 ng/L (PCT3) and 1000 ng/L (PCT4).

Graphene was purchased from Graphene Supermarket (CVD graphene transferred on 1cmx1cm 285nm SiO_2/Si substrate). Monoclonal anti-human procalcitonin capture antibody (clone 42) was purchased from 2BScientific Ltd and Human Procalcitonin (PCT) was purchased from ProSpec-Tany Technogene Ltd. To make up the carbonate-bicarbonate buffer, sodium carbonate (≥ 99.5% pure), sodium bicarbonate (≥ 99.7% pure) were procured from Fischer Scientific. Phosphate-buffered saline solution was purchased from Sigma Aldrich, pH = 7.4 with NaCl = 0.137 M and KCl = 0.0027M and 1-pyrenebutanoic acid succinimidyl ester (PYSE, 95%), methanol, potassium chloride (KCl, ≥ 99.0%) were purchased from Sigma-Aldrich and used as received. Alll aqueous solutions were prepared using ultra-pure DI water.

5.3 Results and Discussion

Surface potential for a FET Channel can change due to the presence of charged species near the surface of the channel. The device conductance of a FET channel will be modulated by the introduction of such species. Conductance modulation is especially useful for the detection of analytes with a net charge on them, or where the molecule is large and has charged groups such that their 3D molecular charge distribution can affect the surface charge density of the graphene sheet, and for analytes that transfer charge (reduction or oxidation reactions) in binding to the linker. This method has been shown already as an effective sensing mechanism for bioanalytes including DNA. In this work, this technique is utilized to sense the binding of proteins to linker FET-based detection of several molecules attached to the graphene surface.

5.3.1 Verification of Functionalization of Graphene Sheet

The functionalization of graphene with PBASE molecule needs to be verified to prove that the linker molecule is still attached to the graphene substrate after all the processing is complete. The graphene device is fabricated and functionalized with PBASE using the steps described in Section 6.2. The sample was then left for two days in an airtight petri-dish in a cleanroom environment. Subsequently, the sample was immersed in a solution of Horse Radish Peroxidase (HRP) in a pH = 9.2 CBB solution (5 μg/mL) for 20 mins. This is a molecule that is known to bind to the PBASE if present. The HRP can then be detected by reacting it with a molecule known as *o*-phenylenediamine dihydrochloride (OPD). The OPD is dissolved in a colourless pH=5 phosphate citrate buffer solution and the substrate containing the graphene+PBASE+HRP is immersed in the solution. If HRP is present, a yellow colour appears. This indicates the presence of PBASE as well, because HRP does not bind to graphene without the presence of the linker. Figure 5.6 shows a photograph taken of a sample after immersion in OPD

Figure 5.6: A photograph taken 1 minute after HRP-PBASE functionalized graphene is immersed in an OPD solution with Phosphate citrate buffer. The colourless solution turned yellow.

5.3.2 Electrical Characterization of the Graphene Sample

The electrical characteristics of graphene FET devices are typically studied by measuring resistance as a function of gate voltage V_g. The R-V_g curves for all four devices as measured immediately after fabrication are shown in Figure 5.7 a, b, c, d. At room temperature, the highest values of V_g that were accessible was about 30 V. In this window, the resistance showed an almost linear correlation to the gate voltage, which indicated the samples were heavily p-doped. In order to be able to identify the Dirac point V_D , the samples needed to be swept to increasingly larger gate voltages. At room temperature, for applied gate voltage of V_g = 30V and greater, the samples exhibited a leakage current through the gate. Therefore, low temperature measurements of R-V_g were required to be able to access the R- V_g characteristics for large values of gate voltages.

Figure 5.7 shows the R-V_g measurement between the top right contacts (R1 and R2) for the four samples that were measured. The samples were immersed into a liquid helium dewar with the temperature T = 4.2 K. It is evident from the graphs that the graphene sheet in all samples was very heavily p-doped and the Dirac point for samples S1,S2,S3 lie between 137V and 139V. However, S4 was even more heavily p-doped and the dirac point was found to be at 180 V.

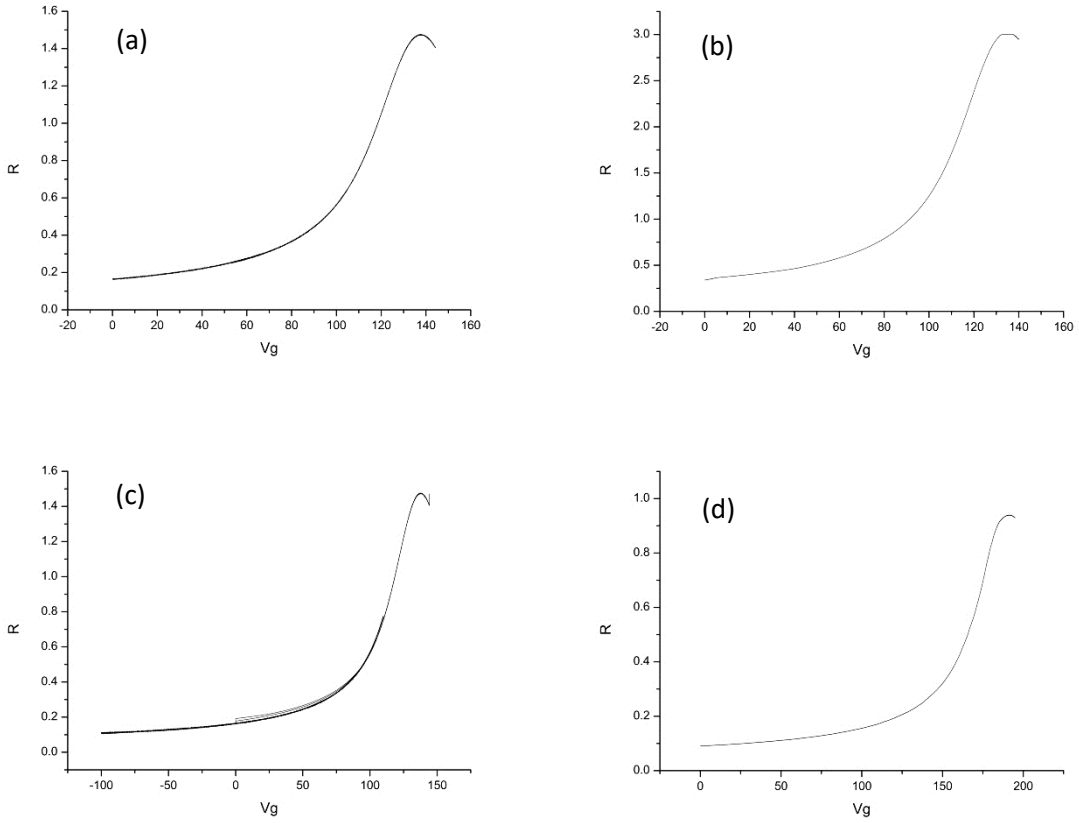

Figure 5.7: R-V_g curves for the 4 samples S1-S4, (R is measured as kΩ and V_g in volts) taken at T=4.2K and V_{SD} = 1V **a)** For S1, V_D = 137.59 V **b)** For s2, V_D = 137.783 V **c)** For s3, V_D =138.12 V and **d)** For S4, V_D = 180.12 V

Several studies including J.Ping et al and Zhou et al have shown that by comparing the R-V_g characteristics before and after the introduction of an analyte, relative shifts in Dirac point voltage can be used as an indicator of the binding event that has taken place. [9][24] In the case of these measurements however, owing to the heavy p-doping of the sample, it was impossible to access the Dirac point at room temperature. Therefore, the observing the shift in transfer curves or R-V_g curves could not be used reliably as an electronic sensing method.

5.3.3. Resistance-Time measurements

To achieve a dynamic response to the addition of an analyte, several groups have shown that measuring the drain current I_{ds}, resistance or conductance as a function of time is a useful technique. The resistance response of a FET-based sensor is affected by two factors: First, the electrostatic interaction between the charge of the biomolecule, and its effect on the surface charge density of the FET channel, this is the response that the experiment seeks to highlight and second, the counterions in the buffer, with channel, which may cause screening effects due to the formation of a passivation layer. This effect is expected to suppress the signal. In this work, instantaneous changes in Resistance are correlated to the introduction of specific analytes. Counterions build up which could cause screening effect was addressed by refreshing the graphene surface by repeated 'rinsing' in DI water. Effectively, in experimental conditions this meant that after every charged analyte was introduced, 3 drops of DI water were successively added and suctioned off to remove an excess build up of ions.

5.3.3.1 Response to DI Water and drop evaporation/drying

As described in Section 5.2, to study the response of the channel to the analyte, a 2 µL drop of analyte is position onto the surface of the graphene sheet such that drop lies exactly between the two voltage probes. Figure 5.7 shows a typical Resistance change that is observed on the introduction of the DI water drop. The blue arrows correspond to the drop in resistance that is repeatably observed every time a drop of DI water is introduced on to the channel. The drop in resistance corresponds to between 1.5% - 2.5 % in resistance. Shortly after the drop makes contact, owing to the small volume of the drop, the resistance of the channel gradually begins to increase as the drop begins to evaporate, as shown by the yellow arrows. If the drop is dried off or suctioned off, then resistance increases in a step-like manner as indicated green arrow. This behaviour was observed in every experiment that was performed, because DI water droplets were repeatedly introduced and suctioned off, after every analyte response was measured to help remove a build of ions and refresh the region of the graphene channel that was being measured.

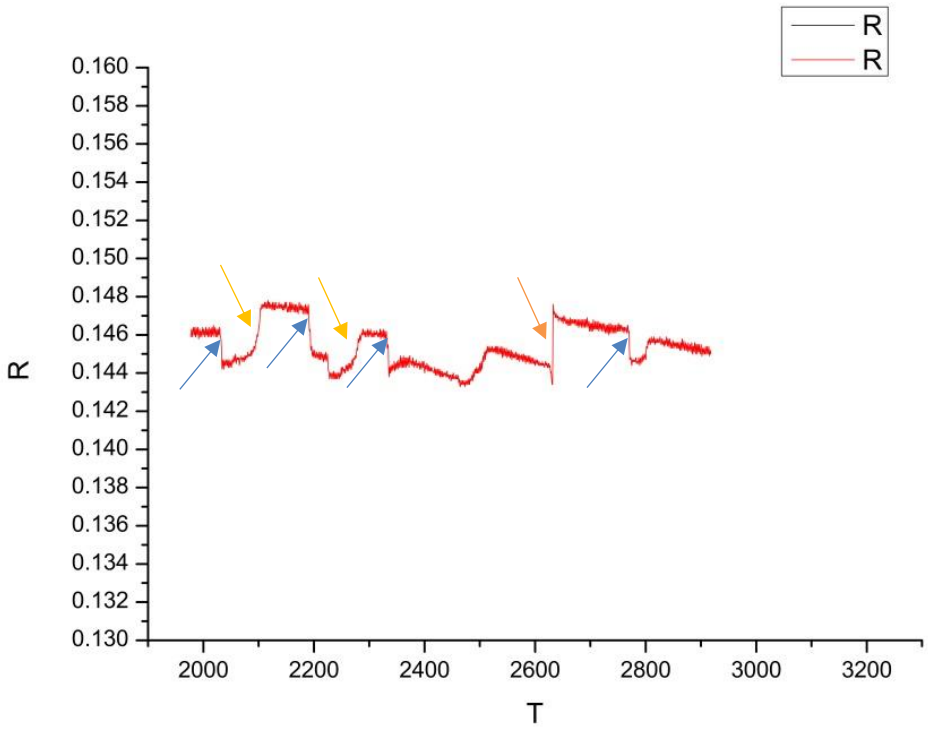

Figure 5.8: R-T response (measured as kΩ and seconds resp.) to addition and removal of a drop of water on the FET channel. Applied V_g = 20V. Blue arrows indicate addition of a droplet of water onto the channel. The yellow and green arrows indicate gradual drying and drying with N_2 gun respectively.

5.3.3.2 Response to Buffer Solutions

Two different Buffer solutions are used in these experiments, and they correspond to the pH required for the binding events of the Antibody and the PCT. Both buffer solutions are alkaline (CBB=9.2 and PBS =7.4) and add charged ions to the graphene surface causing an increase in resistance. The first step in the experiment requires the binding of antibody to the PBASE linker molecule. The antibody drop is added to a fresh sample between L3 and L4 probes and the response is recorded. A control drop of CBB solution is added to another region of the R3 and R4 and the response is recorded. The order is then reversed where the CBB solution is added to a fresh sample first between L3 and L4 and then an AB solution is added between R3 and R4. Figure 5.9 shows the R-T response in both cases.

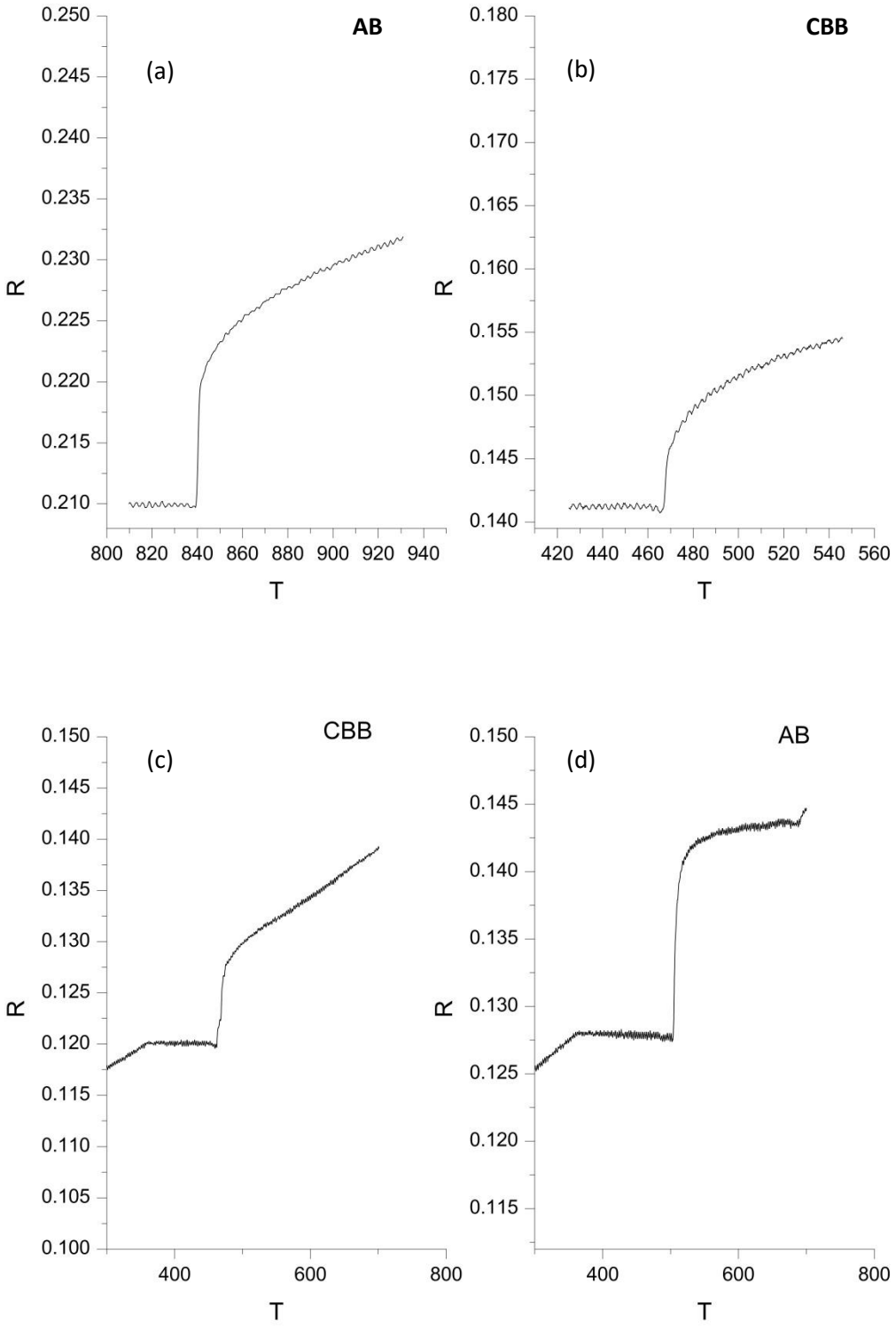

Figure 5.9: R-T response (measured as kΩ and seconds resp.) for (a) The addition of AB between L3 and L4 – ΔR = 8.4 % (b) The addition of CBB solution to R3 and R4 of the sample test sample TS1. ΔR = 4.2 % (c) and (d) correspond to the reverse process where CBB was added to L3 and L4 (ΔR = 6.4 %) and AB was then added to R3 and R4 (ΔR = 12.1 %).

By observing the % increase in resistance in the case of AB solution, an increased response to AB solution is indicated. Additionally,the shape of the resistance curve differentiates the AB solution from the CBB solution. This result can be explained by the fact that when antibody binds to the graphene surface, the surface charge density would increase over and above that which is produced by just the ions in the buffer solution. The binding of the antibody was also further verified by using the chemical means described in section 5.3.1, where a test sample with a graphene sheet was incubated in AB solution (5 mins), followed by HRP solution (20mins) and then tested with OPD for the presence of yellow colour.

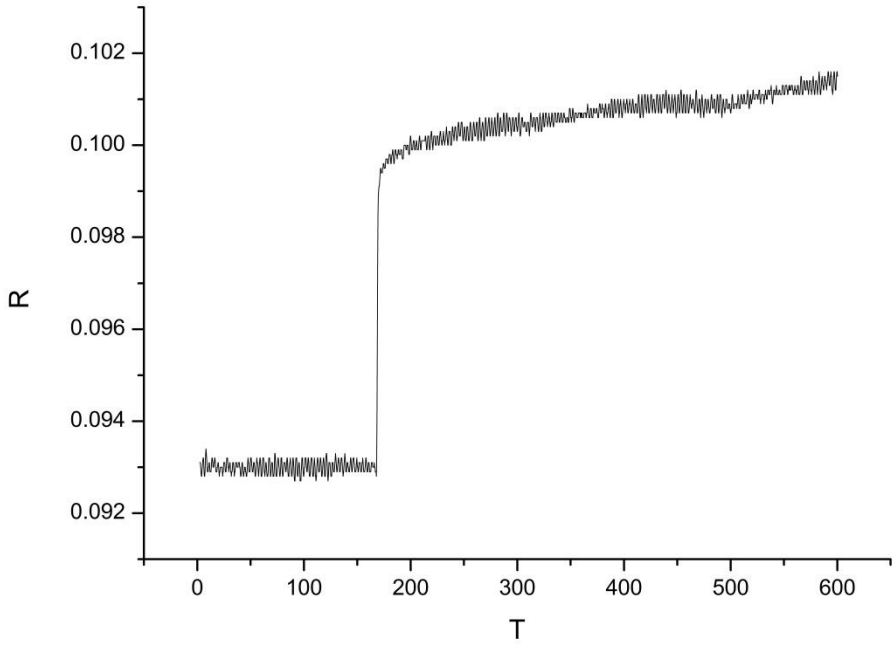

Figure 5.10: R-T response (measured as kΩ and seconds resp.) for the addition of 2μL drop of 0.01M PBS solution between L3 and L4 of test sample TS3. ΔR = 6.8 %

The R-T response to the addition of a drop of PBS solution on a test sample is shown in Figure 5.10. It shows a small and sharp increase in the resistance which increases gradually as the drop dries up. The R-T response of a PCT solution on a bare substrate shows identical behavior to PBS solution. This is

because of the absence of the antibody where it can bind. In this case, the large protein molecule is unable to interact with the linker molecules and is shielded from interaction with the graphene surface by the large linker molecules as well as the electrolyte ions, unless it binds to the protein molecule. This is confirmed by the addition of PCT solution on a bare substrate, as well as recording the response to the PCT after the addition of a CBB buffer (with no attached Antibody) in Figure 5.10.

Furthermore, the R-T response to PBS is further verified by the addition of a drop of PBS solution to a sample after the antibody has been binded to it. Figure 5.11 reveals an expected small increase in resistance on addition of PCT in PBS which is in contrast to the response to PCT after antibody binding has taken place as shown in Figure 5.15.

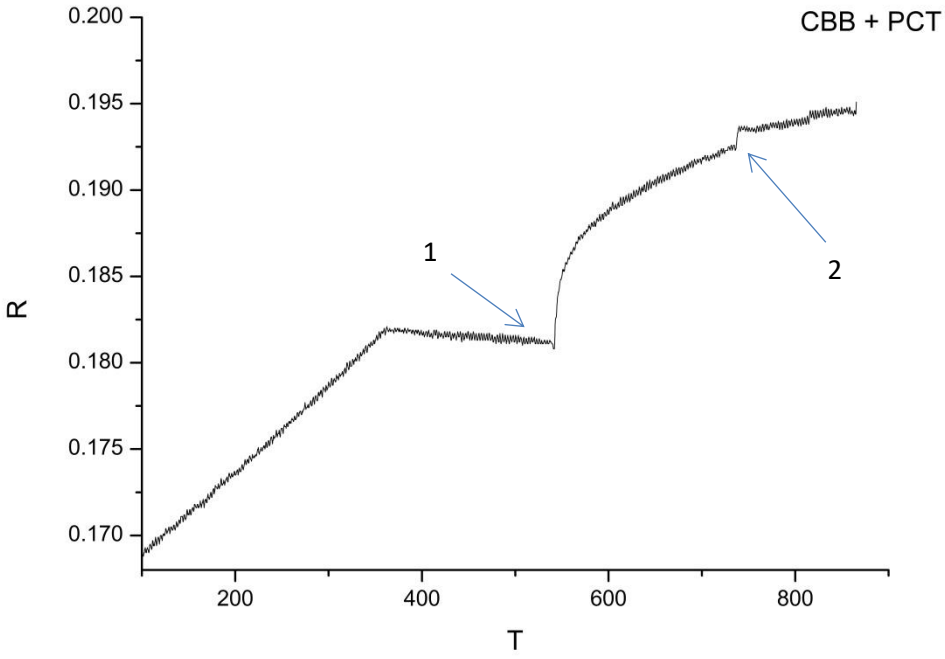

Figure 5.11: R-T response (measured as kΩ and seconds) for the addition of (1) CBB Solution (ΔR = 3.91 %) followed by (2) addition of PCT solution between L2 and L3 of test sample TS2 (ΔR < 1 %)

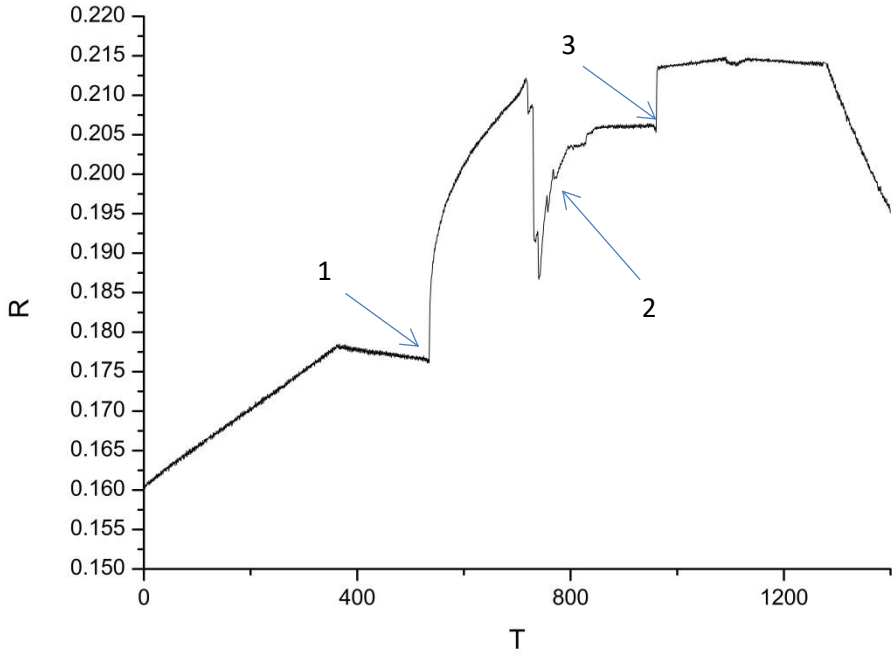

Figure 5.12: R-T response (measured as kΩ and seconds resp.) for the addition of (1) AB solution (ΔR = 16.6 %) followed by (2) the successive addition and removal of DI 3 Water drops (ΔR = 8.1%) and (3) addition of PBS solution between L1 and L2 of test sample TS1 (ΔR = 4.91 %)

5.3.3. Response to PCT

The electrical response to the binding of PCT molecule to the Antibody is the final step in the development of the sensor. As seen in the previous section, the introduction of PCT in the absence of the antibody does not yield a significant increase in resistance and the resistance change closely mimics the response to a drop of PBS solution in contact with the graphene sheet.

Figure 5.13 illustrates the response on Sample S1, where the gate voltage is V_g = 0V. A drop of AB solution is first added to the sample (1) and allowed to bind to the linker molecule for 2 mins. The excess liquid is suctioned off (2) and DI water is added to the region to refresh the channel and remove excess ions (3). A drop of PCT is then added to the channel (4) and the resistance increase that is recorded is order of magnitude larger than the response for PCT on a bare substrate or on a substrate with no antibody attached.

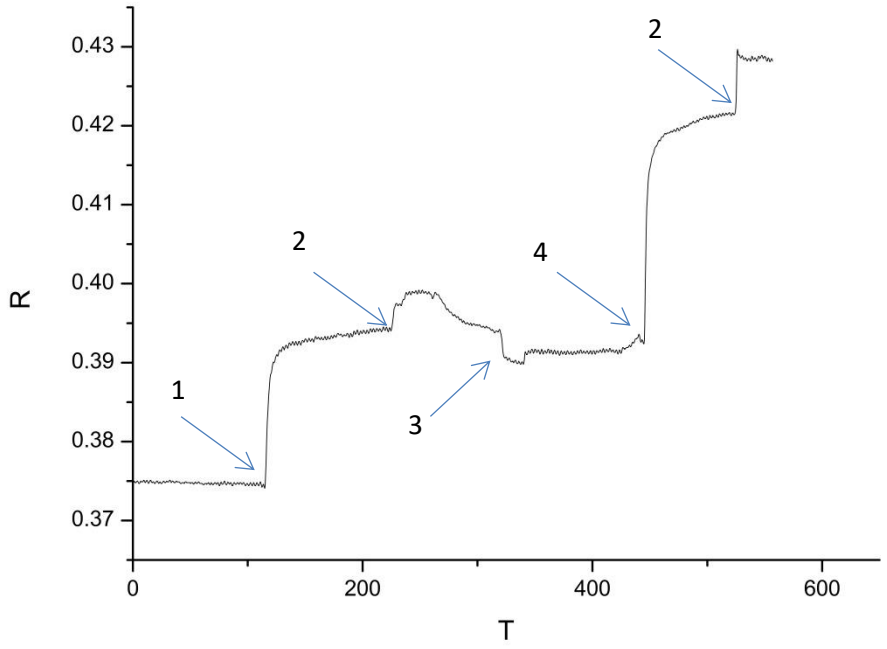

Figure 5.13: R-T response (measured as kΩ and seconds resp.) for the addition of (1) AB Solution (ΔR = 4.56 %) followed by (2) removal of excess liquid (3) addition of DI Water drop and (4) addition of PCT 1 solution (ΔR = 5.9 %) between L1 and L2 of sample S1

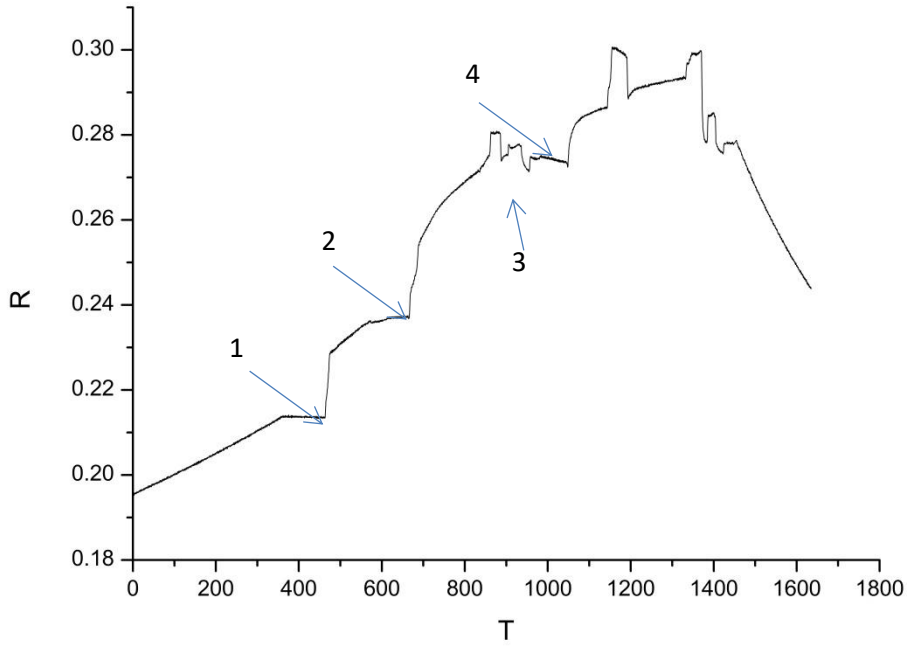

Figure 5.14: R-T response (measured as kΩ and seconds resp.) for the (1) addition of CBB solution (ΔR = 8.1 %) followed by (2) addition of AB solution (ΔR = 10.9 %) (3) removal of excess liquid and refreshing the surface with DI Water and (4) addition of PCT 2 solution (ΔR = 8.4%) between R3 and R4 of sample 2.

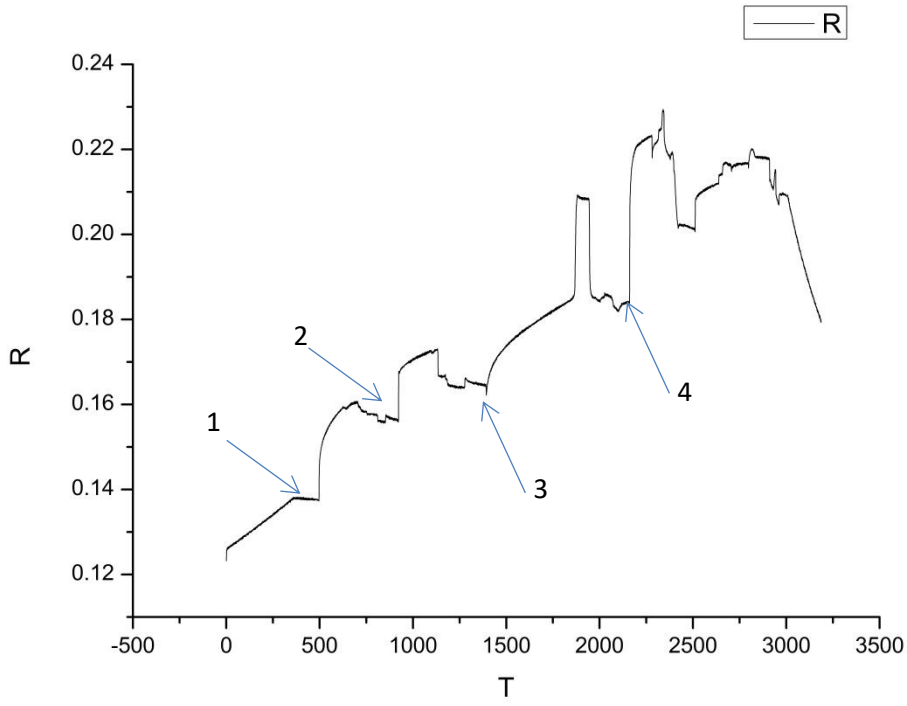

Figure 5.15: R-T response (measured as kΩ and secs resp.) for (1) addition of AB Solution (ΔR = 12.9 %) followed by (2) addition of PCT 1 soln (ΔR = 7.9 %) (3) addition of AB soln. and refreshing surface (4) addition of PCT 3 (ΔR = 13.9 %) solution between L3 and L4 of sample 3

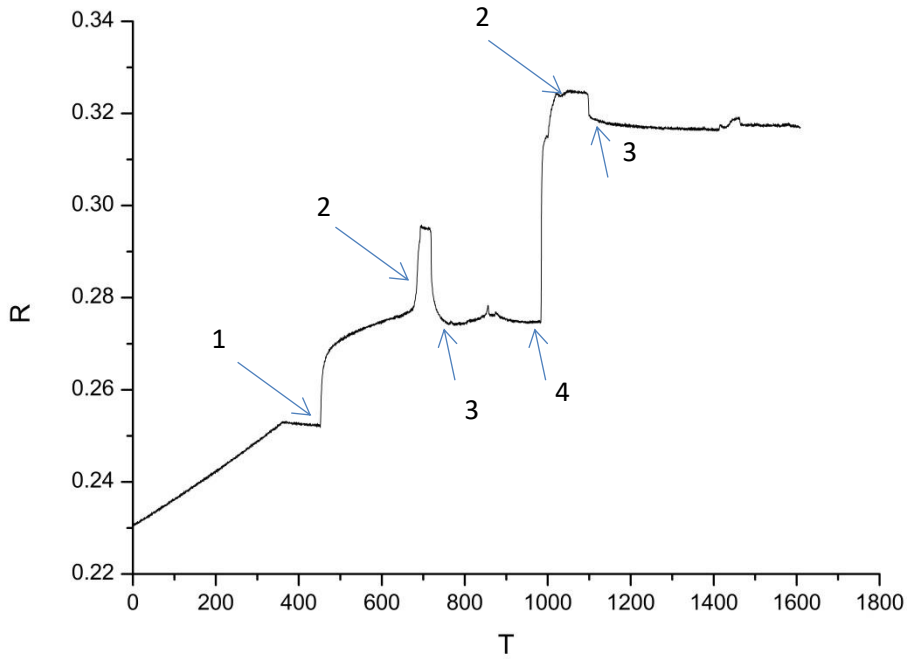

Figure 5.16: R-T response (measured as kΩ and seconds resp.) for the (1) addition of AB Solution (ΔR = 9.1%) followed by (2) removal of excess liquid (3) refreshing the surface with DI Water and (4) addition of PCT 4 solution (ΔR = 15.9 %) between R1 and R2 of sample S4

Observing the ΔR in figures 5.13 -5.16 suggests that the resistance in the graphene channel is modulated by the introduction of AB as well as PCT. In every sample, the response to PCT in terms of percentage increase in resistance was consistently higher than for AB (and significantly higher than for plain buffer solutions). Additionally, in figure 5.15, two different concentrations of PCT solution are introduced to examine whether the graphene surface is still sensitive to another drop of PCT with higher concentration. And from the experiments, we were able to see that it was. After the surface was exposed to PCT1, it was refreshed using DI water and suctioning it twice. This addressed the build-up of excess ionic species on the graphene surface, and it was made sensitive again to the target analyte. Therefore, on introducing PCT 3, the sample showed an appropriately higher percentage increase in resistance. This suggests that the mechanism for interaction with graphene surface that is causing the increased resistance is likely due to more than just a build-up of charge, but in all likelihood, an indication of binding of PCT to available binding sites.

5.3.3.4 Variation of PCT Concentration

In section 5.3.3.3, it is shown that the graphene-based FET channel is able to sense the binding of Antibody and PCT molecules to the substrate. However, sensitivity to variation in the concentration is also another pre-requisite to building a sensor. In Figure 5.17, the values of ΔR, the increase the resistance, are correlated to the concentration of the PCT used for measurements in four samples S1-S4. In all four samples, the graphene channel responds with larger changes in resistance for larger concentrations of the target analyte. From this data, we can calculate the limit of detection (LOD) for PCT detection. It should be noted, that due to the small number of samples, as well as only different concentrations of PCT, the calculated LOD may in reality be different. For these samples, the LOD was found to be 66.94 ng/L and the sensitivity of the device was found to be 8×10^{-5} kΩL/ng. Additionally, although this graph indicates that the increase in resistance is dependent on the PCT concentration, calibration of the device characteristics with the concentration will require greater precision of

measurement as well as the ability to be able to measure shifts in the Dirac point at room temperature, which is not possible with this device geometry and these samples.

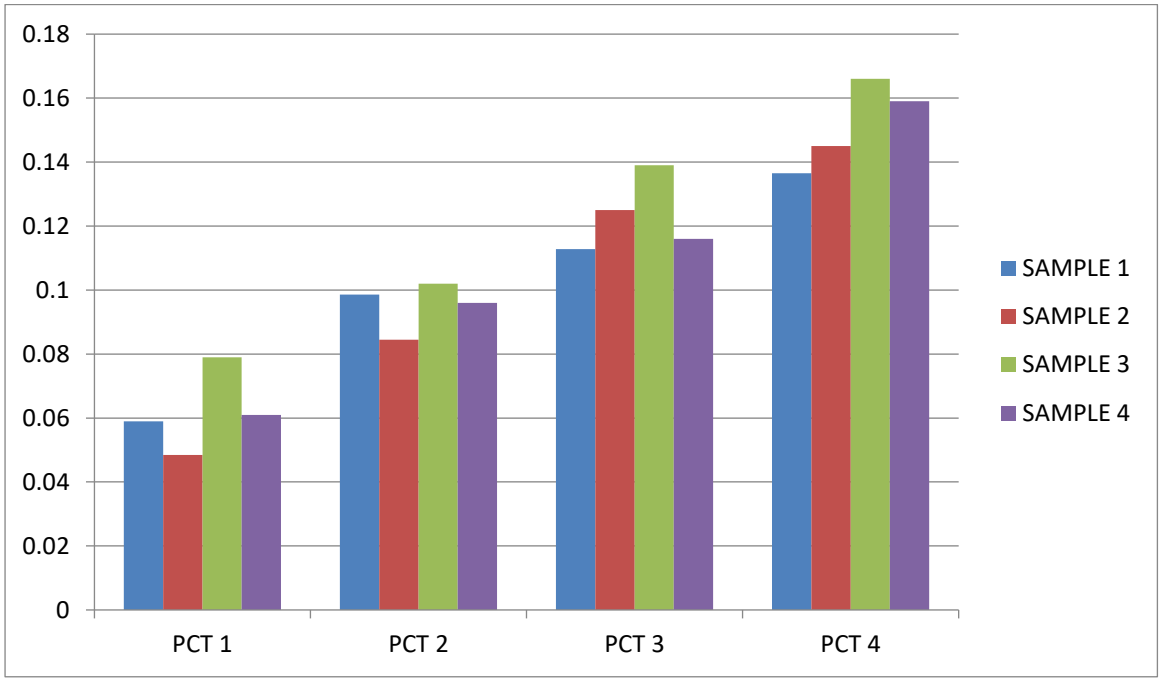

Figure 5.17: A bar graph correlating the percentage ΔR shift from R-T measurements for four samples S1-S4 using 4 different concentrations of PCT 1-4.

The Debye length is a factor that can affect detection limits and sensitivity. In ionic mediums such as PBS which are required to sustain the activity of a protein, the Debye length tends to be quite small. For instance, 1M PBS solution has a DL nearing 0.7 nm, which is much smaller than the size of a regular antibody (5~10 nm). Therefore, to sensitively detect proteins through a linker molecule on a FET, the electrical measurements are made in more dilute solutions such as 0.01 PBS as in these measurements, such that the Debye length is larger (7.4 nm). In these experiments, due to the stacked structure, it is likely to have an effect on the direct screening of charge to the graphene surface. Therefore, one possibility to explain the modulation of graphene's resistance would be to verify that the binding event is able to directly transfer charge through the stacked structure. More experiments need

to be performed to understand the mechanism and this aspect of the sensing platform.

5.4 Conclusion

The measurements as described in section 5.3 offer a proof of concept detection for the presence of a biomarker for Sepsis. It is shown that the graphene-based FET device was able to sense the presence of the Anti-PCT antibody and differentiate from its buffer solution. Furthermore, the device was able to support a second binding event, where PCT attached to the Antibody and caused a measurable increase in the resistance. The limit of detection for the given samples and concentrations tested was found to be be 66.94 ng/L and the sensitivity of the detection was found to be $8x10^{-5}$ kΩL/ng. The resistance increases were correlated with the concentration of the PCT solutions used.

The sensor combines the exceptional electrical properties of graphene which when functionalized offers an interesting sensing platform for the electronic detection of PCT and offers a new route for diagnosis of Sepsis in real time measurements.

Further work is needed to achieve greater control over the electrical measurement characteristics, quantify the specificity and sensitivity, as well as understand the mechanisms affecting the sensing of PCT. Exploring alternate devices geometries such as arrays of graphene FET channels would offer the advantage of multiple binding sites, because the cumulative area of the graphene would be large, as well as offering greater control over the device characteristics. Most importantly, the ability to measure dirac point shifts at room temperature would lead to the possibility of calibrating the sensor for the concentration of analyte solution.

5.5 Bibliography

1. Numan Celik , Wamadeva Balachandran, Nadarajah Manivannan IET Circuits Devices Syst., pp. 1–12
2. Karolina Z. Milowska and Jacek A. Majewski *J. Phys. Chem. C*, 2014, 118 (31), pp 17395–17401
3. Weiss, N.O., Zhou, H., Liao, L. et al. Adv. Mater., 2012, 24, (43), pp. 5782–5825
4. Balandin, A.A., Ghosh, S., Bao, W., et al Nano Lett., 2008, 8, (3), pp. 902–907
5. Novoselov, K.S., Geim, A.K., Morozov, S.V., et al , Science, 2004, 306, (5696), pp. 666–669
6. Ana Carolina Mazarin de Moraes and Lauro Tatsuo Kubota Chemosensors 2016, 4, 20,
7. N C S Vieira1,3, J Borme1, G Machado Jr1, F Cerqueira2, P P Freitas1,V Zucolotto3, N M R Peres2 and P Alpuim1,2J. Phys.: Condens. Matter 28 (2016) 085302 (9pp)
8. Sowmya Viswanathan1, Tharangattu N. Narayanan, Kiana Aran, Kathryn D. Fink, Jacobo Paredes, Pulickel M. Ajayan4, Slawomir Filipek5, Przemyslaw Miszta, H. Cumhur Tekin, Fatih Inci, Utkan Demirci, Pingzuo Li, Kirill I. Bolotin, Dorian Liepmann and V. Renugopalakrishanan Materials Today Volume 18, Number 9 November 2015
9. Ning Gaoa,1, Teng Gaoa,1, Xiao Yanga, Xiaochuan Daia, Wei Zhoua, Anqi Zhanga, and Charles M. Liebera,b,2PNAS | December 20, 2016 | vol. 113 | no. 51 | 14633–14638
10. Hugo Pinto and Alexander Markevich Beilstein J Nanotechnol. 2014, 5: 1842–1848.
11. T. Kuila et al , Biosensors and Bioelectronics 26 (2011) 4637– 4648
12. Ohno, Y., Maehashi, K., Yamashiro, Y., Matsumoto, K. Nano Lett. 2009, 9, 3318–3322.

13. X. H. Kang, J. Wang, H. Wu, A. I. Aksay, J. Liu, Y. H. Lin, Biosens. Bioelectron. 2009, 25, 901
14. Dong, X., Shi, Y., Huang, W., Chen, P., Li, L.P. Adv. Mater. 2010, 22, 1–5.
15. Yinxi Huang,Xiaochen Dong,Yumeng Shi,Chang Ming Li,Lain-Jong Li Peng Chen Nanoscale, 2010, 2, 1485– 1488
16. Jayeeta Basu and Chirasree RoyChaudhuri Sensors 2016, 16, 1481, doi:10.3390/s16101481
17. Mengmei Cao,, Aiping Fu Zonghua Wang,Jingquan Liu,Na Kong,Xidan Zong, Huihui Liu, and J. Justin Gooding J. Phys. Chem. C 2014, 118, 2650−2659
18. Liping Chen, Linjun Wang, Zhigang Shuai, and David Beljonne J. Phys. Chem. Lett. 2013, 4, 2158−2165
19. Vasilios Georgakilas, Jitendra N. Tiwari, K. Christian Kemp, Jason A. Perman, Athanasios B. Bourlinos, Kwang S. Kim,and Radek Zboril*,§Material Chem. Rev. 2016, 116, 5464−5519
20. Dianping Tanga,Qunfang Li,Juan Tanga,Biling Sua,Guonan Chen, Analytica Chimica Acta 686 (2011) 144–149
21. C. Pierrakos and J.-L. Vincent, "Sepsis biomarkers: a review.,Crit. Care, vol. 14, no. 1, p. R15, 2010
22. L. S. a. Mahe, S. J. Green, C. P. Winlove, and a. T. a. Jenkins, J. Solid State Electrochem., vol. 18, no. 12, pp. 3245–3249, 2014.
23. D. K. Polyushkin, J. Milton, S. Santandrea, S. Russo, M. F. Craciun, S. J. Green, L. Mahe, C. P. Winolve, and W. L. Barnes, J. Opt., vol. 15, no. 11, p. 114001, 2013.
24. Guangfu Wua, Xin Tanga, M. Meyyappanb, King Wai Chiu Lai a, Applied Surface Science 425 (2017) 713–721
25. Jinglei Ping, Ramya Vishnubhotla, Amey Vrudhula, and A. T. Charlie Johnson, ACS Nano 2016, 10, 8700−8704

Chapter 6

Flow-Sensing with Graphene FET Arrays.

6.1 Introduction

Graphene has been shown to be an excellent material for developing sensors, with the combination of incredible electrical properties as well as an ease of functionalization that enables selectivity in detection of the desired analyte species. [1] Previous studies have demonstrated that the utilization of graphene FETs in sensor architectures provides high sensitivity due to the high surface to volume ratio, biocompatibility and highly conductive nature of these FETs. [2] and an array of medically important analytes have been specifically and sensitively detected using graphene-FET based sensors [1-3]. More recently, studies have emerged that focus on not just the proof-of-concept development of a sensor but developing devices that have the potential to be commercially realized, point of care device (POC). [2-4].

A POC device is one that provides a rapid response, that is inexpensive to fabricate and that is miniaturized, so as to be efficient and low power. It is also known as a lab-on-chip device as it enables immediate detection and quantification of a target analyte without the need for skilled personnel and the expense and time taken for conventional laboratory assays. [4] A POC device thus must have certain characteristics that allow for biological samples to be

used directly without preparation, such as blood or saliva. Microfluidic channels form an important component of such devices as they enable small volumes of liquids to be controlled, manipulated or processed and have been used extensively in field and home POC devices for volumes of fluid, such as blood, that are to be analysed [4-6] Therefore, combining the excellent sensor platform that graphene-based devices can provide with microfluidic channels opens up greater potential for graphene nano-electronic devices to be full realized as next-generation portable, low power, handheld POC devices for the timely detection of biomarkers indicative of serious illnesses and for the cost-effective diagnosis of diseases. Studies have demonstrated the use of microfluidic channels in tandem with graphene FET devices for the electrical detection of several analytes, including glucose and malaria-infected red blood cells [6][7] With this as motivation, a graphene FET array was developed and integrated with microfluidic channels. This chapter details the experiments performed towards realizing flow-sensing using graphene FETs. The chapter begins with an introduction, followed by section 6.2, that outlines the experimental methods that are used to make the measurements – namely, the device layout and the measurement set-up. Section 6.3 describes the results that were obtained from the measurement and demonstrates that the graphene FETs in the array can be individually measured as liquid is passed through the microfluidic channel, thus enabling greater control or dynamic, real-time sensing of changes in conductance of the graphene FETs. The chapter is concluded with an overview of the work done and suggestions for future directions of exploration.

6.2 Experimental Methods

The step-by-step fabrication of the graphene FETs using CVD graphene on a SiO_2/Si substrate has already been detailed extensively in Chapter 3. This section describes the experimental methods required for the measurement of the device starting with the device layout, the measurement set up and reagents

that were to study the electrical response of graphene to water droplets that were placed on its surface or in the vicinity.

6.2.1 Device Layout

One of the key steps towards realization of POC devices from a proof of concept sensor platform is the integration of microfluidic channels. Figure 6.1 shows a CAD design of the device layout, and a photograph of a fully fabricated device with 4 microfluidic channels embedded into a chip carrier. The graphene FET array is arranged into 4 groups that are labelled as Top Left (TL), Top Right (TR), Bottom Left(BL) and Bottom Right (BR). Each section consists of 4 graphene strips that are of the dimensions 625 µm in length and 100 µm in width and referred to as 1,2,3,4, such that the top most graphene strip on the left is labelled TL1, the bottom most strip on the right is BR4 etc. The spacing between consecutive strips is consistent at 235 µm. Each graphene strip is individually contacted and connects to larger metallic contact pads that serve as bonding pads for wire bonding, to connect the device to the chip carrier.

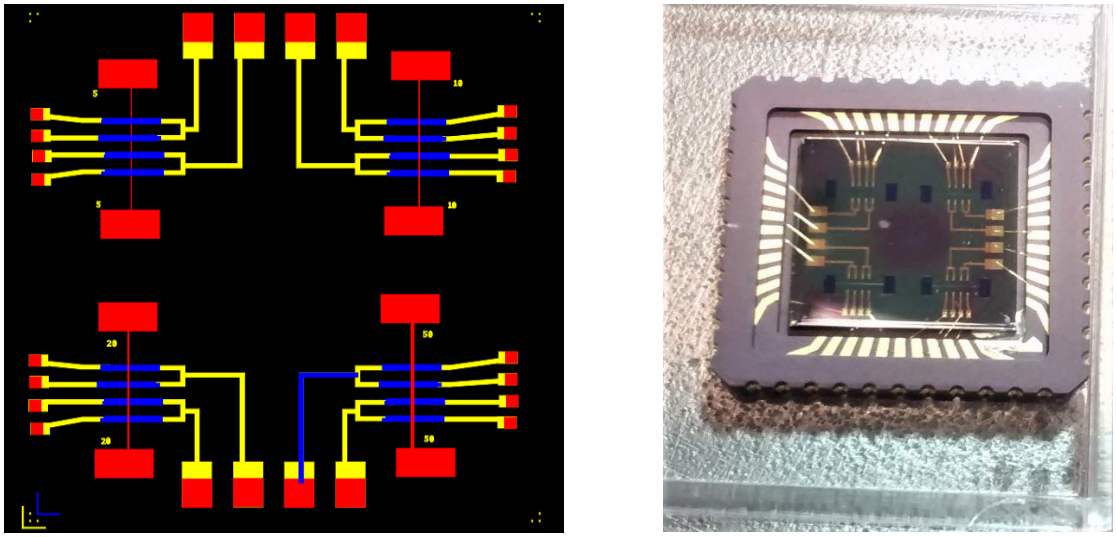

Figure 6.1: *Left:* A CAD schematic of the device layout. *Right:* A photo showing a fully fabricated and contacted device.

The microfluidic channels are fabricated into a thick resist layer on top of this structure and there are 4 channels of varying lengths, one 5 µm channel on the top left, two 20 µm channels top right and bottom left and a 50 µm channel over the bottom right array of graphene strips.

6.2.2 Measurement Setup

Several devices were fabricated in order to arrive at the correct configuration of device layout, especially during the fabrication stage, as well as during the initial stages of measuring the electrical response of the FETs. Some of these had to be discarded owing to leakage of the oxide layer, others due to broken contacts or small tears in the graphene channel that were not visible but discovered during measurement because the channel was found not to conduct. In this work, the measurements that are presented and discussed have been performed on 2 devices, which gives 4 arrays each that could be measured, yielding a total of 8 separate sets of measurements. The samples are referred to S1 and S2 respectively.

To carry out electrical measurements, the substrate was bonded to a 44-pin commercially procured 1cmx1cm chip package using a wire-bonder. The chip package was then slotted into a custom-built substrate holder that was pre-wired and connected to a 22-pin port which could be easily interfaced with a standard D-connector. The substrate holder was designed such that it could be used for room temperature measurements and to allow for a lab clamp stand with a micropipette attached can be positioned above it to drop liquid on to the substrate in the desired location.

In section 6.3, two types of measurements are described, the first set of measurements show the concurrent measurement using two or three separate lock-in amplifiers of 3 out of the 4 graphene strips in one array, as a response to the placement of a drop in its vicinity. Figure 6.2 shows the circuit diagram that is used in the case that three concurrent measurements were made. In this case, each graphene strip is contacted at either ends as source and drain contacts. The

source of the graphene strip is connected to ground and the drain is connected to the Oscillator output in the lock-in amplifier that acts as a voltage source. The back gate is connected using silver conductive paint to a Keithley 2400 source meter that provides a DC voltage. The A voltage probes from each lock-in amplifier is connected in parallel to the source of the corresponding graphene strip and measures the potential drop across the strip with respect to ground. The lock-in amplifier and the Keithley 2400 are both interfaced to a computer using digital ports and a software called CryoMeas is used to control the instrumentation and record and store the data.

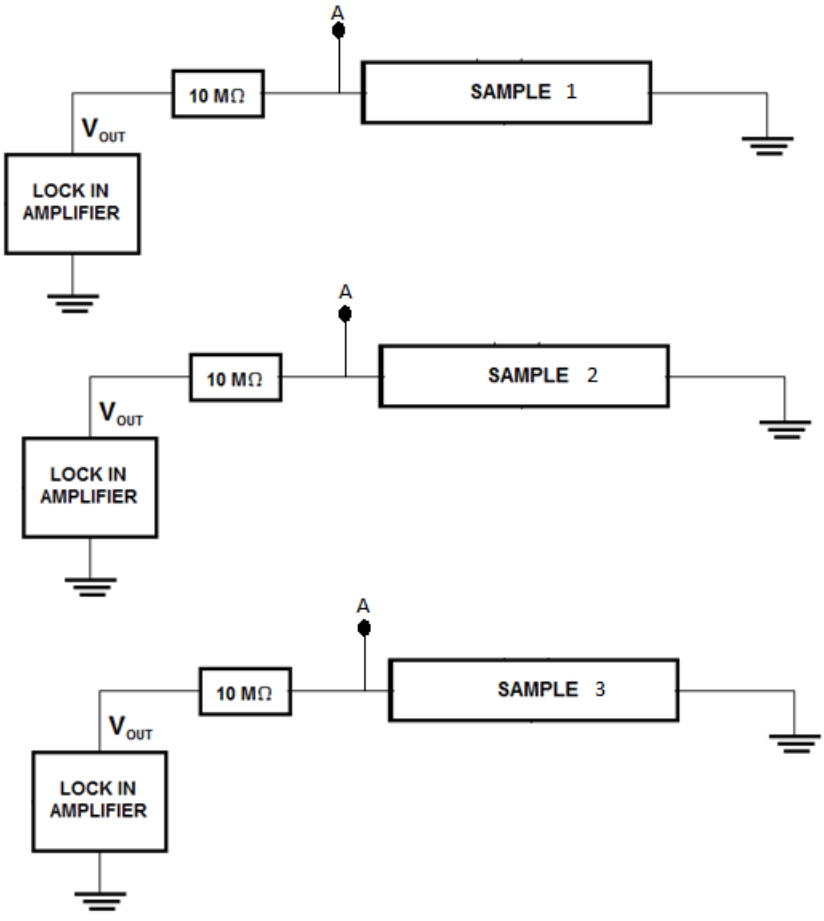

Figure 6.2: A Schematic Diagram of the circuit used to measure the Resistance as a function of time for 3 graphene strips simultaneously in the device.

The voltage across the source and drain is set at .1V. Through a large resistor placed in series with the graphene channel (10M Ohm), a constant current (10^{-8} A) is kept flowing through the channel. The R-T characteristics of the graphene sheet (between source and drain) in response to a droplet of DI water that is positioned on the device using a carefully calibrated micropipette to 2 µL. Before the next measurement is made, the sample is characterized again used R-V_g sweep to get the new baseline for the resistance, measure any shift in the R-V_g characteristics and to ensure the sample is stable and any changes in the resistance that will be measured are a result of the water, and not due to any other factors.

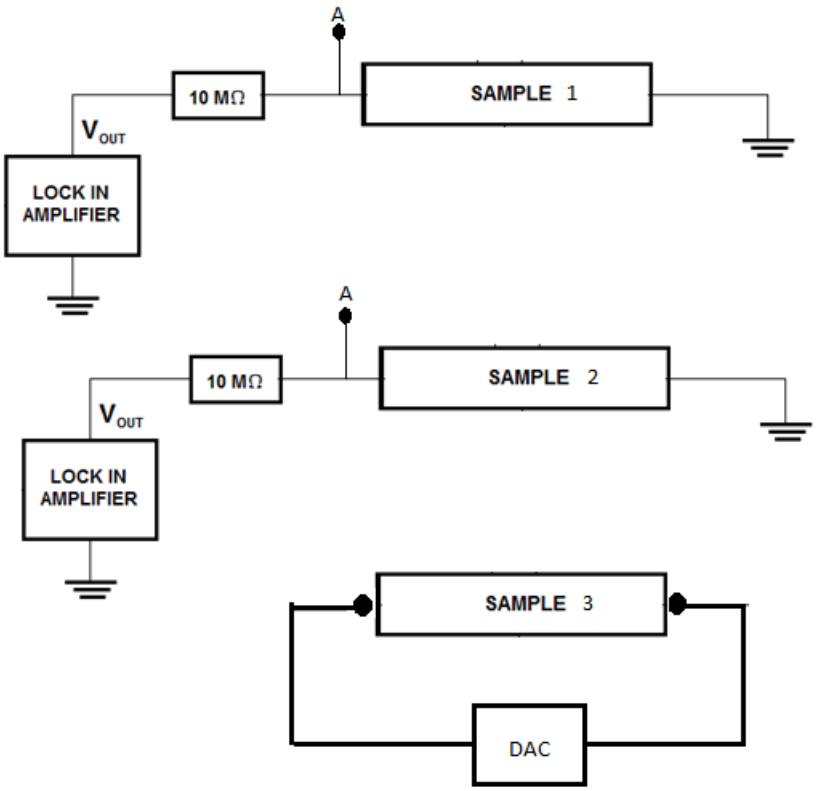

Figure 6.3: A Schematic Diagram of the circuit used to measure the R-T and R-V_{dc} for 2 graphene strips simultaneously in the device.

In section 6.3, the second set of measurements, a DC voltage is applied across one of the graphene strips in the order of 1-20V. The R-T and R-V_{dc} characteristics of the graphene strips in response to the addition of a droplet of DI water is then studied. In this case, each graphene strip is contacted at either ends as source and drain contacts. Figure 6.3 shows that the two graphene strips whose electrical response is to be measured are connected as in the previous set-up. The graphene strip that is used almost as a in-plane side gate and is connected to a DC voltage source using a DAC that is built-in to the Lock-in Amplifier. Both the lock-in amplifiers are interfaced to a computer using digital ports and a software called CryoMeas is used to control the instrumentation and record and store the data.

6.3 Results and Discussion

Surface potential for a FET Channel can change due to the presence of charged species near the surface of the channel. The device conductance of a FET channel is therefore being modulated by the introduction of such species. In this section we report on the experiments performed to understand the effect of water on the graphene FET channel, to ascertain if flow-type transport of water is taking place in the channel and whether that can be electronically sensed by the graphene FETs and finally, the effect of a DC voltage that is applied along one of the graphene FETs, which produces a static electric field that affects the device characteristics and produces some kind of modulation when the voltage is swept across a range.

6.3.1 Effect of water on Graphene FET channel

Understanding the effect of water on the electronic properties is extremely important for applications that involve the electrical response of a graphene channel in atmospheric conditions or in solution medium. Several studies have

investigated the effects of water vapour and humidity on the electrical characteristics of graphene. [4][6]. Indeed, humidity sensors and water vapour detection has been achieved with graphene nano-electronic devices. [11][12] Theoretical works have also studied the effect of graphene and water vapour and both experimental and theoretical works agree that the presence of water adsorbates on a graphene surface cause an electron-withdrawing effect, thus p-doping the graphene channel. [8-12] However, very few reports discuss the effect of macroscopic volumes of water on graphene's electrical properties. This may be because as Bollmann et al. report, the doping effects of a single layer of water has the largest p-doping effect, and after 5 layers, the doping effects of water are saturated [13] [14] A few other studies also refer to the possible diffusion of water through monolayer graphene to the SiO_2 substrate surface, that can cause doping as well as wrinkling and folding of the graphene sheet. [4] [15]

In this work however, because the graphene FET arrays are subjected to macroscopic drops of DI water in the microfluidic channels, it is necessary to establish a baseline for their effect on the graphene. This would also be of interest to any sensor application of graphene FETs that uses an aqueous solution medium. (as in Chapter 5). Therefore, the first measurements taken were with a view to characterize the sample and establish the electrical response to the placement of a standardized DI water droplet (2 µL) on the surface of the graphene. Figure 6.4 is a graph showing the resistance as a function of time. Here, a drop of DI water was placed directly on top of the graphene strip BL1 that was being measured and the RT response was recorded. The source-drain voltage is set at 0.1V, in series with a 10 MΩ resistor, such that the current is given as 10^{-7} A. It was observed that the addition of the water droplet immediately caused a significant drop in the resistance of the graphene strip. This is because the water pulls electrons out of the channel and increases the no. of holes in the graphene, thus causing a drop in the resistance. In other words, the graphene strip is getting p-doped. The resistance of the strip then increases with time as the droplet evaporates and stabilizes finally when the droplet has disappeared.

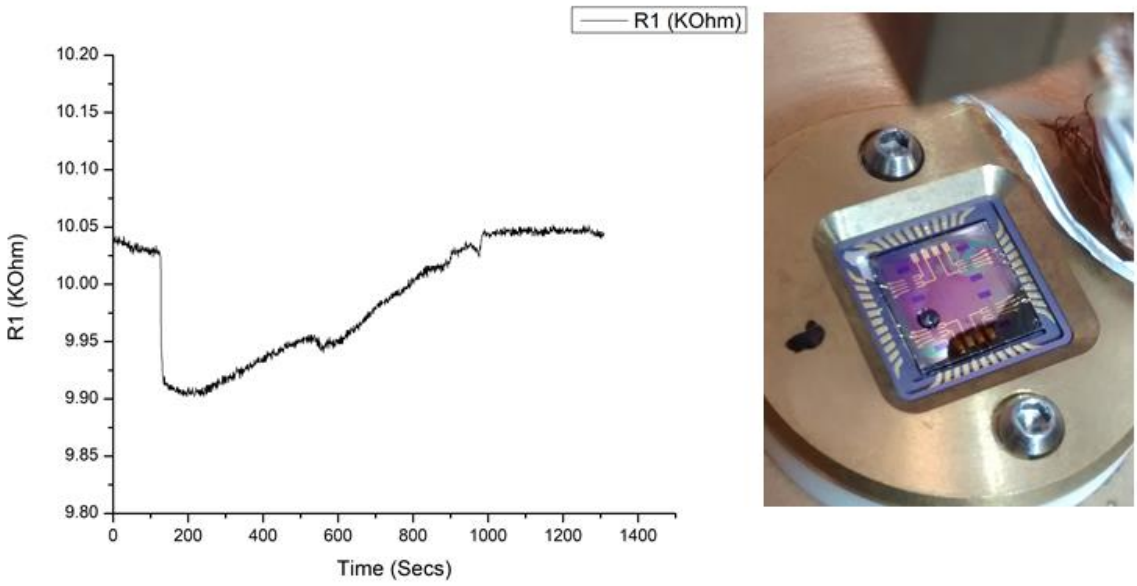

Figure 6.4: *Left:* Graph showing drop in resistance as a result of the a droplet of water being placed on the graphene strip. *Right:* A photograph taken of the sample after the drop was placed.

Further, it was also seen that when the meniscus of the drop was placed in the proximity of the graphene strip but not directly on it, as in the photo shown in Figure 6.5, the resistance of the graphene strip still dropped, indicating that the water was able to travel through the channel and affect the conductance of the channel.

In the graph, a droplet of water was dropped onto the substrate, causing a drop in resistance, it was then removed, causing an increase in resistance, then another drop was added in the same position, causing yet another drop and finally the drop was dried forcefully and rapidly using a N_2 gun thus causing a massive spike in the resistance, which stabilized shortly. The change in resistance in this case is smaller despite the drop being of the same volume. This can be explained by considering that only a small amount of water (not the bulk drop) travels along the channel might cause small amounts of water to travel along the channel (The underlying substrate is SiO_2) and wets the surface of the graphene, causing a smaller change in resistance. Additionally, it must be noted that the large spike in the plot is due to forceful suction of the droplet from the channel. This is anomalous to all other observations in this work.

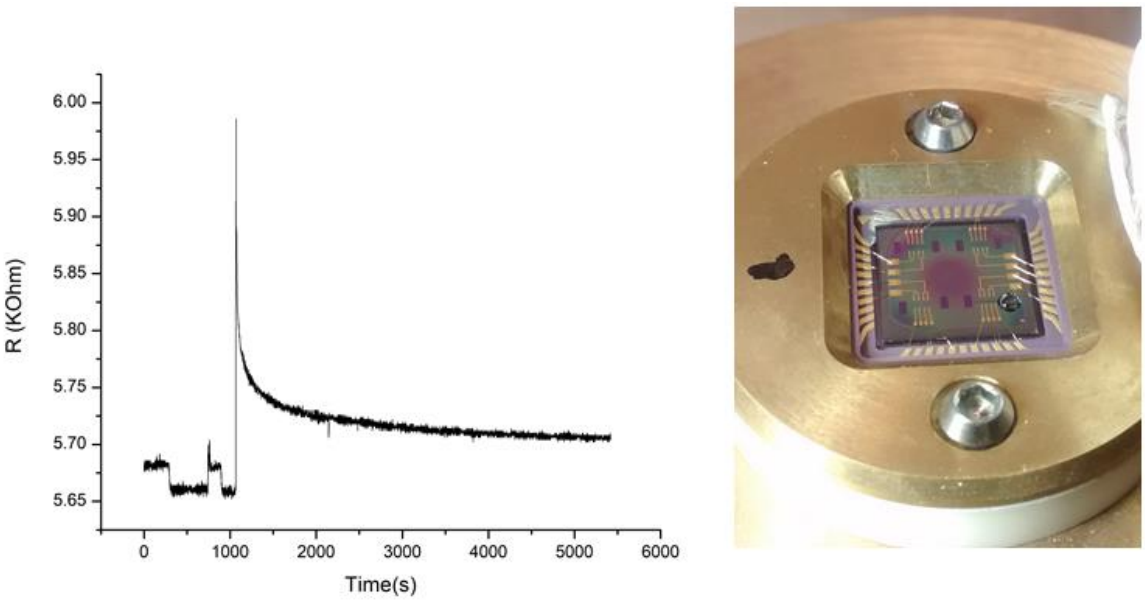

Figure 6.5: *Left:* Graph showing resistance changes as a result of the addition and removal of water twice, being placed in the proximity of the graphene strip. *Right:* A photograph taken of the sample after the drop was placed.

6.3.2 Measuring FET channel response to flow.

As a result of the design of the device, that incorporated micron size channels, it was important to establish whether these channels were able to fulfil their purpose. During the fabrication of the device, several different resist materials were explored for their ease of use, ease of handling and consistency in the output. SU-8, PDMS that have been reported in the literature were both tried but were found to be difficult to handle and not consistent in their reproducibility despite other groups reporting good results. [5][16] Finally, PMMA was chosen because it is routinely used and it was shown to produce reproducibly good results in terms of profile (as described in section 3.4). Here, we ascertain that the fluidic channels are indeed able to transport liquid. This is done by simultaneously measuring the R-T response of 2 or more graphene strips. All the devices on both samples S1 and S2 were electrically tested, their initial resistance on the application of 1V across the graphene strip was recorded and the microfluidic channels were checked optically to ensure that there were no blockages and the channels would able to allow the water to be transported through.

Figure 6. 6 shows the graphs that were recorded for sample S1 on the 5µm channel on the top left array, such that the drop is placed on the top reservoir above and not directly in contact with the two graphene strips TL1 and TL2 and after a length of time, it is removed gently with a N_2 gun. The two graphene strips are connected to two lock-in amplifiers as depicted in Figure 6.2. where R1 corresponds to the TL2 and R2 corresponds to TL1. The plots reveal that there is roughly the same % change in the resistance for both channels, indicating that a film of water is moving across the channel.

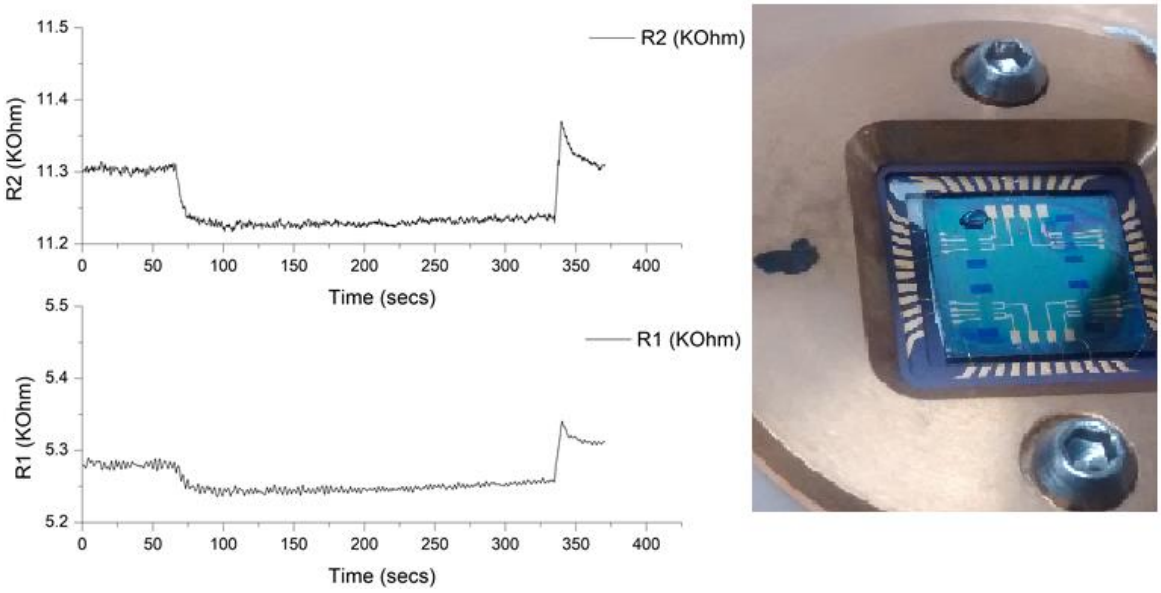

Figure 6.6: A Graph showing the R-T characteristics of two graphene strips TL1 (ΔR = 0.69%)and TL2 (ΔR = 0.71%) in sample S1, for the 5µm channel upon the placement of a drop in the top reservoir.

Figure 6.7 shows the measurement of 3 graphene strips concurrently. Here, the DI water droplet was placed on the bottom reservoir of the 50 µm channel. (Bottom Right) and the top three strips were connected to three separate lock-in amplifiers using the scheme in figure 6.2. In this graph, R1 represents the conductance changes occurring in BR1, the top most strip, furthest away from the droplet. R2 corresponds to BR2 and R3 corresponds to BR3.

In this case, a drop is place on the furthest edge of the reservoir from the channel, there is no discernible change in R in any of the three graphene strips. A second drop is then placed in the centre of the reservoir at ~ t=600 secs and this causes a small, discernible change in R in all 3 graphene strips. The drop is allowed to evaporate, and this causes a gradual increase in the resistance once again. Next, just after t=1500 secs, another drop is added such that it is touching BR4. This causes a noticeable drop in R once again which revives on evaporation. AT t=2200 secs, another drop is placed again in the same location and is dried with a N_2 gun, which causes an immediate spike in the resistance as the drop is blown off. Two more drops are placed in the channel this time over BR3 and blow-dried using the N_2 gun which each produces the corresponding drop and spike in resistance.

In every case, when the experiment was performed on both samples S1 and S2, it was found the graphene strip closest to the position of the drop showed the higher sensitivity and the graphene strip furthest from the dropped showed slightly smaller percentage change in the resistance. This seems to indicate that the graphene strip closest to the drop comes into greater contact with water perhaps in terms of surface area coverage, and perhaps this decreases further away from the drop along the channel.

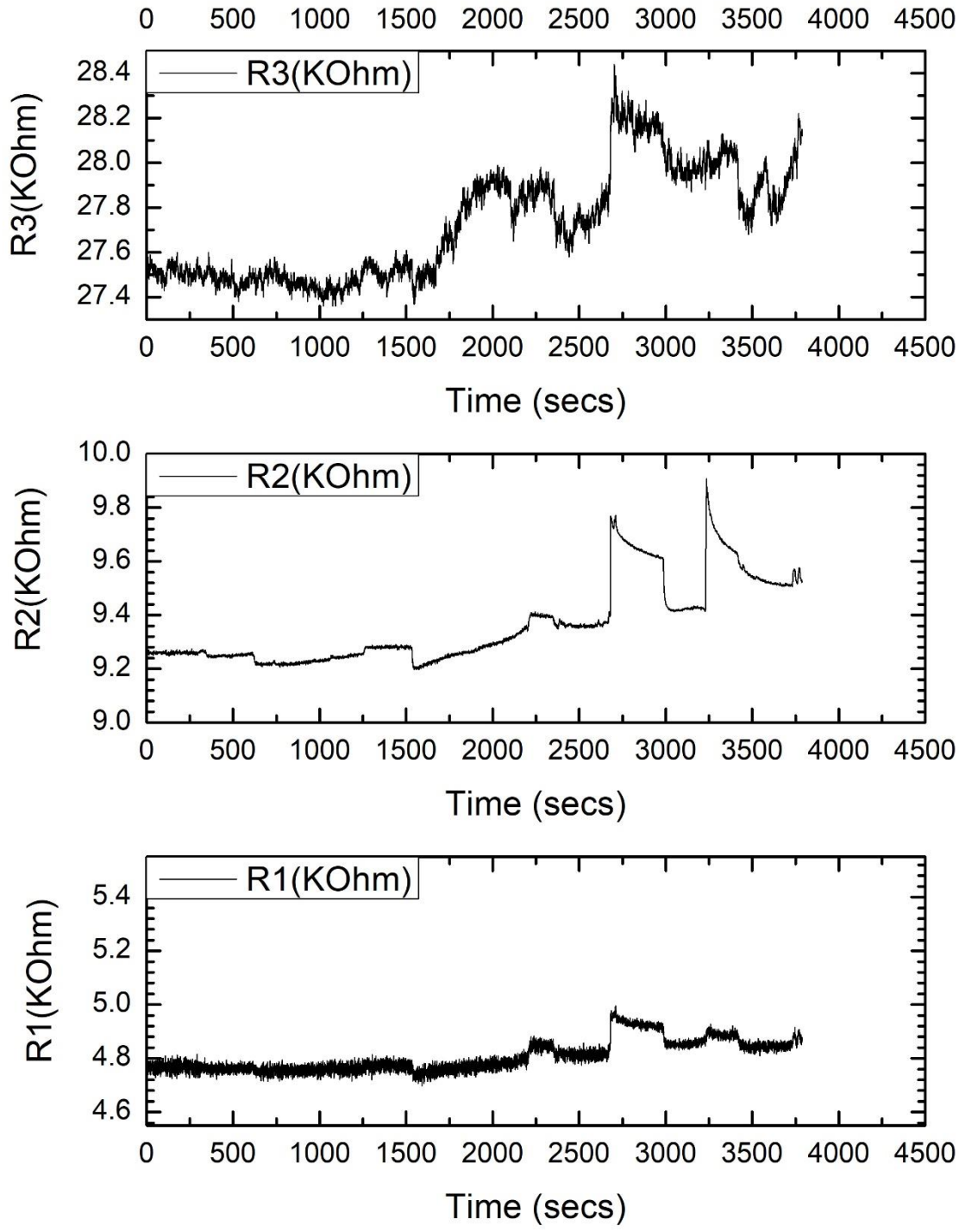

Figure 6.7: A Graph showing the R-T characteristics of three graphene strips BR1 and BR2 and BR3, for the 50μm channel in sample S1, upon the placement of a drop in the bottom reservoir.

6.3.3 DC Voltage effect on transport in FET channels.

The motivation behind introducing a DC voltage applied across one of the graphene strips, was to investigate if such a voltage would be a) significant enough to affect the transport characteristics of the other channels and b) whether the DI water droplet could be induced to move along the channel or repelled away from it by the application of an electric field. The measurement set up for this experiment is described in section 6.2.2.

Figure 6.8 shows the resistance of 2 graphene strips in the 20μm channel of BL1 and BL2, which are biased at 1V causing a current to flow through them. Before the application of the DC voltage, the resistance is steady. After an application of DC Voltage onto BL4 in sample 2, the sweeping of a DC voltage was found to exert a hysteretic behavior on the resistance of the graphene strips in the array. This seems to imply that the graphene strip acts as planar gate, exerting an electric field that can cause small changes in the surface charge density of the graphene strips BL1 and BL2.

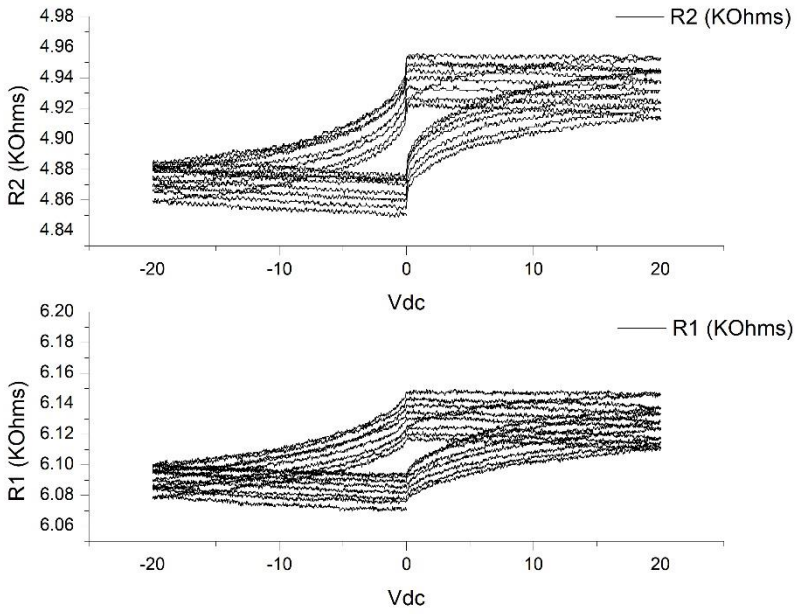

Figure 6.8: A graph showing the hysteretic response of the resistances for BL1 and BL2 on the application of Vdc on BL4.

The next measurement shows demonstrates the effect of putting 1 drop of DI water in the top reservoir of the BL channel. Here, BL4 is swept with a DC voltage between -10V and +10V and then between -20V and +20V and the resistance changes as function of this sweeping voltage are recorded. In both cases, the addition of the DC voltage has the effect of causing the resistance to increase when water is added. In the case of the first graph in Figure 6.9, the water droplet is added to the reservoir at V_{dc}=0V and in the case of Figure 6.10, the water droplet is added to the reservoir at V_{dc}= +20V. It is unclear as to what the origin of this reversal of behaviour is.

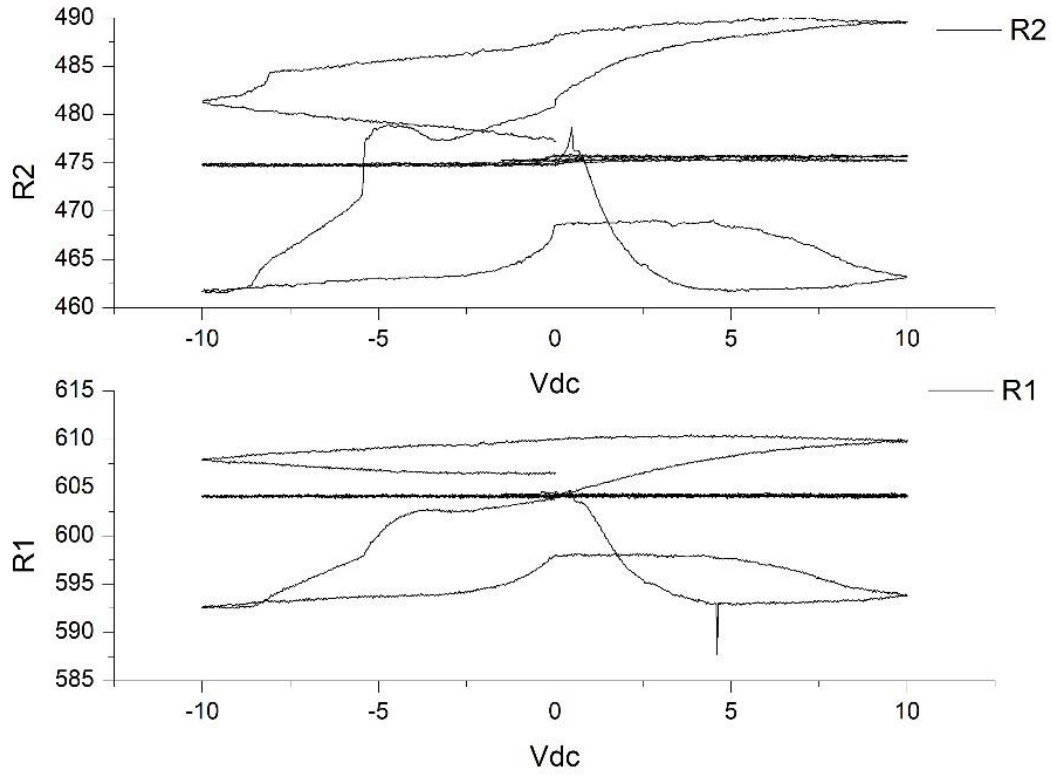

Figure 6.9: Resistance modulation on the addition of 1 drop of DI water at V_{dc}=0V as a result of V_{dc} being swept between -10V and +10V. Here R1 refers to BL2 an R2 refers to BL1.

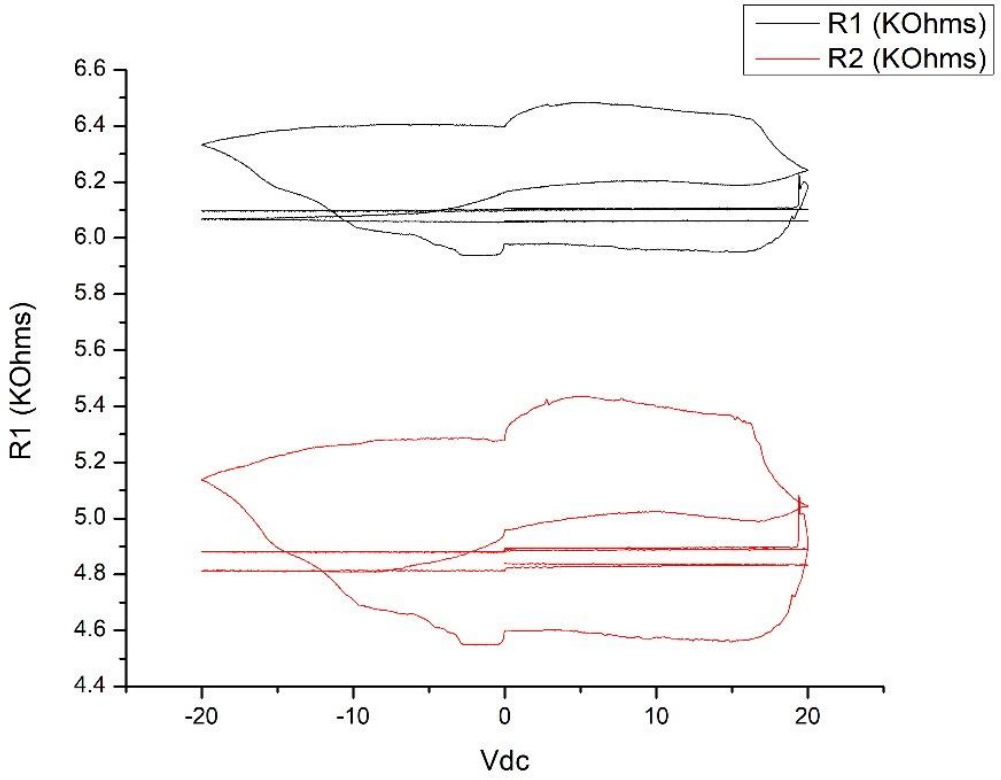

Figure 6.10: Resistance modulation on the addition of 1 drop of DI water at V_{dc}= 20V, as a result of V_{dc} being swept between -20V and +20V. Here R1 refers to BL2 an R2 refers to BL1.

However, for the sample S2, when the 5µm Top Left channel was being measured. It was observed that at V_{dc}=20V, which was held as a static potential on TL4, while TL1 and TL2 were measured, as evident in Figure 6.11, it was found that the resistance dropped in the characteristic manner, as a result of the addition of a drop of DI water on top of TL1 towards the top reservoir. Furthermore, it was observed that the resistance began to rise up quicker than expected for typical evaporation of a droplet of that size (10 mins) On taking photographs of the droplet, it was noticed that the water droplet appeared to be moving away from the channel and after about 300 secs the meniscus of the droplet appeared to no longer be on the TL1 graphene strip. This can be observed in the photos as shown in Figure 6.12

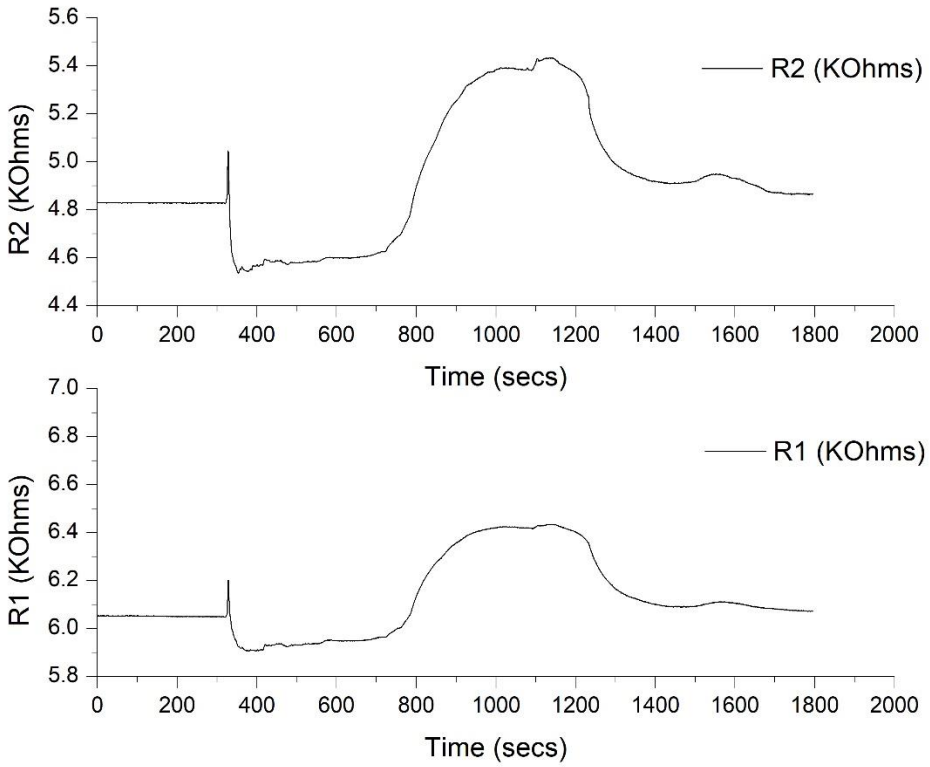

Figure 6.11: Resistance Vs. Time graph showing the addition of 1 drop of DI water at V_{dc}= 20V, for the top left array of the sample S2. Here R1 refers to BL2 an R2 refers to BL1.

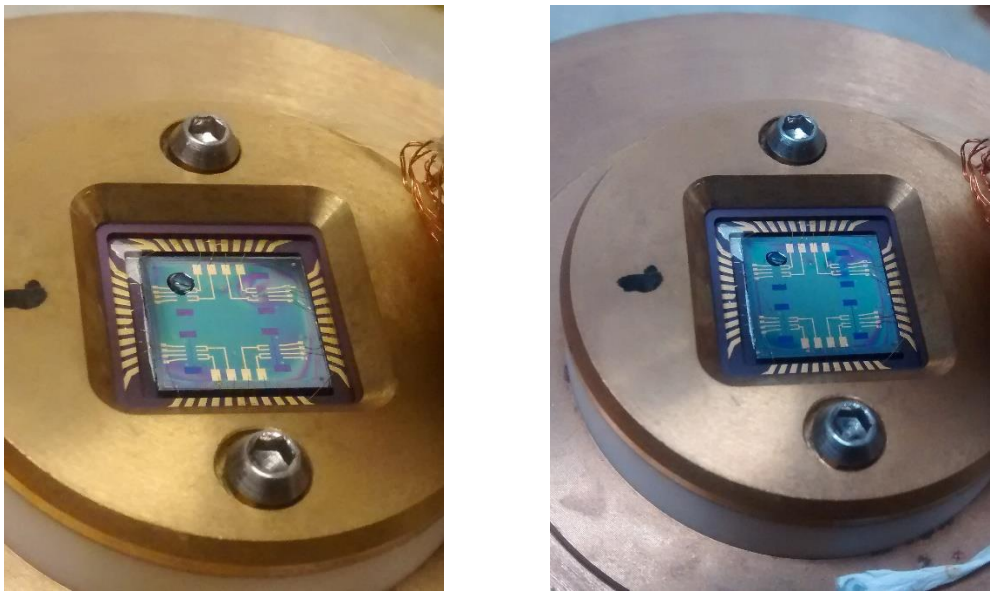

Figure 6.12: Photos showing the retreating meniscus of the water droplet away from the applied DC potential corresponding to the measurement in Figure 6.11

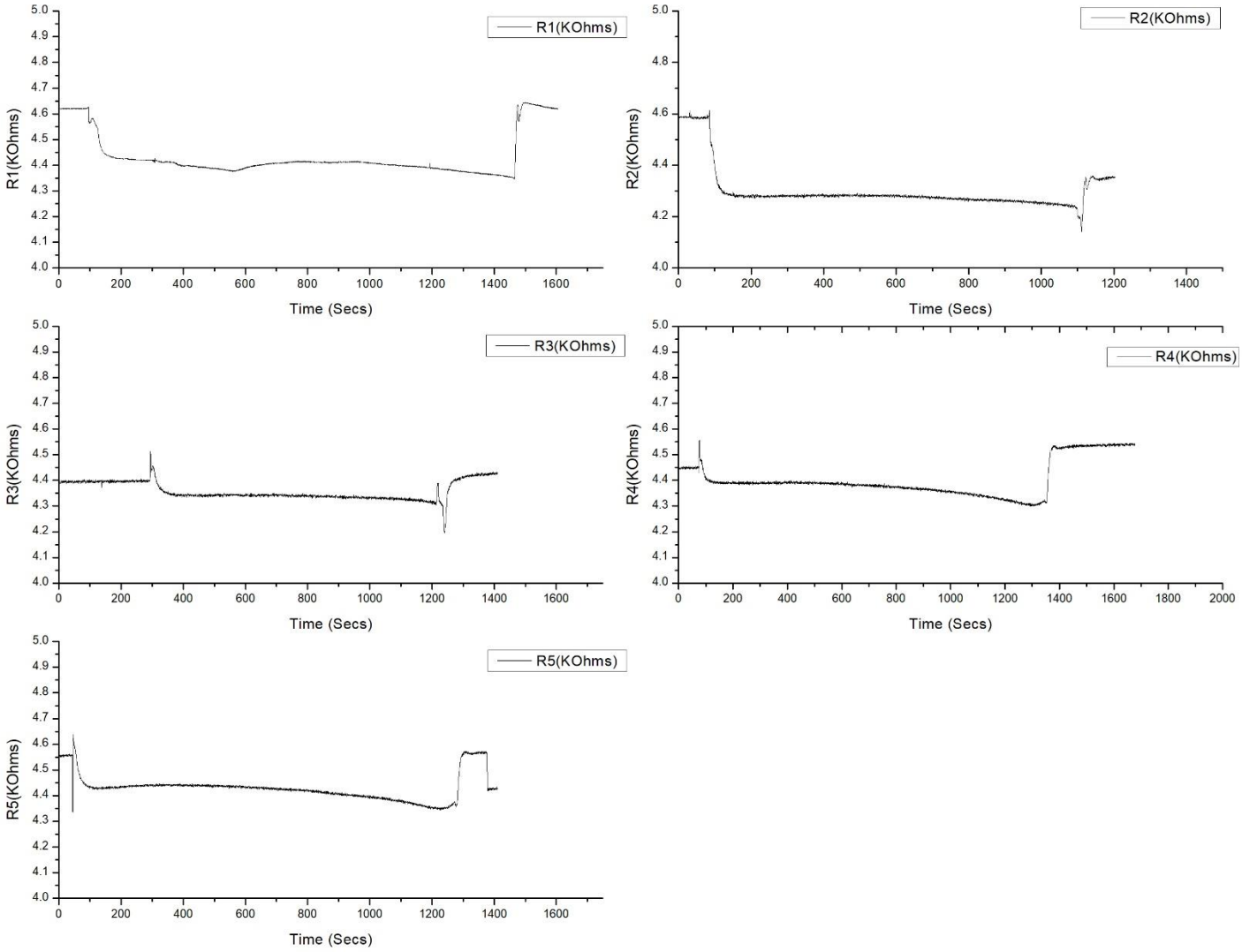

Figure 6.13: Resistance Vs. Time graph showing the addition of 1 drop of DI water and its removal by evaporation at 1) V_{dc}= 0V, 2) V_{dc}= 1V 3) V_{dc}= 5V 4) V_{dc}= 10V 5) V_{dc}= 20V for the top right of sample S2.

Further, the top right 20µm channel on sample two was measured for varying value of a statically applied positive voltage $V_{dc.}$ (0V, 1V, 5V, 10, 20V) as shown in figure 6.13. The drop was placed in exactly the same position (top reservoir) and the R-T characteristics for TR1 was recorded when V_{dc} was applied onto TR3. And it could be seen that some modulation of the resistance change

occurred. However, the mechanism behind this is yet unclear and needs further investigation.

6.4 Conclusion

In this chapter we have developed a hybrid graphene FET array that is embedded with microfluidic channels. The motivation for this is towards developing a POC device. The effect of water droplets on the device was measured and discussed. Further, it was shown that the microfluidic channels at all three widths are able to allow transport of water, such that individual graphene strips can sense them. This scheme is extremely useful and can be adapted to a host of other sensing applications, which would benefit from dynamic and precise control on the detection of the analyte. The sensitivity of this method is that it can also be tuned by applying a biasing voltage on the back gate. Additionally, a planar gate-like potential was applied, which shows some modulation of the graphene channels. There is scope for a lot more investigation with this work. For instance, in the previous chapter, a proof of concept immunosensor device for the electronic sensing of Procalcitonin, a biomarker for Sepsis was demonstrated. And there is a need for the sensing element, namely the graphene surface to be regenerated for repeated use. This is not possible in a simple device architecture as used in Chapter 5, unless the bonding is removing (which could easily destroy the device). This can be achieved however, if a fluidic channel is integrated with the device as the reagents that un-bind the antibody molecules can be flushed through the channel for a period of time, and will only interact with the resist, the graphene and the substrate.

6.5 Bibliography

1. Ana Carolina Mazarin de Moraes and Lauro Tatsuo Kubota Chemosensors 2016, 4, 20
2. Jinglei Ping,†,§ Ramya Vishnubhotla, Amey Vrudhula, and A. T. Charlie Johnson, ACS Nano 2016, 10, 8700−8704
3. Shaurya Prakash, Marie Pinti and Bharat Bhushan Phil. Trans. R. Soc. A 370, 2269–2303
4. S. Goniszewski1,2, M. Adabi1, O. Shaforost1,2, S. M. Hanham1, L. Hao1,2 & N. Klein1 Scientific Reports | 6:22858 |
5. N C S Vieira et al 2016 J. Phys.: Condens. Matter 28 085302
6. Macie juszczek,, Dariusz _wisulski, Robert Hanus, Marcin Zych, and Leszek Petryka EPJ Web of Conferences 143, 02068 (2017)
7. Haomin Wang, Yihong Wu, Chunxiao Cong, Jingzhi Shang, and Ting Yu *ACS Nano*, 2010, 4 (12), pp 7221–7228
8. Sowmya Viswanathan1, Tharangattu N. Narayanan, Kiana Aran, Kathryn D. Fink, Jacobo Paredes, Pulickel M. Ajayan, Slawomir Filipek, Przemyslaw Miszta, H. Cumhur Tekin, Fatih Inci6, Utkan Demirci, Pingzuo Li, Kirill I. Bolotin, Dorian Liepmann and V. Renugopalakrishanan Materials Today _ Volume 18, Number 9 _ November 2015
9. Bedri Gurkan Sonmez , Ozan Ertop & Senol Mutlu Scientific Reports | 7: 12190 | DOI:10.1038/s41598-017-12439-8 1
10. Ning Gaoa,1, Teng Gaoa,1, Xiao Yanga, Xiaochuan Daia, Wei Zhoua, Anqi Zhanga, and Charles M. Liebera,b,2 PNAS | December 20, 2016 | vol. 113 | no. 51 | 14633–14638
11. Priscilla Kailian Ang,Ang Li, Manu Jaiswal,Yu Wang, Han Wei Hou, John T. L. Thong,Chwee Teck Lim and Kian Ping Loh Nano Lett. 2011, 11, 5240–5246
12. C Melios et al 2018 *D Mater.* **5** 022001

13. Bollmann T R J, Antipina L Y, Temmen M, Reichling M and Sorokin P B 2015 Hole-doping of mechanically exfoliated graphene by confined hydration layers *Nano Res.* **8** 3020–6
14. Shao, Y. Y., Wang, J., Wu, H., Liu, J., Aksay, I. A., Lin, Y. H. Electroanalysis 2010, 22, 1027–1036
15. Alwarappan, S., Erdem, A., Liu, C., Li, C. Z. J. Phys. Chem. C 2009, 113, 8853–8857.
16. Wan Li,Cen Tan,Michael A. Lowe,Hector D. Abruna, D. C. Ralph. ACS Nano 2011, Vol.5, No.3, 2264-2270
17. Pumera, M et al., 2009. Chem. Rec. 9, 211–223.
18. Tang, L.,Wang, Y., Li, Y., Feng, H., Lu, J., Li, J., 2009. Adv. Funct.Mater. 2782–2789.
19. T. Kuila et al , Biosensors and Bioelectronics 26 (2011) 4637– 4648

Conclusions and Future Work

This thesis demonstrates the work done towards investigating graphene-based devices for applications in electro-chromism and sensing. Three separate devices were fabricated for three different sets of measurements. The electrochemical characterisation of graphene was undertaken and the electron transfer behaviour studies of graphene using cyclic voltammetry (CV) of redox couples, $[Fe(CN)_6]^{-3/-4}$and $[Ru(NH_3)_6]^{+3/+2}$ was studied and it was shown that the graphene exhibited well-defined redox peaks. This indicates that the unique electronic structure of graphene, especially the high density of the electronic states over a wide energy range, endows graphene with fast electron transfer rates. This, along with its surface physico-chemistry are beneficial and can make graphene a good platform for electrochemical sensing of biomolecules. Graphene was then used as a working electrode to create an electrochromic device where the optical transparency of the graphene was modulated and the electrochemical characteristics of the graphene device were examined. It was seen that graphene could sustain reversible electrodeposition of Pb onto its surface for upto 40 cycles. After this, some degradation of the surface was observed. The surface was renewed by applying a positive potential step to oxidise the deposited Pb and dissolve it into solution. However, this was not able to fully refresh the surface and restore it to its original state. In this regard, more work needs to be done to improve the longevity of the electrochromic device and explore the usage of other electrolytes towards a device with a longer life-cycle.

The measurements as described in chapter 5 offer a proof of concept detection for the presence of a biomarker for Sepsis. It is shown that the graphene-based FET device was able to sense the presence of the Anti-PCT antibody and differentiate from its buffer solution. Furthermore, the device was able to support a second binding event, where PCT attached to the Antibody and caused a measurable increase in the resistance. The resistance increases were correlated with the concentration of the PCT solutions used and were shown to be responsive over the entire medically required range from 50ng/L to 1000 ng/L . The sensor offers a new electrical measurement route for diagnosis of Sepsis in real time measurements.

Further work is needed to achieve greater control over the electrical measurement characteristics. Exploring alternate devices geometries such as arrays of Graphene FET channels would offer the advantage of multiple binding sites, because the cumulative area of the graphene would be large, as well as offering greater control over the device characteristics. Most importantly, the ability to measure Dirac point shifts at room temperature would lead to the possibility of calibrating the sensor for the concentration of Analyte solution. This could be achieved firstly by improving the fabrication process so as to reduce impurities and dopants on the graphene surface.

In chapter 6, we have developed a hybrid graphene FET array that is embedded with microfluidic channels. The motivation for this is towards developing a POC device. The effect of water droplets on the device was measured and discussed. Further, it was shown that the microfluidic channels at all three widths are able to allow flow of water, such that individual graphene strips can sense them. This scheme is extremely useful and can be adapted to a host of other sensing applications, which would benefit from dynamic and precise control on the detection of the analyte. This method is of further interest because it can also be tuned by applying a biasing voltage on the back gate. Additionally, an in-plane side gate potential was applied, which shows some modulation of the graphene channels. There is scope for a lot more investigation with this work. For instance, in the previous chapter, a proof of concept immunosensor device for the electronic sensing of Procalcitonin, a biomarker for Sepsis was demonstrated. And there is a need for the sensing element, namely the graphene surface to be regenerated for repeated use. This is not possible in a simple device architecture as used in Chapter 5, unless the bonding is removing (which could easily destroy the device). This can be achieved however, if a fluidic channel is integrated with the device as the reagents that un-bind the antibody molecules can be flushed through the channel for a period of time, and will only interact with the resist, the graphene and the substrate.